Anisotropy in Residual Stresses and Subsurface Damage in Machined Ceramics

By

Aditya Nagaraj

A dissertation submitted in partial fulfillment of

the requirements for the degree of

Doctor of Philosophy

(Mechanical Engineering)

at the

UNIVERSITY of WISCONSIN-MADISON

2024

Date of final oral examination: December 13, 2024

The dissertation is approved by the following members of the Final Oral Committee:

Sangkee Min, Associate Professor, Mechanical Engineering, UW-Madison

Frank E. Pfefferkorn, Professor, Mechanical Engineering, UW-Madison

Lianyi Chen, Associate Professor, Mechanical Engineering, UW-Madison

Ramathasan Thevamaran, Associate Professor, Mechanical Engineering, UW-Madison

Paul Voyles, Professor, Materials Science and Engineering, UW-Madison

Woo Kyun Kim, Associate Professor, Mechanical and Materials Engineering, University of Cincinnati

© Copyright by Aditya Nagaraj 2024

All Rights Reserved

This work is dedicated to my parents and grandmother.

Abstract

As humankind continues to push the boundaries of science and technology to explore and develop a deeper understanding of our universe, materials that can perform reliably, under harsh conditions are a necessity. Single crystal sapphire ($\alpha - Al_2O_3$) and 8-mol % yttria stabilized zirconia (8YSZ) are two such materials that are frequently used in a variety of applications ranging from protective optical windows and electronic substrates to biomedical implants and solid oxide fuel cells. Although properties such as high hardness, chemical resistance and superior mechanical strength make these materials favorable in the applications mentioned, fabricating these ceramics into intricate shapes is challenging as these properties along with pronounced brittleness hinder material removal. Commonly, ceramics have been processed through loose abrasive processes such as grinding and polishing which take advantage of the ductile-brittle transition observed at small length scales (on the order a few microns or smaller). However, a major limitation of these abrasive processes is that complex shapes cannot be fabricated due to limitations in tool geometries that can be used. One promising technique that has been developed to address this issue is Ultra-precision Machining (UPM), which provides the flexibility in terms of tooling as well as precise control of multiple machine axes which can be used to cut complex geometries in ceramics in a ductile manner. In spite of overcoming some of the challenges mentioned, two new challenges, namely material anisotropy and residual stresses need to be addressed to improve the material removal rate and process single crystal ceramics more efficiently.

Through preliminary research conducted at the Manufacturing Innovation Network (MIN) lab, the effect of crystal anisotropy on material deformation during machining of sapphire was quantified in terms of the critical depth of cut (depth of cut at which ductile-brittle transition occurs) and this result was extended to the case of 2-step machining (machining over an area that has been previously machined). In these studies, a decrease in the Critical Depth of Cut (CDC) was observed during the second machining operation which hinted at the presence of residual stresses or subsurface damage that promoted crack initiation at a lower stress compared to machining of a pristine ceramic surface and forms the motivation for this work. Furthermore, a literature survey on this topic revealed that detailed studies correlating the residual stress and

subsurface damage to activation of different deformation mechanisms in single crystals had not been conducted.

Based on the preliminary experimental results, it was hypothesized that the residual stresses and subsurface damage would be anisotropic in nature depending on the cutting direction and depth of cut, due to activation of distinct deformation mechanisms in different cutting directions. To test this hypothesis, machining was performed on 4 different crystallographic planes of sapphire (A-, C-, M-, and R-) and two planes on 8YSZ ((001) and (011)). Subsequently, in the first phase of the study, residual stress magnitude was quantified for 7 cutting directions on each plane of sapphire and 8YSZ. Particularly, these measurements were made at different depths of cut, focusing on the ductile, Ductile to Brittle Transition (DBT), and brittle regions of the cut.

In the case of sapphire, the residual stresses were tensile in nature for most of the cases and the ductile regions had a higher residual stress magnitude than the brittle region. The magnitude of residual stress varied from -65 MPa (compressive) in a couple of cases to 148 MPa (tensile). There was a clear anisotropy in the residual stress magnitude in terms of the cutting direction and depth of cut. In crystallographic planes like the C-plane, the residual stress magnitude was almost negligible but in some other planes like the M- and R-planes, much larger magnitudes of residual stress was observed.

To further understand the reason for this anisotropy, the most likely modes of plastic deformation on the C- and R-planes were calculated and compared. It was found that, based on the alignment of the dominant slip/twinning system with respect to the machined surface, more plastically deformed material was likely to remain in the workpiece post machining, such as certain directions on the R-plane that exhibited higher magnitudes of residual stress. On the contrary, most of the plastically deformed material on the C-plane and few R-plane directions would be removed by chip formation, thus confirming the hypothesis initially presented. These efforts were then extended to understand the residual stress tensor post machining. Next, residual stress measurements were carried out on the 2 planes of 8YSZ through analysis of nanoindentation data. For the analysis, two different approaches were followed - fracture toughness based calculation and energy partition based calculation. The residual stresses were generally tensile in nature. However, in the brittle regions of the cut, very large fluctuations in the residual

stress measurements were observed. The residual stresses in the ductile region varied between -35 and 240 MPa.

The second phase of this study involved understanding subsurface damage through Raman spectroscopy, Transmission Electron Microscopy (TEM), and Molecular Dynamics (MD) simulations. This portion of the study was limited to sapphire. To begin with the subsurface damage across different cutting directions was evaluated by investigating the relative peak broadening of the 417 cm^{-1} peak. These evaluations were done both in the depth wise direction (selected directions on the R-plane) and along the machined surface (A-, C-, M-, R-planes). It was observed that the crack morphology played an important role in influencing the subsurface damage and generally the directions with lateral and sculptured cracks which extended deeper into the subsurface by way of the alignment of the cleavage plane with respect to the machined surface led to higher amounts of peak broadening and subsurface damage whereas cutting directions with shallower spalling or fan shaped cracks that were restricted closer to the surface showed smaller amounts of peak broadening.

In the next section, MD simulations results from selected cutting directions were analyzed and the trends in the damage depth were compared with the results from the Raman evaluation of subsurface damage. It was observed that most of the cutting directions followed the same trends as the Raman results except for the 2 cases on the C-plane of sapphire. The likely cause for this discrepancy could be due to the differences in the time and length scales of the MD simulations which were performed at much higher strain rates than the experiments.

In the last section of this phase of the study, TEM evaluation was carried out for different cases. In the first set of cases, the subsurface damage was compared between the C- and R-plane of sapphire. It was observed that in the case of the C-plane, the damage was limited very close to the surface and the basal twinning acted like a blocking mechanism to prevent any deformation from extending deeper into the subsurface. On the contrary, larger amount of subsurface damage in the form of cracks, plastic deformation, amorphization, and stacking faults was observed on the R-plane of sapphire. These results supported the Raman spectroscopy results and the hypothesis presented at the beginning of this study. In the second set of experiments, two samples were made on the C-plane of sapphire parallel to the cutting direction along 180° and 270°. In both these samples, deformation parallel to the basal plane and just below the machined

surface were observed. In the case of the 180° cutting direction, additional subsurface cracks and large amounts of plastic deformation in the subsurface were observed. However, in the 270°, the deformation was limited to few bands of basal twinning and no other forms of deformation were observed. These trends were similar to the subsurface damage predicted from the Raman peak broadening.

The third part of this research involved investigating the effect of different process parameters such as machining pitch and depth of first cut on surface cracking and residual stress formation during 2-step machining operations. Based on the results in the previous section, it was evident that the crystal anisotropy played a major role in influencing the residual stress state, as well as the surface and subsurface damage mechanisms. The main objective behind this section was to investigate whether the deformation anisotropy could be exploited to develop machining strategies that improve the material removal rate while minimizing surface and subsurface damage. The first two experiments involved studying the effect of machining pitch and depth of first cut on the CDC of the subsequent machining operation on the A-plane of sapphire. These experiments provided insight into how to account for different crack morphologies, residual stress state, and material deformation mechanisms while choosing a machining strategy. The next stage of this research involved demonstrating a machining strategy on the R-plane of sapphire to improve the machining throughput to obtain a ductile machined surface while minimizing the residual stresses. The process parameters for this strategy were selected by choosing cutting conditions that leave behind shallow cracks and low residual stress during rough machining and performing finish machining under conditions with higher CDC to get rid of the surface defects.

Through the knowledge gained in this study, our understanding of material deformation during UPM of ceramics and residual stress/subsurface damage formation is improved, guiding us towards increasing the efficiency of the machining process of hard and brittle materials by exploiting the anisotropic deformation characteristics observed.

Acknowledgements

First and foremost, I would like to express my heartfelt gratitude to Prof. Sangkee Min, who has been an inspiration, mentor, and friend over the past 7 years. Thank you for believing in me and providing me an opportunity to work at the Manufacturing Innovation Network (MIN) Lab. None of this work would have been possible without your constant support and encouragement.

My heartfelt thanks to Prof. Frank Pfefferkorn for serving on my thesis defense committee, providing constant guidance, and for facilitating my acceptance to the Manufacturing Systems Engineering graduate program at UW Madison which was the start to this wonderful journey. I would like to thank my thesis defense committee members Prof. Lianyi Chen, Prof. Ramathasan Thevamaran, and Prof. Paul Voyles for their valuable feedback and guidance to improve my research work and dissertation. I'm truly indebted to them for the knowledge shared through their courses which helped me make significant progress in my research.

My sincere thanks to Prof. Woo Kyun Kim and his group at the University of Cincinnati for the fruitful collaboration and guidance over the past five years. The molecular dynamics simulations helped me better understand the different deformation mechanisms during ultra-precision machining and formed a key part in formulating the main hypothesis for this work. I would also like to thank Prof. Kim for serving on my defense committee and providing valuable feedback to help improve my dissertation.

Sincere thanks to my research collaborators Dr. Suk Bum Kwon, Dae Nyoung Kim, Rui Liang, Dalei Xi, and Yiyang Du for fostering a friendly and creative atmosphere in the lab and throughout our collaborative project with the University of Cincinnati. I would like to appreciate Dr. Kwon for helping with the SEM imaging of crack morphology on sapphire and for the numerous discussions and valuable insights provided at various stages during my master's and doctoral studies. I would also like to thank Vignesh Selvaraj and Manikanta Grandhi for collaborating on projects outside the scope of this dissertation. Working on new and diverse topics helped me gain new skills, expand my horizons, and become a better researcher.

I would like to thank Dave Tuschel, Dr. Justin Morrow, and Dr. Francis Deck for providing valuable guidance while beginning the residual stress measurements using Raman spectroscopy.

Their advice on choosing the Raman measurement parameters helped set the stage for a major portion of the data collection for this work. I would like to extend my gratitude to the staff at NIAC, UW-Madison - Dr. Julie Morasch, Dr. Donald Savage, Dr. Alex Kvit, Dr. Nick Bulloss, and Richard Noll for always being willing to help and patiently answering all my questions related to the operation of various material characterization and sample preparation equipment.

Special thanks to my friends and colleagues at the MIN Lab over the years, especially Prof. Sangjin Maeng, Prof. Hae-Sung Yoon, Zach Lowery, and Shodai Yamada for their enduring friendship and teaching me about a lot of different things ranging from CNC machine operation to conducting research, that have helped me formulate new ideas over time.

This work could not have been realized without the kind support of FANUC Corporation, Japan in terms of the monetary assistance and donation of the ultra-precision machine tool, ROBONANO α-0iB to theMIN lab at the University of Wisconsin-Madison. I would also like to thank A.L.M.T. Corporation, Japan for providing the diamond tools used for the experiments at a discounted price. This work was supported in part by the National Science Foundation under the award number CMMI-2008563. Additionally, I would like to gratefully acknowledge use of facilities and instrumentation supported by NSF through the University of Wisconsin Materials Research Science and Engineering Center (DMR-1720415).

Sincere thanks to the Department of Mechanical Engineering, UW-Madison for supporting the early part of my doctoral studies through a teaching assistantship without which I would not have been able to continue my studies.

Heartfelt thanks to all my friends and well wishers for their support and encouragement throughout the years!

I would like to thank my mother Chitra and father Nagaraj for encouraging me to explore the world and pursue the path of my liking. No amount of words will ever suffice for the unconditional love and support they have given me over the last thirty one years and being the pillars for me to lean on at all times. I would like to thank my grandmother Vijayam and late grandfather Ramakrishnan for taking care of me while my parents were away at work. I owe everything to my family.

Contents

List of Figures

List of Tables

Acronyms

8YSZ 8-mol % yttria stabilized zirconia.

AFM Atomic Force Microscopy.

CAD Computer Aided Design.

CAM Computer Aided Manufacturing.

CDC Critical Depth of Cut.

CIRP College International pour la Recherche en Productique - International Academy for Production Engineering.

CMP Chemo-mechanical Polishing.

CNC Computer Numerical Control.

CRSS Critical Resolved Shear Stress.

CSIF Critical Stress Intensity Factor.

DBT Ductile to Brittle Transition.

EDS Energy-Dispersive X-ray Spectroscopy.

FFT Fast Fourier Transform.

FFT Inverse Fast Fourier Transform.

FIB Focused Ion Beam.

FWHM Full Width at Half Maximum.

HRTEM High Resolution Transmission Electron Microscopy.

IC Integrated Circuit.

LAMMPS Large-scale Atomistic/Molecular Massively Parallel Simulator.

LED Light Emitting Diode.

MD Molecular Dynamics.

MIN Manufacturing Innovation Network.

NASA National Aeronautics and Space Administration.

NSF National Science Foundation.

O-CDC Critical Depth of Cut of Primary Cut.

PBC Periodic Boundary Condition.

PCD Polycrystalline Diamond.

S-CDC Critical Depth of Cut of Subsequent Cut.

SCD Single Crystalline Diamond.

SEM Scanning Electron Microscopy.

SOFC Solid Oxide Fuel Cell.

TEM Transmission Electron Microscopy.

UPM Ultra-precision Machining.

List of Symbols

ν	Poisson's ratio
a	Length of initial flaw in the material
A_{pml}	Projected contact area
c	Cleavage factor
D	Degree of damage
E	Young's modulus
E_r	Reduced modulus
F_c	Cutting force
F_t	Thrust force
$F_j^{'}$	Cleavage fracture parameter
H	Hardness
h_c	Indentation contact depth
h_{max}	Maximum indentation depth
K_I	Stress intensity factor
K_{IC}	Critical stress intensity factor
M	Resistance to machining-induced cracking
m	Schmid factor
$P_i^{'}$	Plastic deformation parameter
P_{max}	Maximum indentation load
U_r	Plastic energy during indentation
U_t	Total energy during indentation
$\Delta\nu$	Raman peak shift
λ	Angle between slip direction and direction of applied stress
ϕ	Angle between slip plane normal and direction of applied stress
Φ_{xyz}	Rotation matrix
Π_{ij}	Piezospectroscopic coefficients
ψ	Angle between cleavage plane normal and direction of applied stress

σ	Applied stress
σ_{ij}	Stress tensor
σ_N	Applied tensile stress
τ^{crit}	Critical resolved shear stress
τ_s	Resolved shear stress
θ_{force}	Angle between the resultant force and cutting force

Chapter 1

Introduction

The quest for scientific advancement and exploration in a wide range of fields calls for materials that can perform reliably under harsh conditions. Drawing from a wide range of disciplines, some examples include optical switches for high energy lasers used to realize inertial confinement fusion [1], scientific instruments on spacecraft and space based telescopes [2,3], and biomedical implants such as artificial knee or hip joints [4]. A common class of materials used for these applications are single crystal ceramics, due to favorable properties such as superior optical and mechanical properties, chemical inertness, and wear resistance [5–7]. In spite of the favorable properties, manufacturing ceramics is challenging due to the high hardness which rapidly wears out tools. Further, due to the brittle nature, crack initiation can occur easily, hindering the functionality of many components, especially optics. Additionally, the anisotropic crystal structure and properties make it difficult to design tool paths and machining strategies [8,9].

Conventionally, ceramics have been manufactured using loose abrasive processes such as polishing and grinding that remove material at small cutting depths, below the ductile-brittle transition (also known as the Critical Depth of Cut (CDC)) [10–12]. However, these manufacturing processes have some drawbacks: i) available tool profiles and geometries limit the part geometries and forms that can be produced, ii) producing miniature parts and features on the order of a few hundred microns can be a challenge as it is difficult to control the movement of abrasive particles at those scales, and iii) many applications like optics and electronics require nanometer level surface roughness [13] which can be achieved only by multiple operations on different machines which would make the process capital intensive.

With advancements in manufacturing technology, control systems, sensors, and CAD/CAM software, many companies have produced ultra-precision Computer Numerical Control (CNC) machines capable of multi-axis movements with a command resolution of a single angstrom that

have addressed the short comings previously mentioned [14, 15]. With these machines, it is possible to cut hard and brittle ceramics at depths lower than the CDC while maintaining sub-micron form accuracy and surface roughness for complex part geometries, all on a single machine. While machining at these small scales, the tool-workpiece interactions are very different from that observed in conventional machining. For a start, as the cutting depth is reduced to the same order of magnitude as the grain size of most engineering materials, the grain orientation and crystal anisotropy start to influence the material removal behavior [16]. Additionally, as the tool edge radius is of the same order of magnitude as the cutting depth, the material deformation and chip formation are significantly affected by this tool-geometry parameter [17,18]. Hence, conventional machining principles cannot be applied directly to the case of Ultra-precision Machining (UPM) [16, 19]. Due to these complexities, the mechanism of material removal during UPM is not fully understood and further study is necessary.

1.1 Motivation

To better understand material deformation during UPM of ceramics and develop useful machining strategies, multiple experiments were carried out at the MIN Lab. In terms of the preliminary work, single, isolated cuts were made to understand the effect of crystallography on material deformation. However, in practical scenarios, multiple machining passes are needed to go from the raw material to the required finished geometry in majority of cases. To study material deformation from this perspective, few studies were conducted. In particular, three experiments relevant to overlapping machining are pertinent to the current research and are described in the following subsections. A detailed account of the work can be found in my Master's thesis [20].

1.1.1 Overlapping Cutting on A-plane of Sapphire

The objective of the first experiment was to examine the material response during repeated machining at depths of cut up to the CDC - the depth at which ductile-brittle transition occurs. The experiment was performed on the A-plane of sapphire in a cutting direction with a CDC of 220 nm. The tool path had a slope of 1/500 in the entry and exit portions with a region of constant depth of cut in between. The depth of cut increments for the 3 trials performed were

chosen to be 120 nm, 180 nm, and 220 nm and up to 4 overlapping cuts were performed for each depth increment. A schematic of the experiment is shown in Figure 1.1.

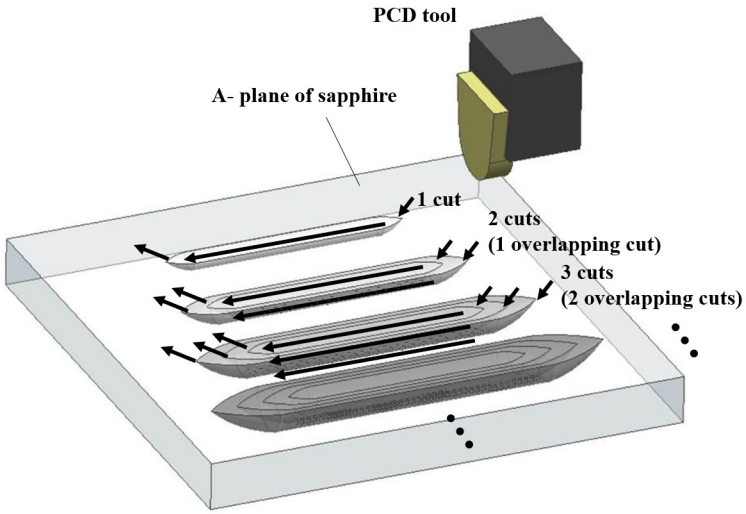

Figure 1.1: Schematic of overlapping cutting on A-plane of sapphire [21].

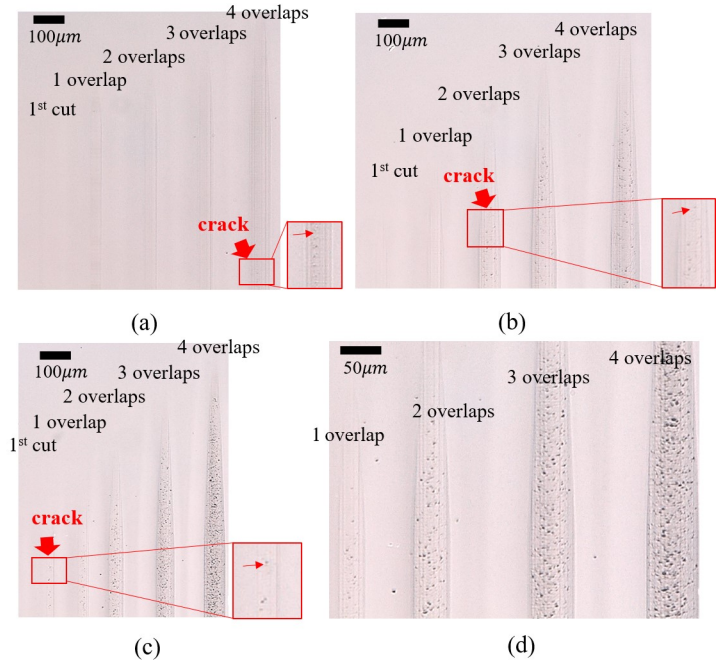

Figure 1.2: Optical images of successive overlapping cuts with depth of cut increments of (a) 120 nm, (b) 180 nm, and (c, d) 220 nm on A-plane of sapphire [21].

Optical images of the resulting machined surfaces are shown in Figure 1.2. It was observed that when the depth increment was 120 nm, ductile machined surface was observed up to the

third cut. However, on the fourth cut, small cracks were observed on the machined surface even though the depth of cut was smaller than the CDC. Similarly, when the depth increment was 180 nm, cracks were observed from the second overlap. In case of the 220 nm depth increment, cracks were visible from the first cut itself as this depth corresponds to the CDC for the given cutting direction. Further, as the number of overlaps were increased for this depth increment, the size and concentration of cracks observed also increased.

1.1.2 2-Step Cutting on C-plane of Sapphire

The experiments on the C-plane of sapphire mainly aimed to study the effect of varying cutting direction on the material response. Since the direction of the subsequent cuts did not align with the first cut, a cracked surface area was first created over which the subsequent plunge cuts were performed. The plunge cuts had an entry and exit slope of 1/500. Two sets of experiments were performed; (i) varying direction of subsequent cutting (primary cutting in $[11\bar{2}0]$ direction – denoted as 0°) and (ii) varying the direction of primary cutting (subsequent cutting in $[11\bar{2}0]$ direction - denoted as 0°). In the first set of experiments, subsequent plunge cuts were performed in the 0° – $[11\bar{2}0]$, 30° – $[10\bar{1}0]$, 60° – $[2\bar{1}\bar{1}0]$ and 90° – $[1\bar{1}00]$ directions. In the second set of experiments, the primary cuts were performed in the 0° – $[11\bar{2}0]$, 30° – $[10\bar{1}0]$, 60° – $[2\bar{1}\bar{1}0]$, and 90° – $[1\bar{1}00]$ directions. The schematic of the experiments are shown in Figure 1.3. The machined surfaces were observed using Scanning Electron Microscopy (SEM) and an optical microscope. Subsequently, the CDC was measured and compared to those machined surfaces generated only by a single cut [22].

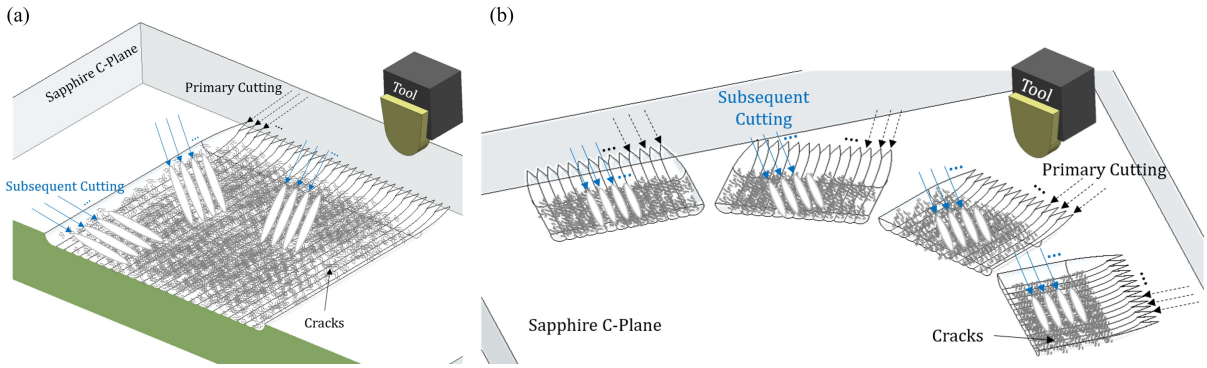

Figure 1.3: Schematic of subsequent machining experiments on C-plane of sapphire; (a) varying direction of subsequent cutting, (b) varying the direction of primary cutting [20].

In certain combination of cutting directions, an interesting phenomenon was observed where a large portion of the visible cracks generated by the primary cut was removed by the subsequent plunge cut. This is illustrated in Figure 1.4 (a). This observation is thought to be caused by the change in cutting direction, which suppresses the initiation of new cracks, and the material volume with cracks from the first cut was so small that it was removed during subsequent machining. To investigate the effect of the subsequent cutting direction and variation in the critical depth, machining was conducted both on cracked surface areas and on a clean surface as presented in Figure 1.4 (b). In the graph, O-CDC represents the critical depth for the case without any primary cutting and S-CDC represents the critical depth of the subsequent cut. From the figure, it is clear that the CDC decreased for machining on cracked surfaces in all the cutting directions. This observation was likely due to the existing damage from the first cuts that produces many surface and subsurface flaws initiating new cracks at lower levels of stress during subsequent machining. The 30° subsequent cutting direction showed a much smaller critical depth after subsequent cutting compared to the other directions. This observation may be caused because the flaws generated during the primary cutting were aligned in the 30° direction through the pile-up glide mechanism [23]. This is illustrated in the inset images in Figure 1.4 (b). During the subsequent cutting in the 30° direction, the aligned flaws are thought to initiate cracks more easily than in any other directions.

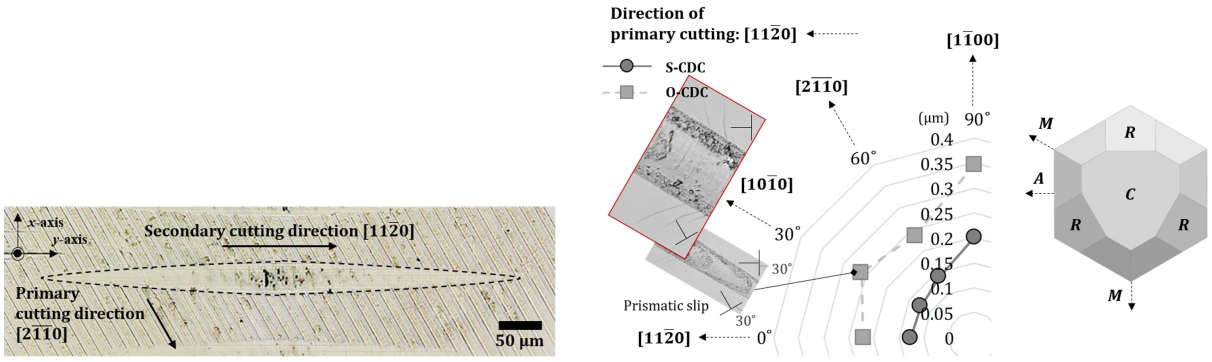

Figure 1.4: Effects of subsequent cutting; (a) optical image of subsequent cutting on C-plane of sapphire, (b) variation in critical depth based on direction of subsequent cutting [22].

It was also found that the primary cuts in the 90° direction generate lamellar cracks perpendicular to the cutting direction (See Figure 1.5 (a)). However, when the subsequent machining

was performed in the 90° direction on cracked surface areas pre-machined in the 0° direction, the type of crack changed from lamellar to concave, similar to that observed in the 30° machining as shown in Figure 1.5 (b). This phenomenon is thought to have occurred as the thrust force was not large enough to suppress crack opening in the $[10\bar{1}0]$ direction. This example clearly illustrates that surface and subsurface damages accumulated through primary machining strongly affects the material response during subsequent machining operations. In the second set of experiments where the direction of primary cutting was changed, the crack morphology showed some variations on the different cracked surface areas, which can be attributed to the anisotropy of the sapphire crystal. This, in turn, can cause varying amounts of surface and subsurface damage. The variation in the critical depth is also presented in Figure 1.5 (c), which clearly shows that the CDC in the 0° direction for the subsequent cutting substantially reduced from the value in the the primary cut whereas the CDC for the subsequent cutting in the other directions is very similar to the critical depth for the primary cuts. It was conjectured that these observations may be caused by the activation of the rhombohedral twinning systems, which is known to promote plastic deformation [23]. In the 0° direction, the flaws generated by the primary cutting aligned with the subsequent cut, thus easily generating new cracks and reducing the critical depth.

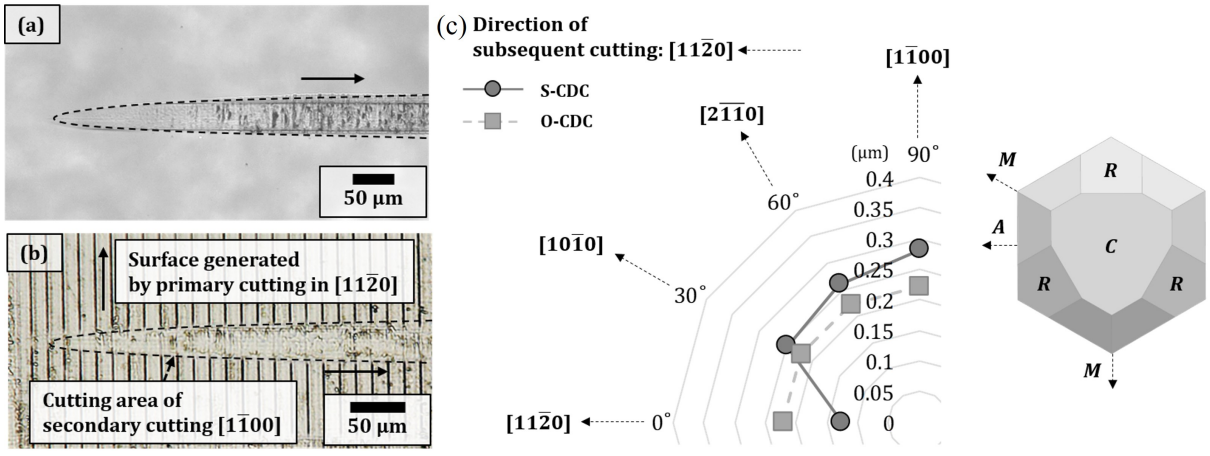

Figure 1.5: Comparison of surface morphology; (a) without primary cutting, (b) with primary cutting, and (c) variation in critical depth based on direction of primary cutting [22].

In the quest to machine ceramic materials more efficiently, it is imperative to fully understand material deformation during the machining process. However, as demonstrated by the

preliminary experiments, material removal is a complex and dynamic process depending on a lot of factors including the cutting direction, depth of cut, and other process parameters. It was also interesting to observe the influence prior machining operations can have on material deformation in terms of premature crack initiation, change in crack morphology and effect on the CDC. These observations indicate that factors such as residual stress and subsurface damage, not observed through SEM or optical microscope evaluations need to be accounted for in order to develop a complete understanding of material deformation during UPM. In this pursuit, the present research will focus on understanding the mechanisms leading to residual stress and subsurface damage formation, and develop procedures to quantify these phenomenon.

1.2 Hypothesis

Based on the knowledge gained from previous work, a couple of hypotheses were proposed at the start of the current research. Firstly, since it is known that plastic deformation is one of the main contributors to residual stresses and that plastic deformation is anisotropic during machining of single crystal ceramics, it was hypothesized that the **residual stresses and subsurface damage left behind after UPM of ceramics are anisotropic in terms of depth and direction of machining**. Another important aspect to consider during the machining process is chip formation and crack initiation beyond the CDC which contributes to the removal of some of the plastically deformed material from the workpiece surface. Combining this knowledge with the anisotropic material deformation caused by activation of specific slip/twinning mechanisms, it was hypothesized that the **residual stress magnitude is proportional to the amount of plastically deformed material remaining in the workpiece post machining.**

Based on the second hypothesis, for those cutting directions in which the plastically deformed region extends deeper into the subsurface, the magnitude of residual stress would be higher. One way to determine this would be to look at the activation of slip/twinning systems for a given cutting direction. As illustrated in Figure 1.6, for those cutting directions that dominantly activate slip/twinning systems that form a shallow angle with respect to the workpiece surface, the region of plastically deformed material is generally close to the surface and is removed by chip formation at low depths of cut or by fracture beyond the CDC. This scenario is hypothesized to have a low magnitude of residual stress. On the contrary, for those cutting directions which

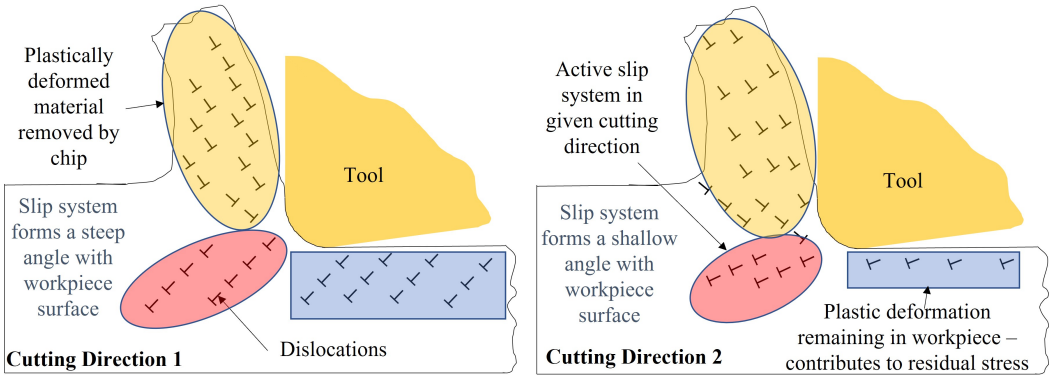

Figure 1.6: Schematic showing the initiation and evolution of two different slip systems during UPM of a single crystal ceramic [24].

activate plastic deformation mechanisms which form steep angles with the workpiece surface, the plastically deformed region would extend deeper into the subsurface and a significant portion of it would not be removed by chip formation or fracture, leading to a higher magnitude of residual stress. In some cutting directions where multiple slip/twinning systems have a similar or low probability of activation, there is a chance of dislocation entanglement causing plastic deformation to be concentrated close to the workpiece surface leading to lower magnitude of residual stress [25].

1.3 Objectives

The overarching goal of this work is to test the hypothesis presented in section 1.2 and understand if, and how residual stresses and subsurface damage influence the outcome of machining process of single crystal ceramics. In particular, this study aims to look at residual stress and subsurface damage formation from the lens of crystal plasticity and single crystal deformation, in order to better understand the relationship between crystalline structure and subsurface deformation during UPM. Based on the knowledge gained through this process, this study also aims to understand if machining strategies can be devised to minimize or control residual stress and subsurface damage magnitude by controlling the material deformation.

1.4 Thesis Organization

This section details the organization of the dissertation. The main contents of this work are organized into four chapters and a brief summary of the chapters are provided in the following paragraphs.

Chapter 2 introduces the reader to the materials and methods used throughout this work. This chapter is divided into 4 sections. In the first section, the two candidate ceramics used in this study - sapphire and 8-mol % yttria stabilized zirconia (8YSZ) are described in terms of their crystal structure, applications, followed by the different deformation mechanisms present in these materials. The second section contains the methodology used to predict the activation of different deformation mechanisms in a single crystal subject to a stress using concepts from crystal plasticity. In the third section, details about the ultra-precision machining setup are provided along with the rationale behind many choices in terms of tool, machining process parameters, and overall setup. In the final section, details about the Molecular Dynamics (MD) simulations carried out in collaboration with colleagues at the University of Cincinnati are described. The results and analysis of the MD simulations are presented in chapter 4.

Chapter 3 delves into the details of residual stress measurements in sapphire and 8YSZ. This chapter is broadly divided into three sections. The first section is a literature survey on residual stress measurements across various relevant domains such as single crystals, ceramics, and machined components, as well as the pros and cons of different measurement techniques available. The second section focuses on residual stress measurements and analysis in sapphire. In the first part of this section, details about Raman spectroscopy are provided, along with the measurement parameter selection methodology. Following this, results of the residual stress magnitude for different cutting directions and depths of cut are discussed. These results are then explained from a perspective of material deformation and crystal plasticity. Towards the end of this section, an approach to calculate the residual stress tensor using Raman spectroscopy data is discussed for selected cases. The third section focuses on residual stress measurements in 8YSZ. As Raman spectroscopy was not suitable for residual stress measurements in 8YSZ, the nano-indentation technique was used. In this section, the different analysis approaches in residual stress measurement through nano-indentation are discussed and the analysis for two

approaches - fracture toughness based and energy based are presented.

Chapter 4 details the investigation of subsurface damage in the case of sapphire. This chapter is divided into 4 sections. The first section is a literature review on subsurface damage evaluation in machined ceramics and the different techniques used to measure subsurface damage. The second section describes the use of Raman spectroscopy to understand subsurface deformation in sapphire and the effect of crystallography in this regard. The results in this section examine the effect of cutting direction, depth of cut, and crack morphology on the extent of subsurface damage. In the following section, the results and analysis of MD simulations are presented and compared with the results from previous sections and chapter 3. The final section of the chapter delves into Transmission Electron Microscopy (TEM) evaluation of subsurface damage. The first part of this section contains a detailed description of TEM sample preparation as it was one of the challenges overcome during this work. A detailed description of the process parameters used during Focused Ion Beam (FIB) milling for TEM sample preparation is documented in the appendix (section A.3). Subsequently, the TEM results are discussed for different scenarios and evaluated from the perspective of material deformation introduced in chapters 2 and 3.

Chapter 5 examines the effect of different machining process parameters on residual stresses, surface, and subsurface damage. The motivation behind the contents of this chapter was to think of the practical aspects of machining single crystal ceramics and evaluate a few of the scenarios that could be encountered while machining a functional part. In this section, the effect of horizontal and vertical overlapping cutting on the surface morphology is presented. Additionally, a machining strategy to minimize residual stress magnitude while improving the machining throughput is discussed.

Chapter 2

Materials and Methods

Having developed an understanding of the problem statement and motivation for this study in Chapter 1, Chapter 2 introduces the reader to the materials and methods used in this study and provides the rationale behind different choices made over the course of this work, in terms of choosing specific process parameters, tool geometries, tool paths, etc.

To begin with, details about the materials chosen - sapphire and 8YSZ are presented, highlighting the crystal structure, physical properties, applications, and deformation mechanisms. Subsequently, deformation in single crystals is discussed from the perspective of plastic deformation and fracture, and methods to predict which deformation system is likely to get activated on application of a stress to the single crystal material. Next, the experimental setup used to test the hypothesis detailed in section 1.2 is described in detail. Unless specified otherwise, all the experiments in subsequent chapters were conducted following the procedure detailed in this chapter, including tool geometry, process parameters, cutting environment, and tool path. Finally, details about the MD simulations performed by colleagues at the University of Cincinnati as part of a collaborative project are presented. The results from the MD simulations were especially beneficial in understanding the activation of different deformation mechanisms in the tool-workpiece interface and evolution of subsurface damage.

2.1 Crystal Structure and Material Properties

In the case of conventional machining, many theories have been proposed to understand material deformation based on the shearing occurring at different regions in the tool-workpiece interface. However, when the scale of machining is reduced from the conventional to micrometer level and further down to the nanometer scale, additional effects such as tool edge rounding, grain boundaries, material phases, crystal structure, and lattice defects need to be taken into account [26, 27]. These factors are especially true with single crystalline materials where low crystal symmetry can result in pronounced crystal anisotropy [28]. Furthermore, the crystalline

arrangement of atoms influences the bond strength between atoms which in turn influences the activation of different slip and fracture mechanisms on application of a load. In this section, two candidate materials - sapphire and 8YSZ are described from the perspective of their crystal structure, material properties, applications, and deformation mechanisms.

2.1.1 Sapphire

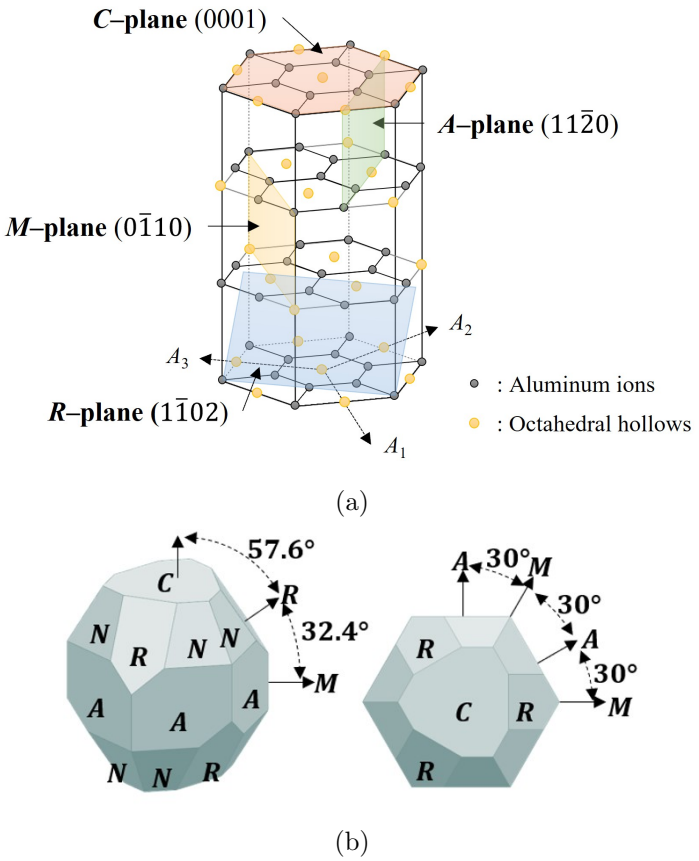

Figure 2.1: (a) Unit cell of sapphire showing the 4 commonly used functional crystallographic planes; (b) Schematic showing the angular relationships between different crystallographic planes [29, 30].

Sapphire (α-Al_2O_3) is the single crystal form of aluminum oxide in which it is renowned for its high hardness, high melting point, wear and chemical resistance, and bio-compatibility [31–33]. Additionally, a high Young's modulus and resistance to thermal shock resistance prompt its use in structural applications under harsh environments [29, 34]. The impressive properties of sapphire can be attributed to the unique crystal structure of sapphire belonging to the ditrigonal-scalenohedral crystal class of trigonal symmetry ($D^6_{3d} - R\bar{3}C$). The structure with this spatial

symmetry group can be considered as a slightly distorted hexagonal closed packing comprising of Al^{3+} and O^{2-} ions with coordination numbers of 6 and 4 respectively. In the unit cell of sapphire, the oxygen ions occupy the lattice points of the hexagonal unit cell, whereas the aluminum ions occupy two-thirds of the interstitial octahedral hollows between the close-packed oxygen ions [29]. As per various mechanical and optical properties in the different crystallographic orientations, 4 functional crystallographic planes are commonly used in industry and are labeled A-, C-, M-, and R-. In common terminology, the C-plane is also referred to as the basal plane, A- and M-planes are known as prismatic planes, and the R-plane is also called the rhombohedral plane. The basal plane is perpendicular to the prismatic planes and forms an angle of 57.6° with the rhombohedral plane. The hexagonal unit cell and 4 functional crystallographic planes, and the angular relationships between the crystallographic planes are shown in Figure 2.1.

Based on the various properties of sapphire, it is used in a variety of applications ranging from optics and semiconductors to biomedical implants and space craft structures. Specifically, owing to the scratch resistance and high optical transparency in the 200-5000 nm wavelength range, sapphire is used as a protective window in different devices such as fingerprint sensors, cameras, watches, and some electronic devices [35, 36]. Given the low coefficient of friction and high wear resistance, sapphire is used as a friction pair in bearings in micro-mechanisms such as those found in mechanical watches [37]. As a bio-compatible and chemically inert material, sapphire is gaining popularity in the field of biomedical implants as recent studies have shown promising results of new and rapid tissue growth on sapphire substrates [38]. Given the high operating temperature of sapphire, it is used for structural components in specialized scientific equipment like the Faraday cup on NASA's Parker Solar Probe [39] being used to study solar wind and coronal plasma. Further, the high dielectric strength and ability to produce wafers with sub-nanometer surface roughness make sapphire the ideal candidate for many semiconductor applications such as substrates for blue LEDs and laser diodes [40].

Looking at applications based on the crystallographic orientations of sapphire, the A-plane of sapphire has been found to be a good substrate to grow carbon nano-tubes and in microelectronic applications where an uniform dielectric constant is required [41]. The C-plane of sapphire is the most widely used orientation and is commonly found across applications, from optical windows to LED substrates and infrared detectors [42]. The M-plane of sapphire has been

found to be suitable for use as a high temperature superconducting filter and for growing non-polar/semi-polar plane epitaxial layers [43]. The R-plane of sapphire is commonly used for hetro-epitaxial deposition of silicon in microelectronic IC devices [44]. The R-plane is also used in high impedance resistors and superconducting components [45].

Table 2.1: Slip/Twinning systems in single crystal sapphire [46].

Slip/Twinning System	**Miller-Bravais Indices**	**Critical Resolved Shear Stress (CRSS) [MPa]**
Basal Twinning (C-plane)	$\{0001\}\langle\bar{1}010\rangle$	2.2255
Basal Slip (C-plane)	$\{0001\}\langle11\bar{2}0\rangle$	2.2255
Pyramidal Slip (P-Plane)	$\{0\bar{1}11\}\langle10\bar{1}1\rangle$	4.4817
Prismatic Slip (A-plane)	$\{11\bar{2}0\}\langle10\bar{1}0\rangle$	1.6487
Rhombohedral Twinning (R-plane)	$\{1\bar{1}0\bar{2}\}\langle1\bar{1}0\bar{1}\rangle$	0.4066

Table 2.2: Cleavage systems in single crystal sapphire [46, 47].

Cleavage System	**Miller-Bravais Indices**	**Critical Stress Intensity Factor (CSIF) [MPa.m$^{0.5}$]**	**Fracture Energy [J/m^2]**
Basal Cleavage (C-plane)	(0001)	4.54	>40
Prismatic Cleavage 1 (A-plane)	$\{11\bar{2}0\}$	2.43	-
Prismatic Cleavage 2 (M-plane)	$\{10\bar{1}0\}$	3.14	7.3
Rhombohedral Cleavage (R-plane)	$\{\bar{1}012\}$	2.38	6

In order to produce the required geometries in sapphire or other single crystal ceramics for the various applications listed, subtractive manufacturing processes involving material removal from a larger workpiece are most commonly used. In order to improve the throughput of these manufacturing processes, it is imperative to understand how the materials deform during application of stresses and load in these processes. Generally, material removal and deformation occurs either through plastic deformation or fracture and depending on the ceramic, are governed

by certain threshold values of stress which need to be met for deformation to occur. Further, in single crystals, plastic deformation and fracture can occur only along specific crystallographic orientations. Details about the different plastic deformation mechanisms in sapphire and the Critical Resolved Shear Stress (CRSS) required to activate a given mechanism is listed in Table 2.1. Similarly, the different cleavage fracture systems present in sapphire and the corresponding Critical Stress Intensity Factor (CSIF) or fracture energy needed to initiate a crack along the different cleavage planes is listed in Table 2.2. The correlation between these values and the prediction of deformation activation is detailed in Section 2.2.

2.1.2 Yttria-stabilized zirconia

As a second candidate material for this study, 8-mol % yttria stabilized zirconia (8YSZ) was selected. The main reason for choosing 8YSZ was due to the substantially different crystal structure compared to sapphire. Further, 8YSZ is also gaining popularity in many key industries such as clean energy and electrolysis which peaked our attention. In summary, we wanted to test whether the hypothesis presented in Section 1.2 is applicable to single crystals with different crystallography and composition.

Zirconia or zirconium oxide (ZrO_2) on its own is a very interesting material as it undergoes phase transitions depending on the temperature and stresses, and each of these phases have unique properties and applications. The most common temperature dependent polymorphs are - monooclinic ($P2_1/c$ space group) at temperatures below 950 °C, tetragonal ($P4_2/nmc$ space group) between 1200-2370 °C which is a metastable phase, and cubic ($Fm-3m$ space group above 2370 °C [48]. As this polymorphism can cause large volumetric changes and property variations during processing, oxide materials such as yttrium oxide (Y_2O_3), calcium oxide (CaO), and magnesium oxide (MgO) are added in small quantities to stabilize the cubic or tetragonal phases at room temperature depending on the concentration [49]. It is noted that stabilizing the tetragonal or cubic phases through alloying is responsible for a low, temperature independent thermal conductivity, which greatly increases the ionic conductivity, and improves the fracture toughness by many fold [50].

From the variety of options in terms of dopant composition, fractions, and stabilized crystalline structure, the cubic structure formed by doping zirconia with 8-mol % of yttria (8YSZ)

was chosen for this study as this composition is one of the most commonly used forms of YSZ across industries. 8YSZ has a fluorite crystal structure where the zirconium ions occupy the face-centered cubic positions and the oxygen ions occupy the tetrahedral interstitial sites. Upon addition of yttria, 8% of the zirconium ions (Zr^{4+}) are replaced by yttrium ions (Y^{3+}) and in this process, oxygen vacancies are created to maintain charge neutrality. These oxygen vacancies make 8YSZ a good ionic conductor [51].The crystalline structure and unit cell of 8YSZ is shown in Figure 2.2

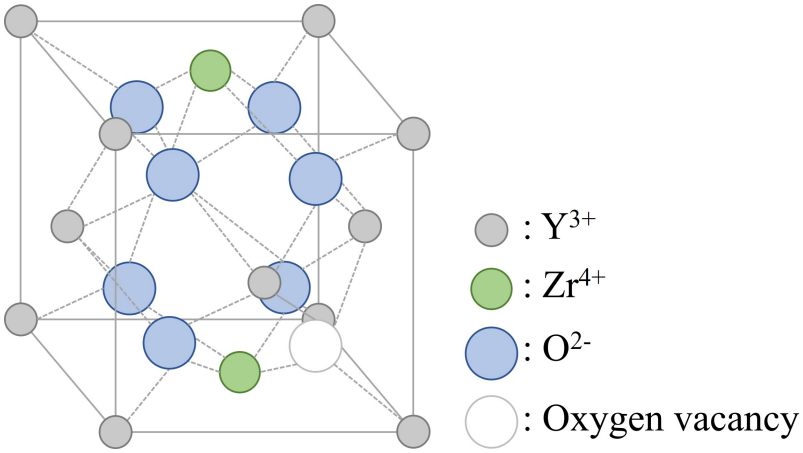

Figure 2.2: Unit cell of 8YSZ [52].

Owing to the high fracture toughness, 8YSZ is commonly used in dental and orthopedic implants. Further, in the polycrystalline form, 8YSZ has a natural color that can be matched to the enamel [53]. Further, owing to the high melting point of >2600 °C, 8YSZ is commonly used in many thermal barrier coatings in jet engines and gas turbines [54]. Further, 8YSZ is gaining a lot of popularity as a seed crystal for synthetic diamond growth and as a diamond substitute in the jewelry industry because of its high refractive index and crystallographic isometry [55]. Due to the high ionic conductivity, 8YSZ is used as the solid electrolyte in a Solid Oxide Fuel Cell (SOFC) where chemical energy of a fuel (hydrogen) is directly transformed into electricity by reacting with the oxygen ions to release electrons and form water vapor [56]. Further, the ion-conducting properties of 8YSZ lead to it's use in oxygen sensing applications such as exhaust gas monitors and for pH measurement in high-temperature water [57]. In spite of the pronounced fracture toughness and hardness, it should be noted that some research points to material degradation due to aging and exposure to moisture over long periods of time which is accentuated

at higher temperature, but further study is required to fully understand the wear/degradation mechanisms involved, and the effect of different dopants and their concentration on the long term degradation behavior [50].

Similar to sapphire, the deformation in 8YSZ needs to be investigated from the point of view of the available slip and fracture systems. Details about the different plastic deformation mechanisms in 8YSZ and the critical resolved shear stress required to activate a given mechanism is listed in Table 2.3. Similarly, the different cleavage fracture systems present in 8YSZ and the corresponding critical stress intensity factor needed to initiate a crack along the different cleavage planes is listed in Table 2.4.

Table 2.3: Slip systems in 8YSZ [58].

Slip System	**Miller-Bravais Indices**	**Critical Resolved Shear Stress (CRSS) [MPa]**
Primary	$\{001\}\langle 110\rangle$	3.0
Secondary	$\{110\}\langle \overline{1}10\rangle$	4.6
Secondary	$\{111\}\langle \overline{1}10\rangle$	Active at higher temperatures

Table 2.4: Cleavage systems in 8YSZ [59, 60].

Cleavage System	**Critical Stress Intensity Factor (CSIF) [MPa.m$^{0.5}$]**
(001)	1.90
$\{110\}$	1.10
$\{111\}$	1.5

2.2 Predicting Deformation Behavior in Single Crystal Ceramics During Machining

Deformation in crystalline materials are primarily driven by the presence of preexisting defects like dislocations, micro-cracks, or stacking faults and are a function of the density of these defects, strain rate, and temperature [61]. Given the orderly arrangement of atoms in a single crystal, deformation is energetically favorable only along specific crystallographic directions. In

this section, the deformation of single crystal ceramics is introduced from the perspective of crystal plasticity, particularly looking from the perspective of activation of different slip and fracture mechanisms.

2.2.1 Plastic Deformation

In single crystals, when a load is applied, plastic deformation in the form of slip or twinning occurs on well defined slip/twinning planes and in specific crystallographic directions. The tendency of activation of different slip/twinning mechanisms is governed by the Schmid Law which says that the dominant deformation mechanism will be the system on which the resolved stress exceeds the Critical Resolved Shear Stress (CRSS) (See tables 2.1 and 2.3). Mathematically, Schmid's law is represented by the following equations:

$$\tau_s = \sigma m \tag{2.1}$$

$$m = \cos\phi \cos\lambda \tag{2.2}$$

Where τ_s is the resolved shear stress, σ is the applied stress, m is the Schmid factor, ϕ is the angle between the slip plane normal and the direction of applied stress, and λ is the angle between the direction of applied stress and the slip direction. Schematically, the Schmid law is represented in Figure 2.3 [62].

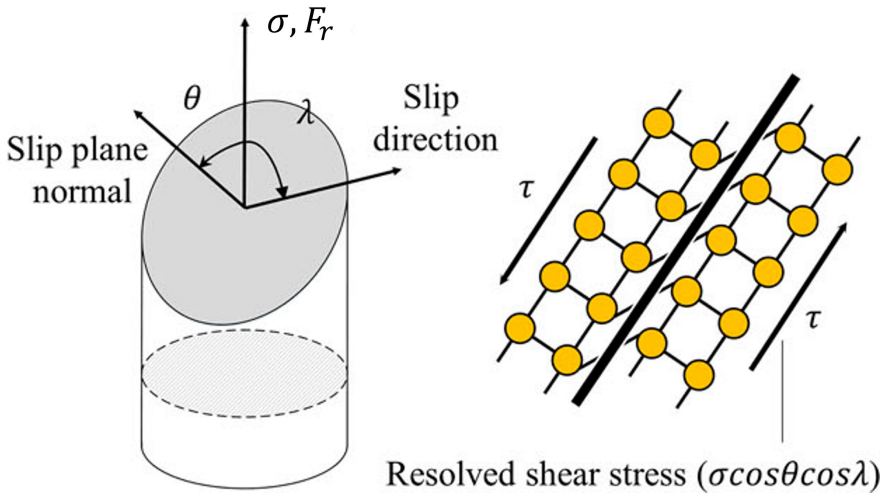

Figure 2.3: Slip/twinning activation in single crystals based on the Schmid Law [63].

Multiple researchers have used this approach to understand the plastic deformation during UPM. Mizumoto et al. followed an approach of using a weighted Schmid factor and CRSS values to calculate the slip/twinning system with highest probability of activation [23]. In this approach, the resolved shear stress is calculated using the resultant force during machining which is obtained from the cutting and thrust forces measured using a dynamometer. However, one of the drawbacks of this approach was that it did not consider the small variations in the direction of the resultant force over time during the machining operation. This was addressed in the work by Kwon et al. [63], where the variation in resultant force direction was accounted for by the following equation:

$$\theta_{force} = \arctan F_t/F_c \tag{2.3}$$

where F_c is the cutting force, F_t is the thrust force, and θ_{force} is the angle between the resultant force and the cutting force. In this approach, commonly, the probability of activation of any slip/twinning system is represented over time. Subsequently, the likelihood of activation of different slip and twinning systems can be calculated using Eq. 2.4,

$$P_i' = \frac{m_i'}{\tau_i^{crit}/min_i\tau_i^{crit}} \tag{2.4}$$

where P_i' is defined as the plastic deformation parameter which represents the probability of activation of the i^{th} slip or twinning system, m_i' is the modified Schmid factor which considers the projection made by the resultant machining force with a given slip/twinning system and τ_i^{crit} is the critical resolved shear stress of the i^{th} slip or twinning system. Based on the calculation, the slip/twinning system with the highest probability is most likely to get activated for the given cutting direction and at the specific depth of cut. This is the approach used throughout the dissertation.

2.2.2 Fracture

The second mode of deformation, commonly observed during machining of hard and brittle ceramics is fracture. In the original theory of fracture proposed by Griffith in 1921, it was theorized that a fracture can be characterized by the conversion of elastic strain energy to

surface energy and crack opening occurs only if the decrease in elastic strain energy exceeds the increase in surface energy for an incremental increase in the crack length [64]. However, subsequent research has shown that this theory is applicable mostly to amorphous materials as the plasticity at the crack tip resulting from high stress concentration is not accounted for [65]. One of the factors used to address this issue in the case of crystalline materials is the stress intensity factor which represents the severity of stress at the crack tip. Akin to the critical resolved shear stress in plastic deformation, stress above a threshold Critical Stress Intensity Factor (CSIF) is necessary for crack initiation (see Tables 2.2 and 2.4) and like the slip/twinning systems, cleavage fracture occurs only along well defined crystallographic planes where the bonding between the atoms is weak. The CSIF value depends on the mode of crack opening and can be calculated using the following equation for mode I cracks (purely tensile loading):

$$K_I = \sigma_N \sqrt{\pi a} \cos^2 \beta \tag{2.5}$$

where K_I is the stress intensity factor for mode I crack opening, σ_N is the applied tensile stress, a is the half-length of initial flaw already existing in the material, and β is the angle between the direction of applied stress and the normal direction to the flaw. This is schematically represented in Figure 2.4.

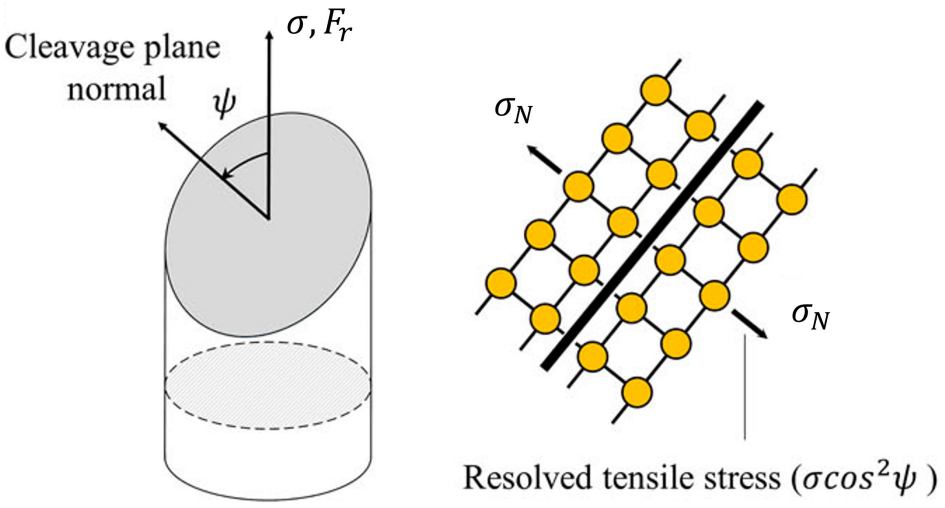

Figure 2.4: Fracture activation in single crystals for an applied stress σ_N [63].

In terms of predicting the most likely cleavage fracture system to get activated during machining, a similar approach to the one followed for plastic deformation (section 2.2.1) is taken. Analogous to the Schmid factor, a term called the cleavage factor was defined by Mizumoto et al. [23]. The cleavage fracture is calculated using the following equation:

$$c = \cos^2 \psi \tag{2.6}$$

where c is the cleavage factor and ψ is the angle between the direction of applied stress and the normal to the cleavage plane. In a similar fashion, Mizumoto et al. developed an equation to calculate the likelihood of activation of different fracture systems and used the fracture energy for different cleavage fracture systems as the threshold parameter. However, due to non-availability of experimental data for all different cleavage systems in sapphire, Yoon et al. switched to using the critical stress intensity factor [30]. However, these two approaches still did not consider the variation in the resultant force direction as discussed in section 2.2.1. This was addressed in the work by Kwon et al. [63] and is the method followed in this work. The probability of activation of any cleavage system is calculated using the following equation:

$$F'_j = \frac{c'_j}{K_{ICj}/min_j K_{ICj}} \tag{2.7}$$

where F'_j is defined as the cleavage fracture parameter which represents the probability of activation of the j^{th} fracture system, c'_j is the modified cleavage factor which considers the projection made by the resultant machining force with a given fracture system and K_{ICj} is the critical stress intensity factor of the j^{th} cleavage fracture system. Based on the calculation, the cleavage fracture system with the highest probability is most likely to get activated for the given cutting direction and at the specific depth of cut.

2.3 Experimental Setup

As described in Chapter 1, ceramics exhibit the ductile-brittle transition phenomenon at very small deformation scales, generally in the order of a few hundred nanometers. Subsequently, to machine ceramics in the ductile regime, a highly precise machine tool with a command resolution at least an order of magnitude below the ductile-brittle transition depth is necessary.

Throughout this study, one such ultra-precision machine tool, the FANUC ROBONANO α-0iB (FANUC Corporation, Japan) was used for all the cutting experiments. This machine tool is a 5-axis CNC machine with a command resolution of 1 nm in the three linear axes and 1 microdegree command resolution in the 2 rotary axes which provide adequate control over the ductile-brittle transition depth during machining. While machining at these small scales, there are many environmental factors that can affect the outcome of the machining process, such as vibrations, temperature differences, and friction or backlash among machine components. In the ROBONANO, each of these potential causes of variations are addressed through thoughtful and innovative design features. To minimize the effect of vibrations, the machine tool is located in a room where the floor is isolated from the rest of the building. Additionally, the machine has active dampers that cancel out any vibrations from the immediate vicinity of the machine. To account for variations in temperature, the machine is located inside a thermal enclosure where the temperature is maintained at 23 $\pm$ 1 °C. To address the issue of friction and backlash in the machine drives, the machine tool utilizes linear motors and drives mounted on air bearings which prevent physical contact between the drive components and eliminate the need for ball screws where backlash errors are prominent. The machine installation is shown in Figure 2.5.

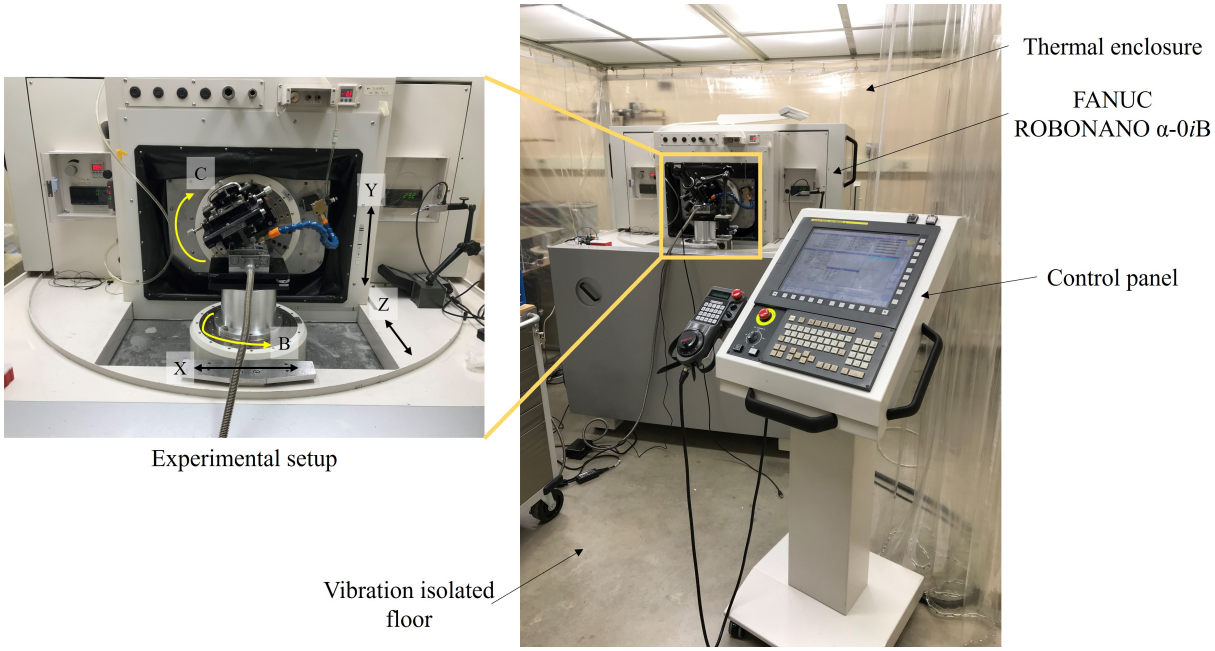

Figure 2.5: FANUC ROBONANO α-0iB machine installation and overview of experimental setup.

In the experiment setup used throughout this dissertation, 10 mm x 10 mm x 0.5 mm single crystal ceramic substrates (M.T.I Corp., U.S.A) produced by Czochralski technique and cut into different crystallographic orientations were used. Both sides of the substrate were polished using CMP process by the vendor. In the case of sapphire, the orientations used were A-plane $\{11\bar{2}0\}$, C-plane (0001), M-plane $\{10\bar{1}0\}$, and R-plane $\{10\bar{1}2\}$. For 8YSZ, the crystallographic orientations used were {001} and {110}. These crystallographic orientations were chosen based on the commonly used orientations across different applications of sapphire and 8YSZ described in Section 2.1.

To successfully machine hard and brittle ceramics such as sapphire and 8YSZ, it is imperative to use a cutting tool that is much harder than the workpiece. With a Mohs hardness of 9 (maximum possible is 10), not many options are available in terms of tool materials other than diamond. Among diamond tools, multiple options are available such as Single Crystalline Diamond (SCD), Polycrystalline Diamond (PCD), nano-twinned diamond, etc. [66, 67]. Generally, single crystalline diamond tools have the best dimensional stability and can be ground and honed to have extremely fine cutting edges, thus resulting in excellent surface finish post machining. However, due to the single crystal nature of the tool, catastrophic failure of the tool due to large stresses is a common occurrence, especially while machining hard and brittle ceramics. On the other hand, conventional polycrystalline diamond tools that are produced by sintering diamond grains (1-20 μm) held together by a cobalt binder are widely used in industry. Although, fracture in this case is localized due to the relatively ductile cobalt binder and intergranular fracture failure mode, it is much harder to grind a sharp cutting edge that holds its form due to the larger diamond grain size. Further, the PCD tools possess a lower hardness and thermal shock resistance compared to the single crystalline diamond tool [66]. With recent advances in material science, the above mentioned problems have been solved by reducing the grain size of the diamond to the nanometer scale and developing a method to sinter the nanosized grains without a binder. It has been shown that these binderless nano-PCD tools have a hardness comparable to the single crystalline diamond tools and a higher fracture resistance compared to both single crystalline and conventional poly crystalline diamond tools. The cutting tools used throughout this study were binderless nano-PCD tools with a 0.5 mm nose radius, 0° rake angle, 7° clearance angle, and a 10 mm x 10 mm carbide shank (A.L.M.T. Corp., Japan). The

edge radius of this tool is in the range of 400 - 600 nm. An image of the tool is shown in Figure 2.6.

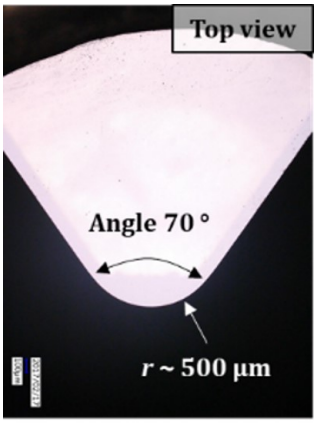

Figure 2.6: Optical microscope image of rake face of binderless nano-PCD tool used in the cutting experiments. [68].

In the cutting experiments, the tool was mounted in a purpose-built scribing tool holder attached to the C-axis of the FANUC ROBONANO machine tool. The ceramic substrates were attached to an aluminum plate using machining wax (SHIFTWAX series, Nikka Seiko Co. Ltd., Japan). The aluminum plate was mounted on a piezoelectric dynamometer (Type 911AA1, Kistler Instrument Corp., Switzerland) which was in turn connected to a charge amplifier with low pass filter (Type 5080A, Kistler Instrument Corp., Switzerland). The dynamometer played a crucial role in measuring the cutting forces that was used to understand and model the material deformation during machining as described in section 2.2. Since the machining process was carried at depths of hundreds of nanometers, it was essential to ensure flatness across the workpiece surface to ensure consistent machining depths. To achieve this, the dynamometer was mounted on a tilt stage with manual pitch and roll control (AIS-1016B, OptoSigma Corporation, USA). This assembly was attached to a fixture mounted on the B-axis of the machine tool. To ensure flatness of the workpiece, the variation in surface height was measured using a digital surface probe with 0.1 μm resolution (Brown & Sharpe 599-988 indicator probe used with Tesatronic TT10 display, TESA Technology, Switzerland). Once the flatness was established, tool-workpiece contact was established using an optical microscope (SH140CCD-2R, Shodensha Inc., Japan). Additionally, during the experiments, the dynamometer also aided in establishing accurate tool-workpiece contact and controlling the depth of cut during machining by monitor-

ing the force signal in real time and correlating the temporal variation of cutting force with the programmed tool path. The cutting direction was varied by rotating the B-axis of the machine tool. The experimental setup used is shown in Figure 2.7.

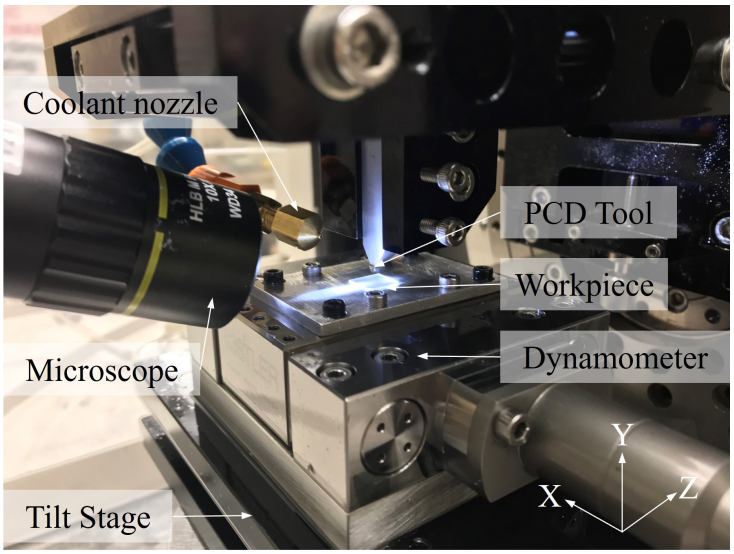

(a)

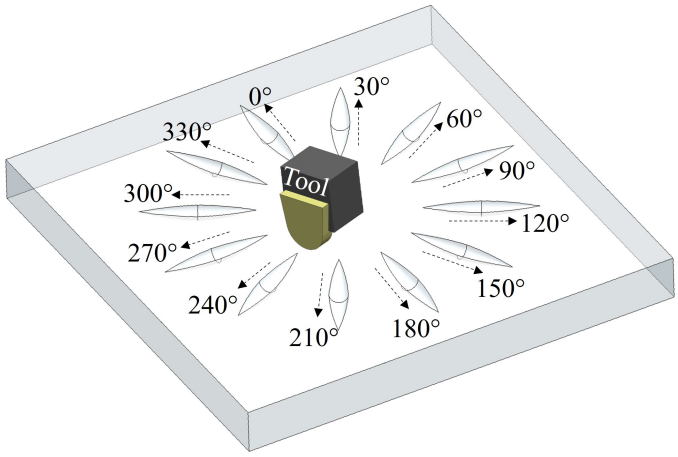

(b)

Figure 2.7: (a) Experimental setup used for ultra-precision machining of ceramic substrates; (b) schematic of cutting in different crystallographic directions [20, 69].

The tool path used for most of the experiments was a plunge cut, as shown in Figure 2.8. The cutting involved gradually increasing the depth of cut up to a value of 500 nm and retracting the tool back to the surface gradually. The slope on these cuts was selected to be 1/500 to limit the increase in stress on the tool cutting edge and subsequently minimizing the chance

of edge chipping or gross fracture. In some cases, the tool path was modified to study specific phenomenon and the variations are described in the respective sections of this dissertation. For the experiments relevant to this work, a cutting speed of 5 mm/min was used. Additionally, cutting was performed under the condition of flood coolant to maximize chip evacuation from the cutting region. For this purpose, a mineral oil based cutting fluid was used (Metal Work HS, JX Nippon Oil & Energy, Japan). The machined surfaces were observed using an optical microscope (VHX 5000, Keyence Corp., Japan) and a scanning electron microscope (LEO 1530, Carl Zeiss GmbH, Germany). The key experimental parameters used in this study are summarized in Table 2.5. It must be noted that Suk Bum Kwon assisted in taking some of the SEM images used in this study. Some of the SEM images or a version of them have been used in a couple of previously published studies [63, 70]. In the published works, the SEM images were used to validate the correlation between the forces/stresses during UPM of sapphire and different cleavage systems activated. In this work, the SEM images are used to better understand how crack morphology affects the subsurface damage and are compared with measurements from Raman spectroscopy and TEM evaluations.

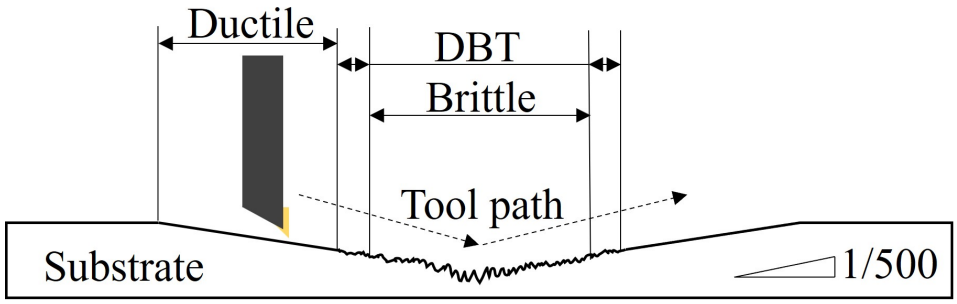

Figure 2.8: Tool path used for plunge cutting [24].

2.4 Molecular Dynamics (MD) Simulations

MD Simulations were designed, setup, and run by Prof. Woo Kyun Kim, Dalei Xi, and Yiyang Du at the University of Cincinnati as part of the collaborative NSF project under the grants CMMI-1844821 and CMMI-2008563 to study the effect of crystal anisotropy on subsurface damage and residual stress through experiments and MD simulations. The individual contribution relevant to this work are the analysis of subsurface damage depth for different

Table 2.5: Summary of machining process parameters and conditions.

Parameter	**Value**
Machine Tool	FANUC ROBONANO α-0iB
Cutting Tool Material	Binderless Nano-PCD
Tool Nose Radius	500 μm
Tool Rake Angle	0 °
Tool Clearance Angle	9°
Cutting Environment	Flood coolant with mineral oil
Cutting Speed	5 mm/min
Cutting Slope	1/500
Maximum Depth of Cut	500 nm

cutting directions and identification of activated deformation mechanisms in the different MD simulations. In this work, the MD simulations were limited to sapphire.

MD simulations of cutting were carried out on the C-, A-, and R-planes of sapphire using the Large-scale Atomistic/Molecular Massively Parallel Simulator (LAMMPS) software [71]. The simulation model consisted of the sapphire workpiece with approximate dimensions of 1500 Å x 30 Å x 1000 Å in the x, y, and z directions respectively comprising of around 4.5 million atoms. Interactions between the oxygen and aluminum atoms of sapphire were modeled using the Vashishta potential consisting two- and three-body terms. The Vashishta potential was selected due to it's capability to accurately describe different properties of sapphire such as elastic constants, bulk modulus, melting temperature, and cohesive energy [72]. Periodic Boundary Condition (PBC) was applied in the y direction to mimic the process of orthogonal cutting where no material flow is permitted around the sides of the tool. The outer most layers of atoms on one of the shorter edges and bottom of the substrate were fixed to prevent rigid body motion and a few layers of atoms adjacent to the fixed layer were assigned as a Langevin thermostat to absorb any excess heat produced by deformation.

The cutting tool comprised of about 68,500 carbon atoms arranged in the diamond cubic crystal structure. The tool was modeled as a rigid body to simplify the simulations. Subsequently, only the atoms at the edges of the tool were defined. The edge radius of the tool was 60

Å and the rake angle was defined to be -10°. The reason for selecting a negative rake angle on the tool in spite of the experimental tool having a 0° rake angle was to account for the effect of the cutting edge radius. As the experimental tool has a sizable edge radius compared to the depth of cut, the effective rake angle during cutting would inevitably be negative. Hence, it made logical sense to use a negative rake angle tool in the MD simulations. The atomic interactions between the tool and the workpiece (i.e. C-O and C-Al) were modeled using the Lennard-Jones potential [73]. An image of the MD simulation setup is shown in Figure 2.9.

The MD simulations of cutting were performed along different cutting directions on the C-, A-, and R-planes of sapphire at different depths of cut (100Å, 200 Å, 300 Å, and 400 Å) and cutting speeds (10 m/s and 100 m/s). However, the results analyzed in this work are limited to a cutting depth of 400 Å and a cutting speed of 100 m/s. The list of cutting simulations pertinent to this work are summarized in Table 2.6.

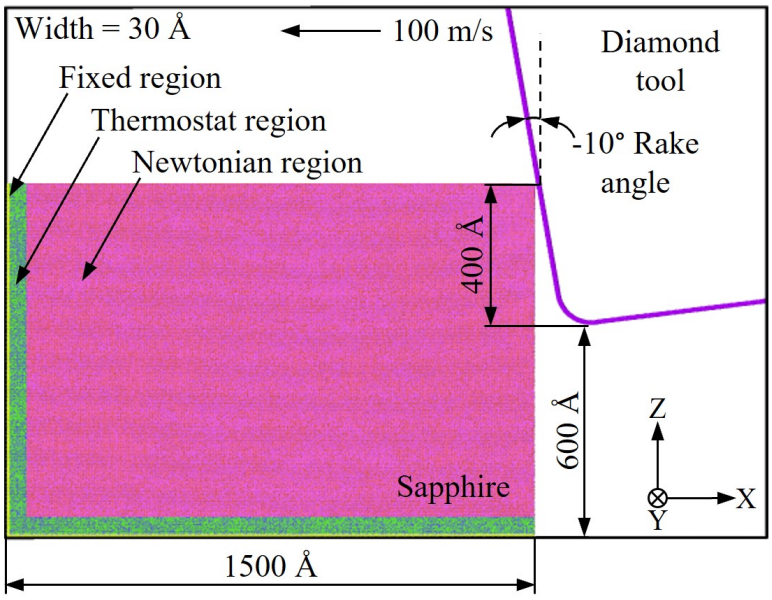

Figure 2.9: Schematic of MD simulation setup.

Table 2.6: Summary of different MD simulations analyzed in this work.

Cutting Plane	**Cutting Direction**	**Equivalent Experimental Representation**
C-plane	#1 - $[2\bar{1}\bar{1}0]$	C180
(0001)	#2 - $[01\bar{1}0]$	C270
A-plane	#1 - $[3\bar{3}01]$	A60
$\{11\bar{2}0\}$	#2 - $[1\bar{1}01]$	A120
R-plane	#1 - $[1\bar{1}00]$	R90
$\{01\bar{1}2\}$	#2 - $[\bar{1}\bar{1}20]$	R180
	#3 - $[1\bar{1}02]$	R270

Chapter 3

Residual Stress Measurements

As highlighted in section 1.1 in Chapter 1, the residual stresses and subsurface damage play an important role in influencing the material removal behavior during UPM of single crystal ceramics like sapphire. Further, it was also found that the crystal anisotropy has a role to play in influencing these parameters. The objective of this chapter is to quantify the residual stress magnitude for sapphire and 8YSZ under various cutting conditions and try to understand the effect material anisotropy and crystallography play in influencing the residual stress formation. This chapter is divided into three sections - the first section is a literature review on residual stress formation during machining of ceramic materials. This section mainly addresses the causes for residual stress formation, modeling of subsurface damage formation, and the different methods used to quantify residual stress.

The second section deals with residual stress measurement and modeling for the case of machined sapphire. This section is further divided into 4 subsections. In the first subsection, the method used to quantify residual stress - Raman spectroscopy is introduced and details about the setup used are provided. In the next subsection, the results of residual stress measurements for different cutting directions on the 4 crystallographic planes of sapphire are discussed. Following this, the correlation between the material deformation and residual stress magnitude is presented. In the last subsection, an approach to measure the residual stress tensor post machining of sapphire is introduced.

In the third section of this chapter, residual stress measurements in 8YSZ are presented. In the case of 8YSZ, nanoindentation was used to measure residual stresses. The data analysis of was however carried out using two approaches. The first approach used the fracture toughness values for different cleavage systems in 8YSZ and the second approach relied on the variation in elastic and plastic energy during the indentation process. In this section, the measurements and analysis was carried out for different cutting directions on the (001) and (011) planes of 8YSZ.

3.1 Literature Review

Residual stresses are those stresses that remain in a material after all the applied loads are removed. The most common sources of residual stresses in machined components include plastic deformation, temperature gradients and phase transformations [74]. These changes can act as initial flaws for crack initiation and lead to failure of the component at premature loads or during subsequent processing [75, 76]. Since residual stresses can be detrimental to ceramic properties through facilitation of crack initiation processes, it is of critical importance to remove residual stresses after machining. Residual stresses in machined ceramics have been quantified through a variety of techniques such as X-ray diffraction, Raman spectroscopy, acoustic birefringence, hole-drilling strain-gauge method etc. [77, 78]. Considering the samples in the current research, nondestructive techniques such as Raman spectroscopy, nano-indentation, and X-ray diffraction are preferred due to the small regions in which the residual stresses need to be investigated and anisotropic nature of the ceramic sample.

The presence of residual stresses after scratch tests on sapphire was reported by Zhang et al. using Raman spectroscopy [79]. The authors observed that the residual stresses gradually changed from compressive to tensile as the scratching depth was increased. A further study with scratch tests showed that tensile residual stresses were responsible for lateral crack nucleation during the unloading phase [80]. This result is pertinent to UPM as this condition is experienced when the tool disengages from the workpiece. In the research by Lin et al., finite element simulations were used to determine the residual stresses during UPM of a NiP alloy. The authors reported that the magnitude of compressive residual stress increased with increase in cutting velocity [81].

Studies by Langan et al. on laser-assisted scratch tests on sapphire reported an anisotropy in the residual stress magnitude in terms of the cutting depth. During the tests without laser, tensile and compressive residual stresses were observed at different depths whereas only compressive residual stresses of different magnitudes were observed with laser. It was also observed that the residual stress changed from tensile to compressive as the scratch depth was increased [82]. In terms of the influence of crystal anisotropy on residual stress, Wermelinger et al. observed regions of compressive residual stress around a nano-indent on the C-plane of sapphire corre-

sponding to the alignment of R-planes. These regions of compressive stress were surrounded by a region of tensile stress in the out-of-plane direction [83].

In the area of conventional machining, many authors have developed models to predict residual stresses during various machining operations [84, 85]. However, no relevant literature could be found for ultra-precision machining of single crystal ceramics considering plastic deformation mechanisms activation or a crystal plasticity approach. Addressing this gap in literature could help improve our understanding of residual stress formation during machining.

From the preliminary experimental results presented in section 1.1 and literature review, it is clear that factors such as residual stresses and subsurface damage can initiate cracks at premature loads during UPM of single crystal ceramics. Further, from many studies on predicting deformation behavior of single crystal ceramics during UPM, the importance of understanding the activation of different deformation mechanisms and the related anisotropic characteristics was established [30, 52, 63].

3.2 Residual Stress Measurements in Sapphire

Based on the literature reviewed, Raman spectroscopy was chosen as the measurement technique due to the following factors:

- Residual stresses in sapphire have been studied by many researchers using this technique and literature to correlate the peak shift to residual stress magnitude is available [82, 83, 86, 87].
- As mentioned previously, high spatial resolution is necessary to take measurements from precise locations. In the confocal Raman microscope available at the university, measurements can be made using a laser spot size <4 μm
- As the plastically deformed layer is believed to extend down only a few microns from the machined surface, a technique where the material volume being probed does not extend beyond this plastically deformed region is necessary and Raman spectroscopy meets these requirements.
- A non-destructive technique where the sample is not exposed to radiation or heating for a long period of time is ideal in order not to change the residual stress state post machining.

By selecting the suitable measurement parameters, Raman spectroscopy can fulfill these requirements.

3.2.1 Raman Spectroscopy

The Residual stress magnitude in the machined sapphire samples were measured using confocal micro-Raman spectroscopy (LabRAM HR Evolution, Horiba Ltd., Japan). A typical Raman spectrum for sapphire is shown in Figure 3.1. In this figure, 4 different peaks at 378 cm^{-1}, 417 cm^{-1}, 432 cm^{-1}, and 573 cm^{-1} Raman wavenumbers are visible. These peaks are a result of distinct E_g and A_{1g} phonon vibrations in sapphire. It must be noted that by increasing the spectral window beyond 580 cm^{-1}, additional peaks will be visible but they have not been considered for this study. From these spectra, two important parameters are calculated by peak fitting - the peak position and the peak width. Variations in the peak position are used to calculate the magnitude of residual stress and the changes in the peak width are used to qualitatively estimate the trends in the subsurface damage.

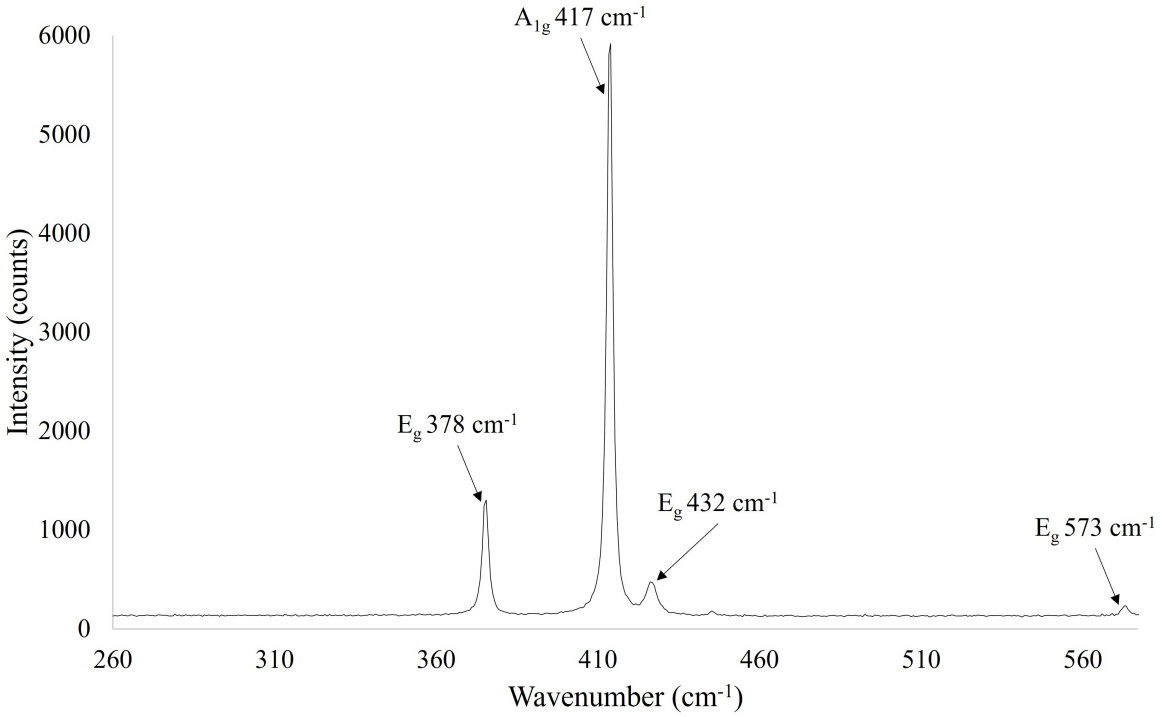

Figure 3.1: Raman spectrum of sapphire.

As will be discussed later, the peak position is very sensitive to the magnitude of stress in the

sample. Subsequently it was necessary to make the Raman measurements at the highest spectral resolution possible to ensure accurate estimation of the residual stress magnitude. The spectral resolution in Raman spectroscopy depends on a number of factors such as the laser wavelength, grating density, focal length, and confocal hole size. Among the laser options available - 405 nm, 532 nm, 633 nm, and 785 nm, the 633 nm laser was selected. As the laser wavelength is increases, the spectral resolution becomes higher but the spectral coverage decreases. The spectral coverage influences the time required for the measurement as larger spectral windows would require multiple exposures and data stitching. Keeping these factors in mind, the 633 nm laser was selected. Next, among the gratings available - 300 mm^{-1}, 600 mm^{-1}, and 1800 mm^{-1}, the 1800 mm^{-1} grating was selected as an increase in the grating density increases the spectral resolution. In terms of the optics and magnification, a 100x objective (0.9 NA) was selected from the available options (10x, 50x, 100x, and 50x far field) as it offered the best field of view in terms of the feature sizes on the machined sapphire samples. Lastly, to maximize the spectral resolution, a confocal hole size of 100μm was used. This parameter can be varied across a wide range and the spectral resolution gets better as the hole size is reduced. However, on reducing the hole size, the intensity of the signal diminishes and a longer exposure time would be required. This parameter was optimized to get a reasonable signal with a 10 - 15 s scan time.

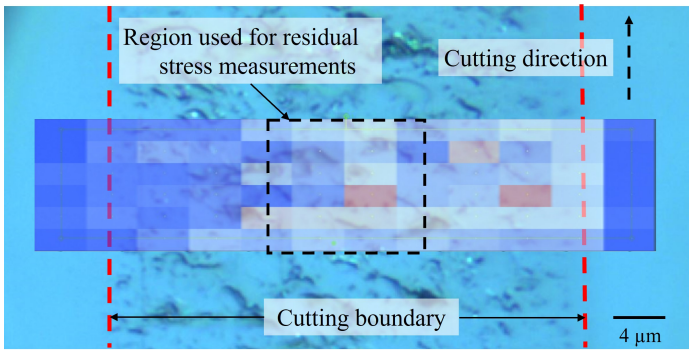

Figure 3.2: An example of Raman measurements taken from the brittle region of a cut.

Figure 3.2 shows an example of the Raman spectroscopy measurements carried out in this study. The image shows a mapping measurement in the brittle region of a cut where each colored box represents the actual peak position for the 417 cm^{-1} A_{1g} phonon peak. For each cutting direction, the peak position was determined by taking the average value from 24 points in the center of the cut. 2 measurements (10 s each) were made at each point to eliminate cosmic ray

spikes. The duration of 10 s for each measurement was selected to minimize annealing of the sample due to laser heating. The 24 points for measurement were arranged in a 6×4 grid, ≈12 μm wide and 9 μm high as shown in Figure 3.2.

The nature and magnitude of residual stress was determined by comparing the peak position in the machined regions with the peak position from a region of the sample free of machining. A peak shift to lower wavenumbers indicates tensile residual stress whereas a peak shift to higher wavenumbers indicates compressive residual stress. The magnitude of residual stress, presented as an equivalent magnitude was determined through data extrapolated from a diamond anvil test resulting in a correlation of 2.2 cm^{-1}/GPa of peak shift [86]. At this stage of the analysis, only the position of the 417 cm^{-1} A_1g phonon peak was considered as it has the highest signal intensity. These measurements were repeated for the ductile, ductile-brittle transition, and brittle regions (see Figure 2.8 for each of the seven cutting directions on the 4 crystallographic planes of sapphire investigated in this study. The measurement parameters are summarized in Table 3.1

Table 3.1: Summary of parameters used in Raman spectroscopic measurements.

Parameter	**Value**
Instrument	Horiba LabRAM HR Evolution
Laser Wavelength	633 nm
Microscope Objective	100x (0.9 NA)
Confocal Hole Size	100 μm
Grating Density	1800 mm^{-1}
Spectral Window	260 cm^{-1} - 577 cm^{-1} (centered about 417 cm^{-1})
Laser Polarization	None
Acquisition Time	10 s per spot
No. of Acquisitions per Spot	2
Binning	1
Neutral Density Filter	100 %
Stage Movement Step Size	4 μm in the horizontal direction and 2 μm in the lateral direction (see Figure 3.2)

3.2.2 Results and Discussion - Residual Stress Magnitude

This work has been published in the Annals of the CIRP and was presented at the CIRP General Assembly in 2022 [24].

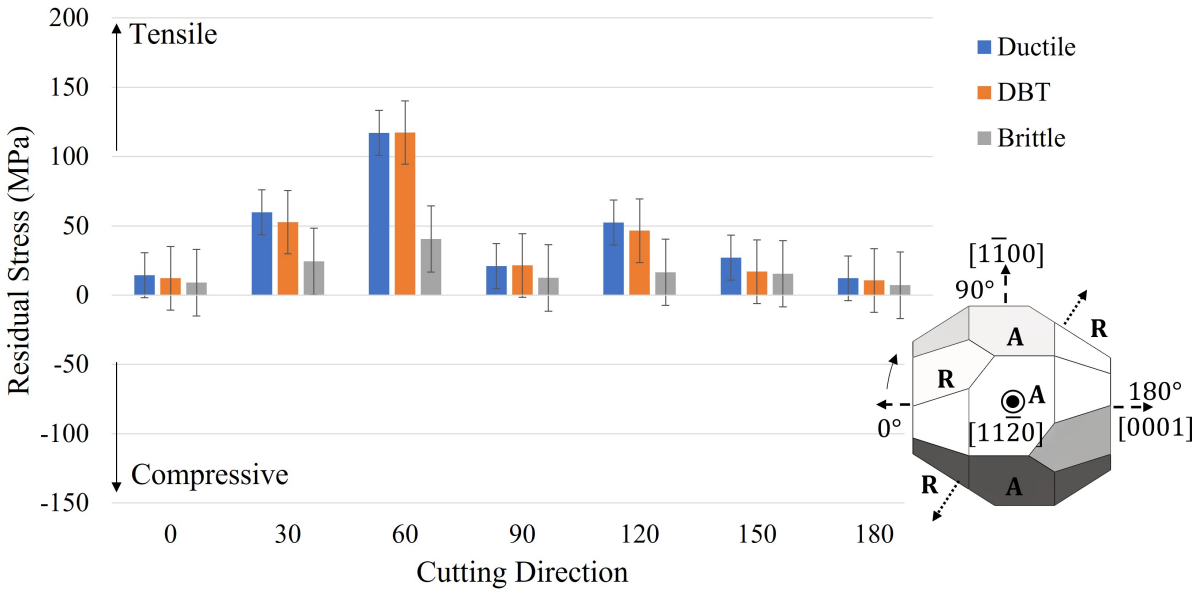

Figure 3.3: Variation in residual stress magnitude with cutting direction and depth of cut on A-plane of sapphire.

Figure 3.3 shows the magnitude of equivalent residual stress in the ductile, ductile-brittle transition and brittle regions for various cutting directions on the A-plane of sapphire. The residual stresses observed were tensile for all the cutting directions and ranged from 7 MPa in the brittle region of the 180° cutting direction to 117 MPa in the ductile and ductile brittle transition regions of the 60° cutting direction. In all the cases, it was observed that the magnitude of residual stress in the brittle region was smaller than that of the ductile or ductile-brittle transition regions. This could likely be due to stress relief provided by crack initiation.

The magnitude of residual stress for different cutting directions on the C-plane of sapphire is shown in Figure 3.4. Unlike the A-plane, the residual stress magnitude across all the cutting directions and depths of cut remained relatively low (<10 MPa) and almost negligible on the C-plane of sapphire. A likely reason for this interesting observation is investigated further in section 3.2.3.

The residual stress magnitude for different cutting directions and at different depths of cut

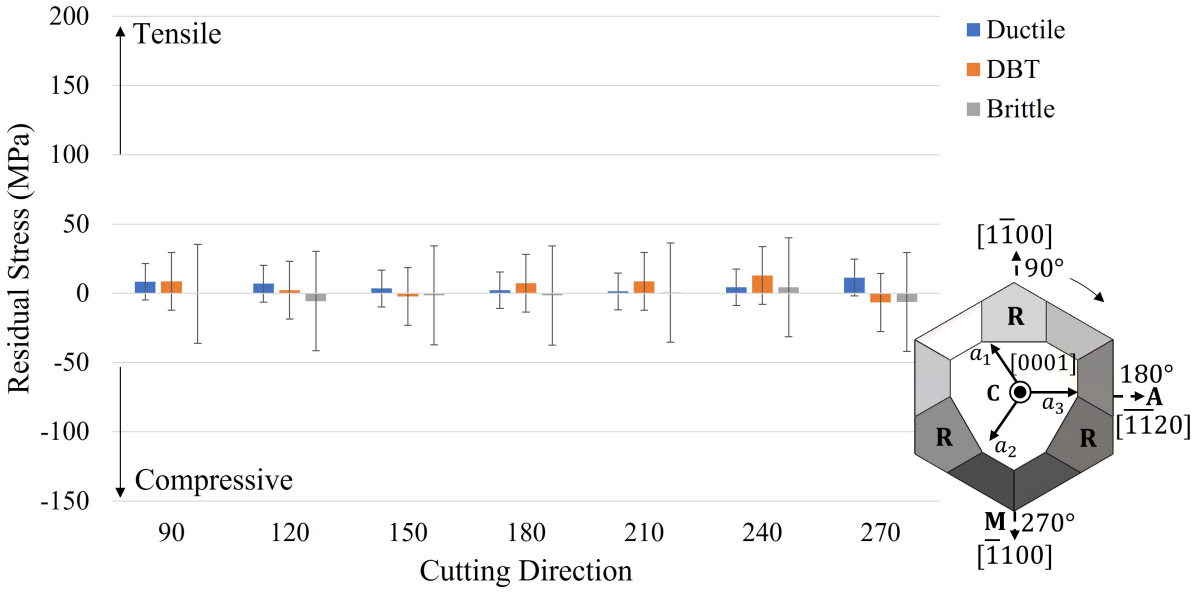

Figure 3.4: Variation in residual stress magnitude with cutting direction and depth of cut on C-plane of sapphire [24].

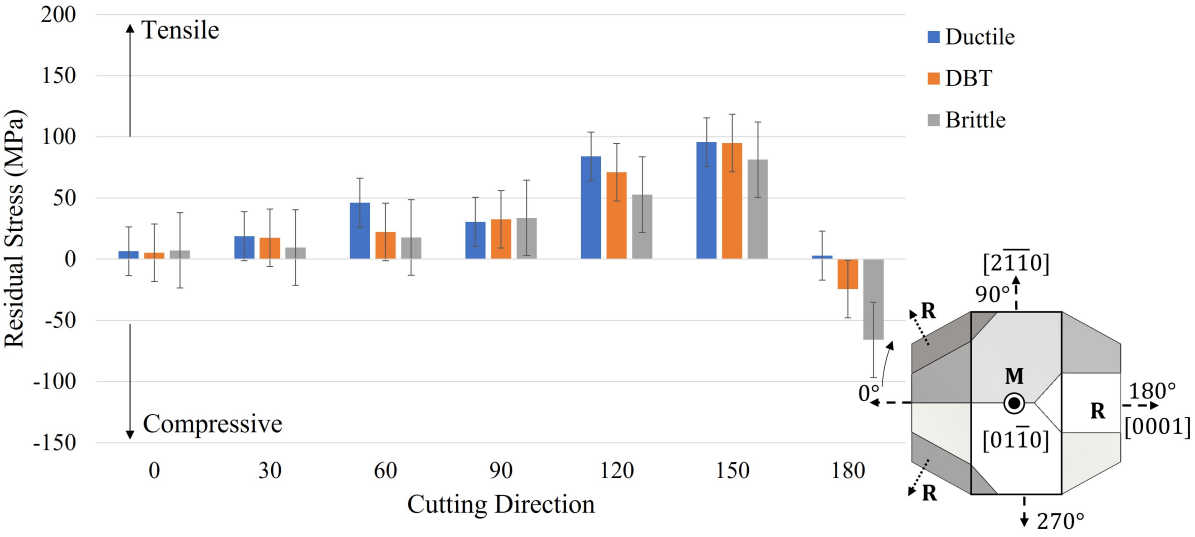

Figure 3.5: Variation in residual stress magnitude with cutting direction and depth of cut on M-plane of sapphire.

on the M-plane of sapphire is shown in Figure 3.5. The residual stresses were tensile for most of the cutting directions investigated except for the 180° case where compressive residual stresses were observed in the ductile brittle transition and brittle regions. The magnitude of residual stress ranged from 7 MPa in the case of the brittle region of the 0° cutting direction to 95 MPa in the case of the ductile and ductile-brittle transition regions of the 150° cutting direction. The maximum compressive residual stress measured was -65 MPa in the brittle region of the 180° cutting direction. At this moment the reason for formation of compressive residual stress is not known and needs to be studied further. In all the other cutting directions, like the case of A-plane, the magnitude of residual stress in the brittle and ductile-brittle transition regions were lower than that of the ductile region.

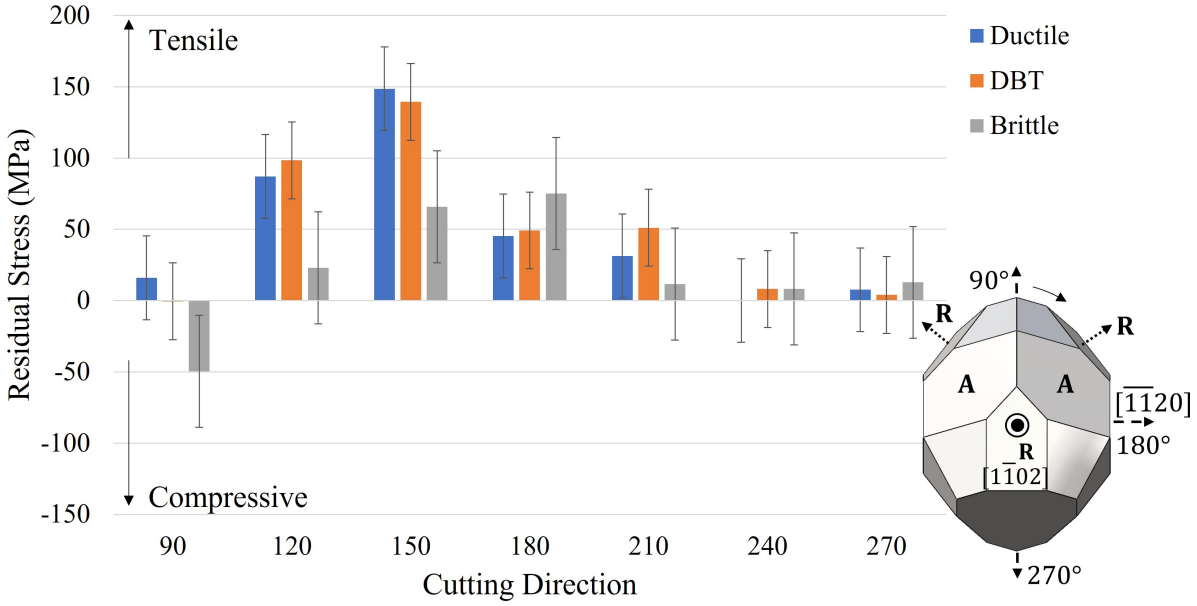

Figure 3.6: Variation in residual stress magnitude with cutting direction and depth of cut on R-plane of sapphire [24].

Figure 3.6 shows the magnitude of residual stress for different cutting directions on the R-plane of sapphire. Like the M-plane, the residual stresses were tensile in most of the cases except for the brittle region of the 90° cutting direction which exhibited an average residual stress of -65 MPa. The magnitude of residual stress varied from 0 to 148 MPa in those directions that exhibited tensile residual stress magnitudes. In most of the cutting directions, the residual stress magnitude decreased in the ducitle-brittle transition and brittle regions due to stress

relief provided by crack initiation except for the case of the 180° cutting direction. A likely reason for this could be due to the sparse nature of cracks in this cutting direction and high CDC value (see Figure 3.7). As a result of this type of crack morphology, it is likely that the residual stresses accumulate with plastic deformation as the depth of cut is increased and the cracks relieve the stresses only at few localized regions beyond the CDC.

From the analysis of the residual stress magnitude for different cutting directions and depths of cut on the A-, C-, M-, and R- planes of sapphire, it was observed that the residual stresses were tensile in nature for most cutting directions and the magnitude varied from -65 MPa to 150 MPa. The uncertainty in the residual stress measurements ranged from $\approx$ 20 MPa in the ductile and ductile-brittle transition regions to $\approx$ 30 MPa in the brittle region. Further, it was also observed that the crack morphology could potentially influence the residual stress magnitude and needs to be accounted for. Based on these results, the first hypothesis was verified that the residual stresses resulting from UPM of ceramics is anisotropic in nature, depending on the cutting direction and depth of cut.

3.2.3 Results and Discussion - Analysis of Plastic Deformation Mode and Correlation to Residual Stress

This section deals with verifying the second hypothesis by investigating whether a correlation between plastic deformation mechanisms and residual stress magnitude exists. Using the approach detailed in section 1.2, the likelihood of activation of different plastic deformation mechanisms on the R- and C-planes of sapphire were calculated corresponding to the depth of cut at which the Raman measurements were made.

The variation in plastic deformation parameter with cutting direction for the three depths of cut corresponding to the Raman measurements on R-plane are shown in Figure 3.7(a). The angle made by the dominant plastic deformation mechanisms with the machined surface is shown in Figure 3.7 (b). In the ductile and DBT regions for the 150°, 180° and, 210° cutting directions, rhombohedral twinning on an adjacent R-plane (R2 TW) was the dominant mechanism. Since this mechanism makes an angle of $\approx$ 42° with the machined surface, the plastic deformation is thought to extend deeper into the subsurface which explains the large value of residual stress magnitude.

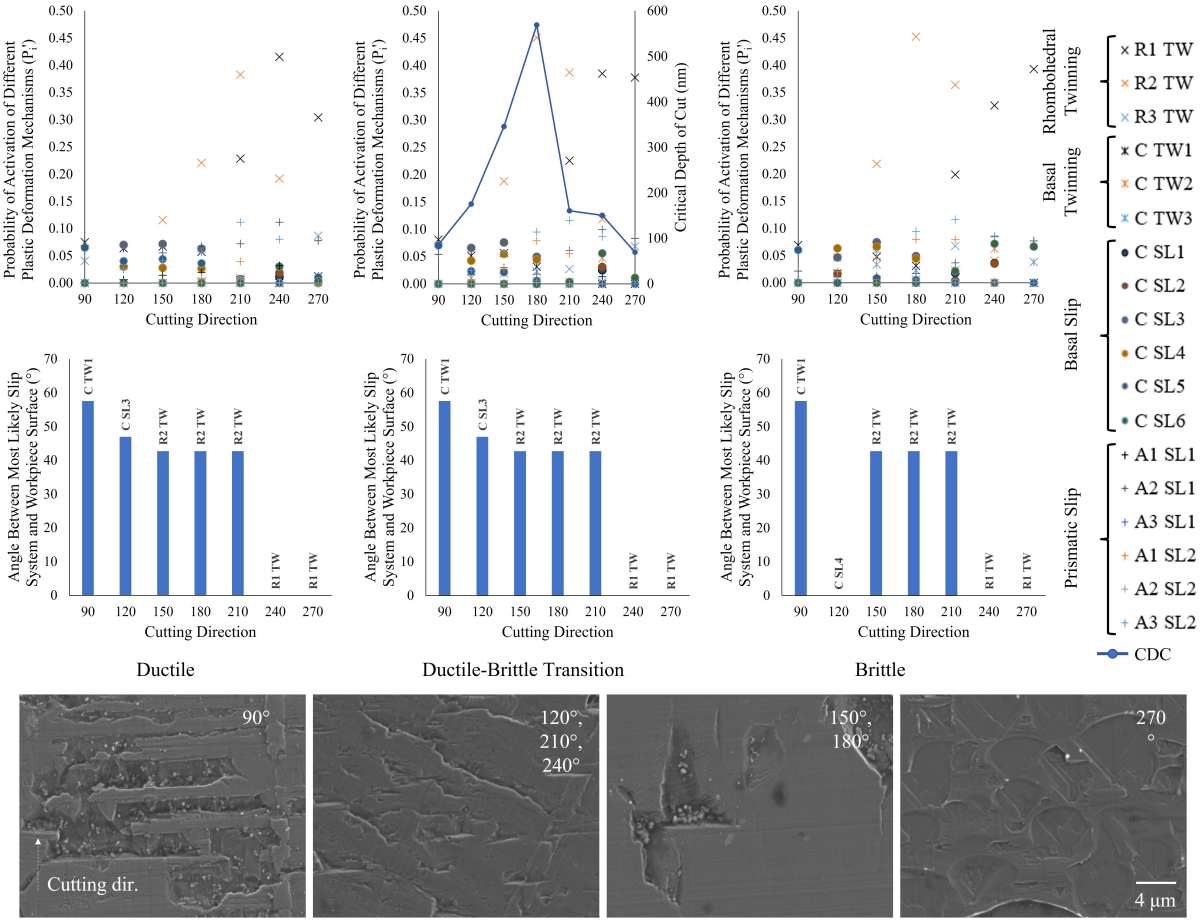

Figure 3.7: (a) Likelihood of activation of different plastic deformation mechanisms with varying cutting direction and depth of cut; (b) Angle made by the dominant plastic deformation mechanism with the substrate surface; (c) Crack morphology for different cutting directions on R-plane of sapphire [24].

In the case of 210° cutting direction the most dominant mechanism was R2 TW and the second most dominant mechanism was rhombohedral twinning on the same R-plane as the cutting (R1 TW) which might lead to dislocation entanglement, thus reducing the amount of plastic deformation deeper into the workpiece and consequently the residual stress. In case of the 240° and 270° cutting directions, rhombohedral twinning on the same plane as the cutting was dominant which results in deformation parallel to the surface and at a shallow depth which is removed by chip formation leading to lower magnitude of residual stress.

In the 90° cutting direction, although the dominant mechanism was basal twinning, the CDC for this cutting direction is the smallest ($\approx$ 90 nm). Hence, not much residual stress is thought to accumulate in the ductile region. In the 120° cutting direction, the dominant plastic

deformation was basal slip which forms an angle of $\approx 47^\circ$ with the machined surface resulting in plastic deformation that extends deeper into the subsurface and higher magnitude of residual stress.

Looking at the brittle regions of the different cutting directions (Figure 3.7 (c)), the fractures in the case of 180° and 150° cutting directions were sparse with large regions of ductile machining in between cracks. As a result, the decrease in residual stress magnitude from DBT to brittle region was not observed in 180° case and a small amount was observed for 150° cutting direction. In the case of 120°, 210°, and 240° cutting directions, prismatic and rhombohedral fractures covered the brittle region and were deep [63]. This explains the sharp reduction in residual stress magnitude in these directions due to stress relief provided by crack initiation.

In case of the 270° cutting direction, shallow prismatic fractures were observed. As the residual stress magnitude in this direction was already small, not much change was observed. In the 90° cutting direction, basal and prismatic fractures were observed in a banded fashion, likely caused by alternative pile up of material through plastic deformation and fractures relieving the stresses partially [30]. The pile-up could be a likely reason for compressive residual stresses in this direction.

The variation in plastic deformation parameter with cutting direction for the three depths of cut corresponding to the Raman measurements on C-plane of sapphire are shown in Figure 3.8 (a). Unlike the R-plane, there wasn't much anisotropy in the dominant plastic deformation mechanisms. In the 120°, 150°, 240°, and 270° cutting directions, the dominant mechanism across depths of cut was basal slip or basal twinning which causes deformation parallel to the workpiece surface (0° in Figure 3.7 (b)) and forms a shallow layer of plastic deformation that is easily removed by chip formation or fracture at larger depths of cut.

Considering the 180° cutting direction, basal slip was the dominant mechanism at low depths of cut but changed to rhombohedral twinning as the depth of cut was increased. However, the probabilities of activation of all the mechanisms remain low and there could be dislocation entanglement leading to lower depth of plastic deformation. The case of 90° and 210° cutting directions was similar to that of the 180° cutting direction with a slight difference being rhombohedral twinning was the dominant mechanism even at low depths. However, low values of residual stress magnitude are likely due to dislocation entanglement resulting in a shallow plas-

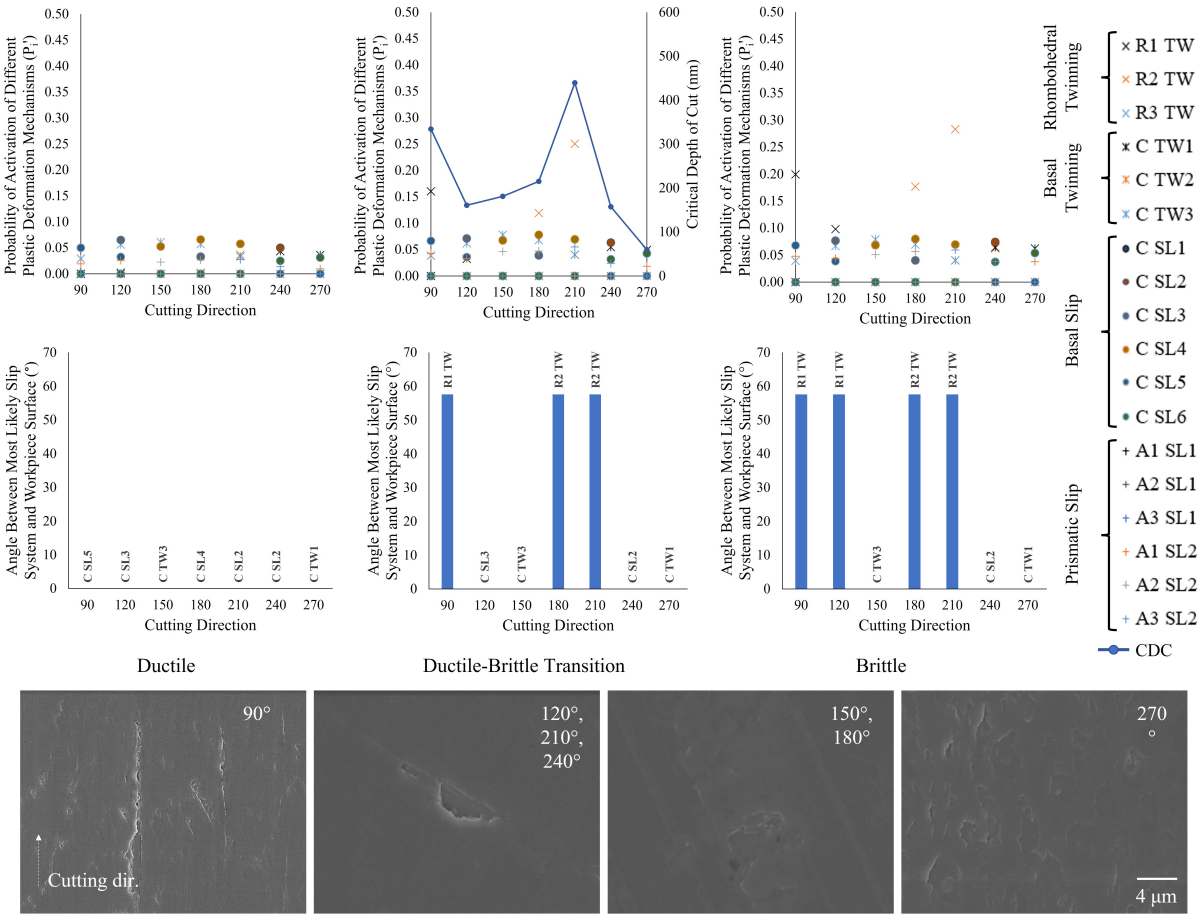

Figure 3.8: (a) Likelihood of activation of different plastic deformation mechanisms with varying cutting direction and depth of cut; (b) Angle made by the dominant plastic deformation mechanism with the substrate surface; (c) Crack morphology for different cutting directions on C-plane of sapphire [24].

tic deformation region. Considering the fracture mechanisms on the C-plane (Figure 3.8 (c)), prismatic fractures dominate across different cutting directions [88]. Unlike the R-plane, cracks were not highly concentrated, as seen in certain directions (270° of the R-plane). These shallow and spaced-out fractures thus relieve the small magnitude of residual stresses and do not cause much of a change to the residual stress state.

3.2.4 Using Raman Spectroscopy to Measure the Residual Stress Tensor

For many decades, researchers have understood the importance of the stress field at the tool-workpiece interface and proposed many theories to predict the outcome of the machining process [89, 90]. Extending this to the case of UPM, additional factors such as the tool edge radius,

material grain size, and crystal structure need to be taken into account [16]. In this regard, due to the additional factors influencing the deformation behavior as well as the difficulties in measuring stress-fields at micro- and nanometer scales, not much progress has been made in this regard which have led to incomplete model development in the field of deformation prediction during UPM.

In the previous section, Raman spectroscopy can be used to determine the average magnitude of stress in sapphire. However, given the unique crystallographic properties of sapphire, it has been shown that the residual stress tensor can be obtained from Raman measurements. This section follows the methodology introduced by Zhu and Pezzotti and is used to calculate the plane strain residual stress tensor. This work was limited to the measurement of only the plane strain tensor as a large enough spectral window was not selected during the initial data collection and the peak positions of only 4 phonon peaks were captured. The full stress tensor analysis requires information from 6 peaks and is proposed for future work. The detailed equations and explanation for full residual stress tensor calculation can be found in [87].

Further, in the case of sapphire, it has been observed that the intensity of different peaks observed in the Raman spectrum is dependent on the crystallographic orientation of the sample in the confocal Raman microscope [91]. As a result, in certain directions, one or more of the weaker peaks would not be visible to obtain peak position information. Under this constraint, it was observed that this effect of crystallography was least observed in the case of the R-plane and peak information from at least 3 peaks were observed for all the cutting directions and depths of cut and subsequently, the analysis was performed only on the R-plane of sapphire. The stress tensor calculation methodology is explained in the following paragraphs.

The analysis starts based on the fundamental relationship between Raman peak shift ($\Delta\nu$) and the stress tensor (σ_{ij}),

$$\Delta\nu = \Pi_{ij}\sigma_{ij} = \begin{vmatrix} \Pi_{11} & \Pi_{12} & \Pi_{13} \\ \Pi_{21} & \Pi_{22} & \Pi_{23} \\ \Pi_{31} & \Pi_{32} & \Pi_{33} \end{vmatrix} \begin{vmatrix} \sigma_{xx} & \sigma_{xy} & \sigma_{xz} \\ \sigma_{yx} & \sigma_{yy} & \sigma_{yz} \\ \sigma_{zx} & \sigma_{zy} & \sigma_{zz} \end{vmatrix} \tag{3.1}$$

where Π_{ij} are the piezospectroscopic coefficients of the material. Due to the symmetry of the sapphire crystal, the piezospectroscopic tensor becomes diagonalized [87]. The piezospectroscoic

coefficients of sapphire are listed in Table 3.2.

Table 3.2: Piezospectroscopic coefficients of sapphire [87].

Peak Position	Π_a **(cm^{-1}/GPa)**	Π_b **(cm^{-1}/GPa)**	Π_c **(cm^{-1}/GPa)**
378 cm^{-1} (E_g)	-0.486 ± 0.03	-0.286 ± 0.02	-0.352 ± 0.04
417 cm^{-1} (A_{1g})	-0.221 ± 0.03	-0.414 ± 0.02	-1.606 ± 0.04
432 cm^{-1} (E_g)	-0.684 ± 0.05	-0.565 ± 0.02	-0.949 ± 0.03

Accounting for the orientation of the crystal in the lab frame,

$$\Delta\nu = \Pi_{ij}\sigma_{ij} = \begin{vmatrix} \Pi_a^{(n)} & 0 & 0 \\ 0 & \Pi_b^{(n)} & 0 \\ 0 & 0 & \Pi_c^{(n)} \end{vmatrix} \Phi_{xyz} \begin{vmatrix} \sigma_{xx} & \sigma_{xy} & \sigma_{xz} \\ \sigma_{yx} & \sigma_{yy} & \sigma_{yz} \\ \sigma_{zx} & \sigma_{zy} & \sigma_{zz} \end{vmatrix} \tilde{\Phi}_{xyz} \tag{3.2}$$

where Φ_{xyz} is the rotation matrix and $\tilde{\Phi}_{xyz}$ is the transpose of the rotation matrix defined in terms of the Euler angles (θ, ϕ, ψ) and is given by:

$$\Phi_{xyz} = \begin{vmatrix} \cos\theta\cos\phi\cos\psi - \sin\phi\sin\psi & \cos\theta\sin\phi\cos\psi + \cos\phi\sin\psi & -\sin\theta\cos\psi \\ -\sin\phi\cos\psi - \cos\theta\cos\phi\sin\psi & \cos\phi\cos\psi - \cos\theta\sin\phi\sin\psi & \sin\theta\sin\psi \\ \sin\theta\cos\phi & \sin\theta\sin\phi & 0 \end{vmatrix} \tag{3.3}$$

with $0 \leq \theta \leq \pi$, $0 \leq \phi \leq 2\pi$, and $0 \leq \psi \leq 2\pi$. Expanding equations 3.2 and 3.3 and simplifying for the assumption of plane strain condition as the deformation is concentrated very close to the surface and the residual stress must equilibrate over any section,

$$\begin{vmatrix} \sigma_{xx} \\ \sigma_{xy} \\ \sigma_{yy} \end{vmatrix} = \begin{vmatrix} A_{11} & A_{12} & A_{13} \\ A_{21} & A_{22} & A_{23} \\ A_{31} & A_{32} & A_{33} \end{vmatrix}^{-1} \begin{vmatrix} \Delta\nu_1 \\ \Delta\nu_2 \\ \Delta\nu_3 \end{vmatrix} \tag{3.4}$$

where A_{ij} are coefficients containing terms from Π_{ij} and Φ_{ij} and can be expanded as follows:

$$A_{n1} = \Pi_a^{(n)}(\cos\theta\cos\phi\cos\psi - \sin\psi\sin\phi)^2 + \Pi_b^{(n)}(\sin\phi\cos\psi + \sin\psi\cos\theta\cos\phi)^2 + \Pi_c^{(n)}(\sin^2\theta\cos^2\phi) \tag{3.5}$$

$$A_{n2} = \Pi_a^{(n)}(-\sin 2\phi\sin^2\psi + \cos^2\theta\sin 2\phi\cos^2\psi + \cos\theta\cos 2\phi\sin 2\psi) + \Pi_b^{(n)}(-\sin 2\phi\cos^2\psi + \cos^2\theta\sin 2\phi\sin^2\psi - \cos\theta\cos 2\phi\sin 2\psi) + \Pi_c^{(n)}(\cos^2\theta\sin 2\phi) \tag{3.6}$$

$$A_{n3} = \Pi_a^{(n)}(\cos\theta\sin\phi\cos\psi + \sin\psi\cos\phi)^2 + \Pi_b^{(n)}(\sin\phi\cos\psi + \sin\psi\cos\theta\cos\phi)^2 + \Pi_c^{(n)}(\sin^2\theta\sin^2\phi) \tag{3.7}$$

Using the equations 3.5 - 3.7 and solving equation 3.4, the plane strain residual stress tensor components were calculated for different cutting directions and depths of cut on the R-plane of sapphire.

Figure 3.9 shows the variation in residual stress σ_{xx} with respect to the different cutting directions and depths of cut. It was observed that the residual stress magnitude varied between -190 MPa and 312 MPa. The residual stresses in the x direction (along the direction of cutting) were compressive for the 90°, 120°, and 270° cutting directions and tensile in the other directions. 150° cutting direction showed the maximum magnitude of tensile residual stress, similar to the average residual stress magnitude presented earlier (Figure 3.6). Further, it was observed that the stress magnitude was lower in the brittle and ductile-brittle transition regions as compared to the ductile region of the cut.

Figure 3.10 shows the variation in residual shear stress τ_{xy} with respect to the different cutting directions and depths of cut. Compared to the normal stress, the magnitude of shear residual stress was almost an order of magnitude smaller. The magnitude of τ_{xy} varied between -21 and 13 MPa. In this case, the ductile and ductile-brittle transition regions for 90° cutting direction, 120°, and 240° orientations exhibited compressive residual stress whereas the other cutting directions and depths were shown to have a tensile residual stress. The 120° cutting direction showed the maximum magnitude of compressive residual stress and the 90° cutting direction showed the maximum magnitude of tensile residual stress.

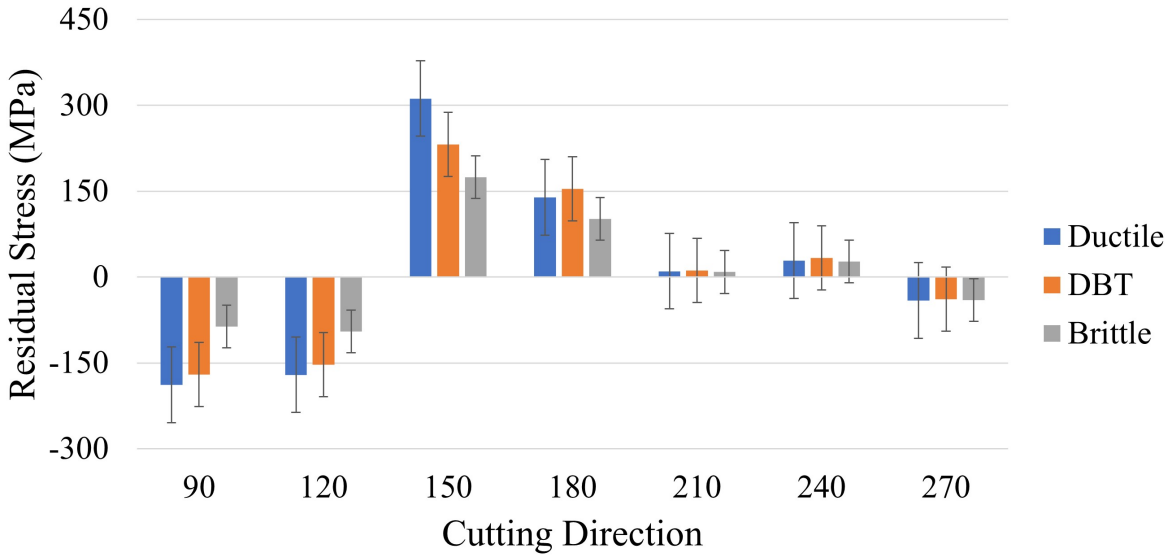

Figure 3.9: Variation in residual stress σ_{xx} with cutting direction and depth of cut on R-plane of sapphire.

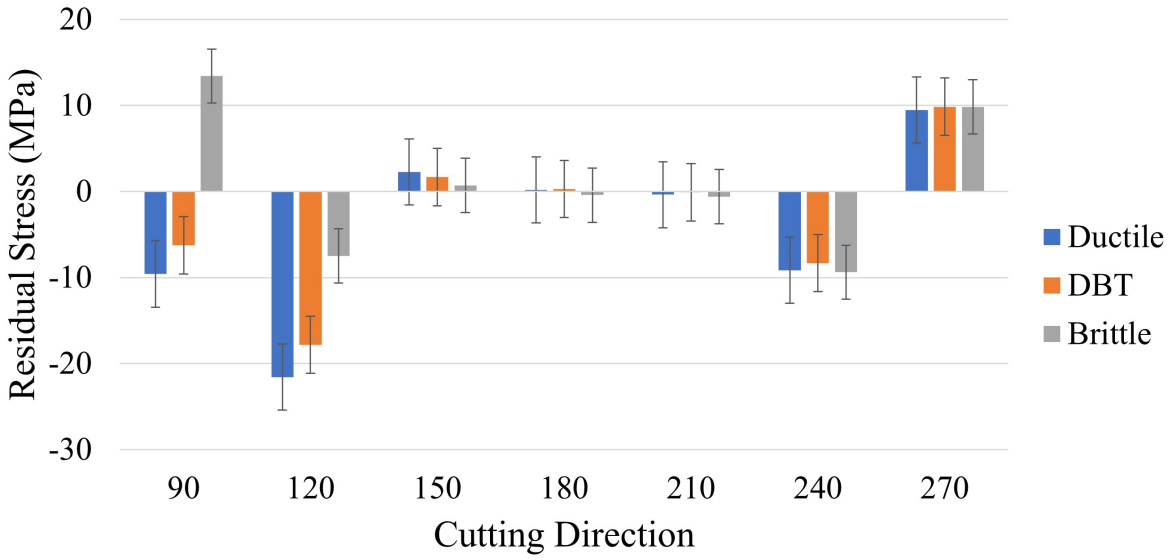

Figure 3.10: Variation in residual stress τ_{xy} with cutting direction and depth of cut on R-plane of sapphire.

The values of normal residual stress in the y direction (perpendicular to the cutting direction) are shown in Figure 3.11. It was observed that the magnitude of residual stress varied between -90 and 79 MPa which is slightly lower than the stresses observed in the x direction. It was further observed that the residual stresses were compressive in the 90°(brittle region), 150°, 180°, and 270° cutting directions and tensile in all other cases. Once again the 150° cutting direction showed the maximum magnitude of residual stress, but compressive in nature whereas the 120° cutting direction showed the maximum magnitude of tensile residual stress.

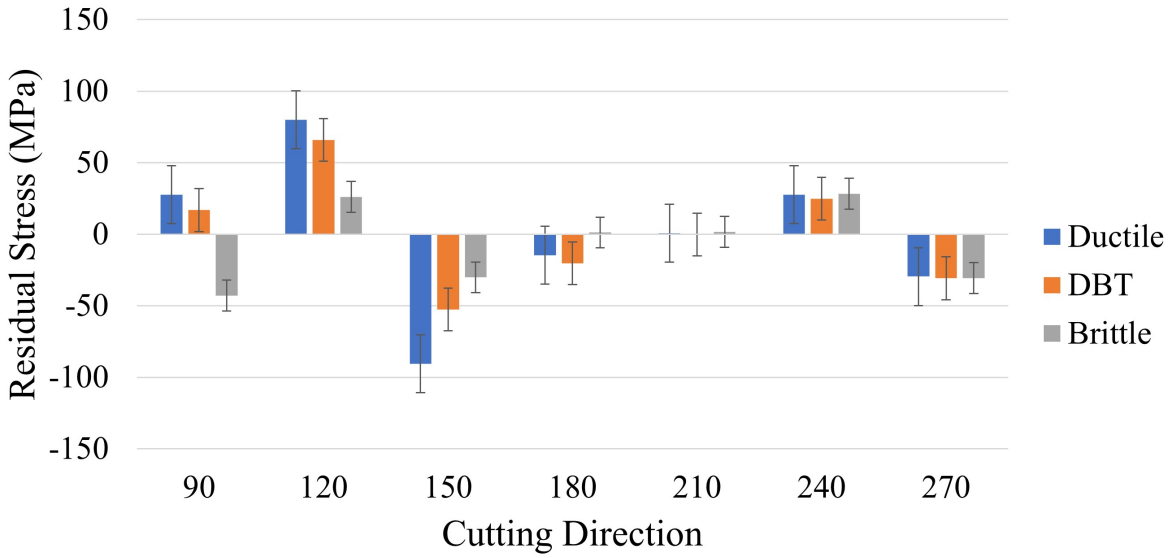

Figure 3.11: Variation in residual stress σ_{yy} with cutting direction and depth of cut on R-plane of sapphire.

Upon completion of the analysis of residual stress components for different cutting directions on the R-plane of sapphire, the first principal stress was calculated to get an idea of the maximum normal residual stress in the material as shown in Figure 3.12. It was observed that the principal stress varied between -39 and 312 MPa. The trends observed were very similar to the measurements obtained previously using only the variation in the 417 cm^{-1} peak data (Figure 3.6). It was observed that the 150° cutting direction exhibited the maximum magnitude of tensile stress followed by the 180° and 120° cutting directions. Like the previous results, the residual stress magnitude in the 90°, 210°, 240°, and 270° cutting directions were small or negligible. Like the previous results, compressive residual stress was observed in the case of the brittle region for the 90° cutting direction.

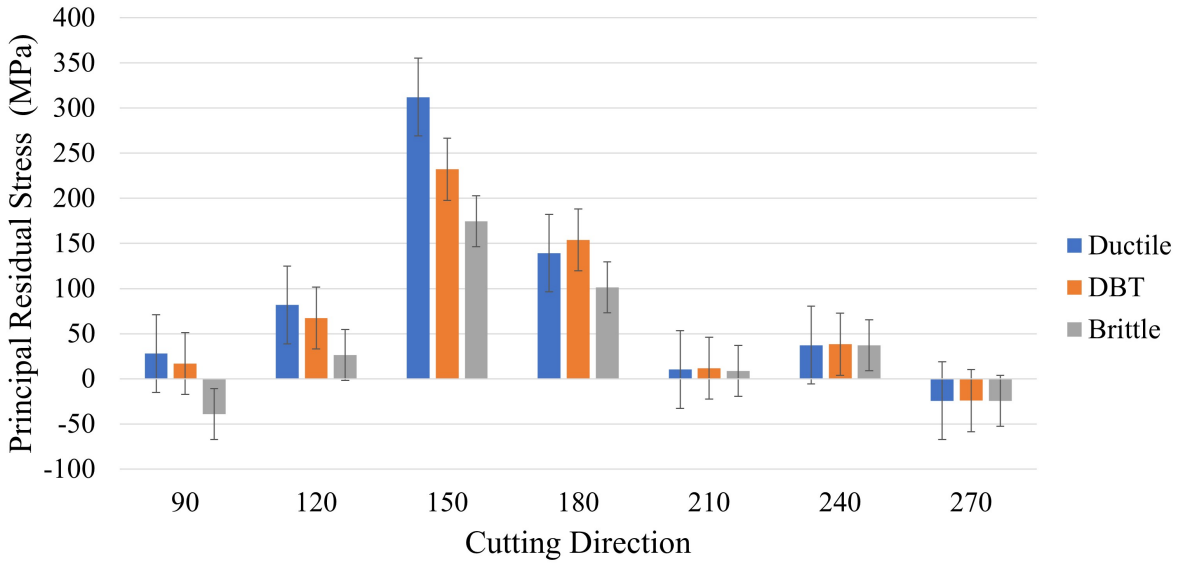

Figure 3.12: Variation in first principal residual stress with cutting direction and depth of cut on R-plane of sapphire.

From these results, it was shown that Raman spectroscopy can be a powerful tool in analyzing the residual stresses in machined ceramics like sapphire and with proper data collection, it is possible to calculate the stress tensor in the areas of interest. Further, a strong correlation between the deformation mechanisms and magnitude of residual stress was shown which helps us look towards improving the machining throughput during UPM of single crystal ceramics.

3.3 Residual Stress Measurements in 8YSZ

Initially, it was planned to use Raman spectroscopy to measure the residual stresses in 8YSZ following many authors in literature [92,93]. However, the Raman and photoluminescence spectrum of the material was too weak (considering scan times of < 15 s) to be able to determine the residual stresses accurately. Consequently, it was decided to use nanoindentation instead, as it provides excellent control over selecting the measurement region and by selecting the correct loading/unloading parameters, the region close to the surface can be probed. One of the main challenges with nanoindentation is that the theory used in analysis is still in the nascent stages and careful thought needs to be given while choosing a model to estimate residual stress magnitude.

Some of the common models proposed to determine residual stresses in brittle materials

using a sharp indenter include the Suresh and Lee models [94]. The Suresh model and Lee model I consider differences in hardness between a stressed and unstressed sample to determine the residual stress [95, 96]. However, the drawback of these models is that it is applicable only to an equi-biaxial stress state which is unlikely in the case of machined ceramics. Subsequently, the Lee model was developed further to account for biaxial stresses but a special apparatus was required to apply different amounts of load in orthogonal directions to determine the calibration constants used in the model [97]. Hence this approach was not pursued further. Another noteworthy approach was the method followed by Zhang et al. to determine residual stresses in zirconia-porcelin dental crowns where the authors used the differences in hardness between a stressed and unstressed region of the sample to determine the residual stress magnitude [98]. Although simple to implement, it was not used since this model assumes isotropic material properties such as the Young's modulus.

Particularly for brittle materials such as ceramics, an interesting approach to determine residual stress involves changes in the radial crack length and fracture toughness. In this method, it is assumed that the residual stress can affect the fracture toughness of the material - increases if the residual stress is compressive and decreases if the residual stress is negative [99]. Consequently, the length of radial crack would shorten or lengthen respectively. Following this approach, Dahmani et al. determined the residual stresses around a laser induced crack in fused quartz [100]. The authors started with an assumption that the at the early stages of crack initiation, the final depth of indentation and radial crack length are of the same order of magnitude and can be equated. Further, accounting for the residual stress field using contact mechanics theory, an expression for the fracture toughness and residual stress was derived. The present research uses this model to determine the residual stresses in machined 8YSZ.

3.3.1 Nanoindentation and Analysis

Nanoindentation was performed along the center of the machined cuts using a triboindenter (Hysitron TI 950, Bruker Corporation, USA) with a diamond Berkovich indenter. The indents were performed from the start of the cut to 500 nm depth of cut in increments of 10 μm lateral spacing. Indentation was performed in the load-control mode with a peak load of 50 mN and loading/unloading rate of 1.25 mN/s with a 2 s hold time between the loading and unloading

segments. A schematic of the indentation is shown in Figure 3.13.

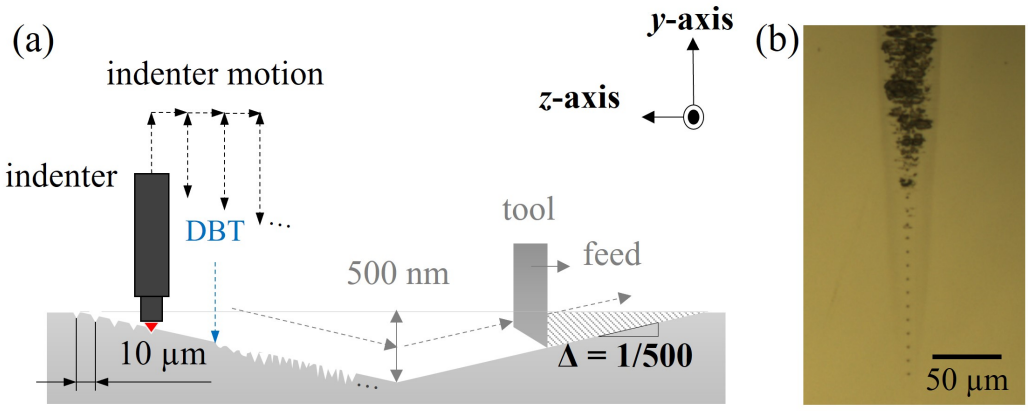

Figure 3.13: (a) Schematic of nanoindentation experiments; (b) Optical image of nano-indents on machined cut.

The indentation was performed on 2 cuts for each machining direction for the purpose of repeatability. As a strain-free reference, 16 indents were performed in the polished region of the samples prior to indentation on the machined cuts for each direction. These reference indents were at least 2 mm away from the machined cuts to prevent any influence from the plastic deformation in the machined regions. Analysis of hardness and Young's modulus was carried out based on the Oliver-Pharr method [101] as follows:

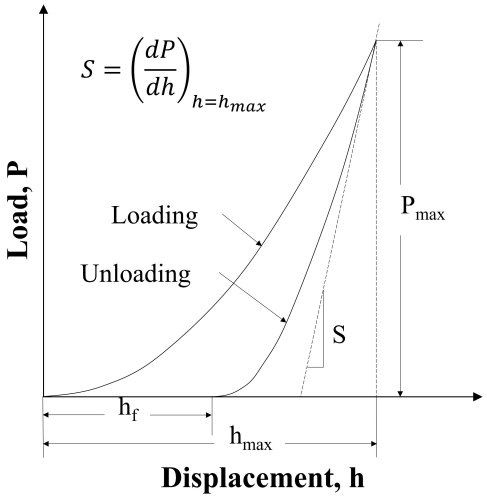

Figure 3.14: An example load-displacement curve obtained from nanoindentation [100, 101].

$$h_c = h_{max} - \epsilon \frac{P_{max}}{S} \tag{3.8}$$

where h_c is the contact depth, h_{max} is the maximum indentation depth, $\epsilon = 0.75$ is a constant which depends on the geometry of the indenter [102], P_{max} is the maximum indentation load, and S is the slope of the elastic portion of the unloading curve.

$$A_{pml} = f(h_c) = 24.56(h_c)^2 + C_1(h_c)^1 + C_2(h_c)^{1/2} + C_3(h_c)^{1/4} + ... \tag{3.9}$$

where A_{pml} is the projected contact area at P_{max} and C_1, C_2, C_3, etc. are polynomial fitting constants obtained from calibration experiments on a fused quartz sample. The hardness, H and reduced modulus, E_r are then determined using the following equations

$$H = \frac{P_{max}}{A_{pml}} \tag{3.10}$$

$$E_r = \frac{S}{2B}\sqrt{\frac{\pi}{A_{pml}}} \tag{3.11}$$

where $B = 0.97$ is a geometric factor which depends on the indenter geometry [102, 103]. The Young's modulus of the sample can then be calculated using

$$\frac{1}{E_r} = \frac{1-\nu^2}{E} + \frac{1-{\nu_i}^2}{E_i} \tag{3.12}$$

where E is the Young's modulus of the sample, $\nu = 0.25$ is the Poisson's ratio of the sample [104], $E_i = 1140$ GPa is the Young's modulus of the indenter, and $\nu_i = 0.07$ is the Poisson's ratio of the indenter.

Based on the literature discussed in section 3.3, the model proposed by Dahmani et al. was used to determine the residual stress magnitude at each indent using the following equation [100]:

$$\sigma_r = \frac{K_c}{(\pi h_{f^*})^{1/2}}\left[1 - \left(\frac{E_*}{E_0}\frac{H_0}{H_*}\right)^{1/2}\left(\frac{h_{0f}}{h_{f^*}}\right)^{3/2}\right] \tag{3.13}$$

where K_c is the fracture toughness of the material (1.90 MPa.m$^{1/2}$ for radial cracks propagating along $\langle 100 \rangle$ and 1.50 MPa.m$^{1/2}$ for radial cracks propagating along $\langle 011 \rangle$ [60]), E_*, H_*, and h_{f^*} are the Young's modulus, hardness, and final indenter displacement of the machined region respectively, and E_0, H_0, and h_{0f} are the Young's modulus, hardness, and final indenter displacement from the strain-free reference region of the sample, respectively.

3.3.2 Results and Discussion - Residual Stress Magnitude

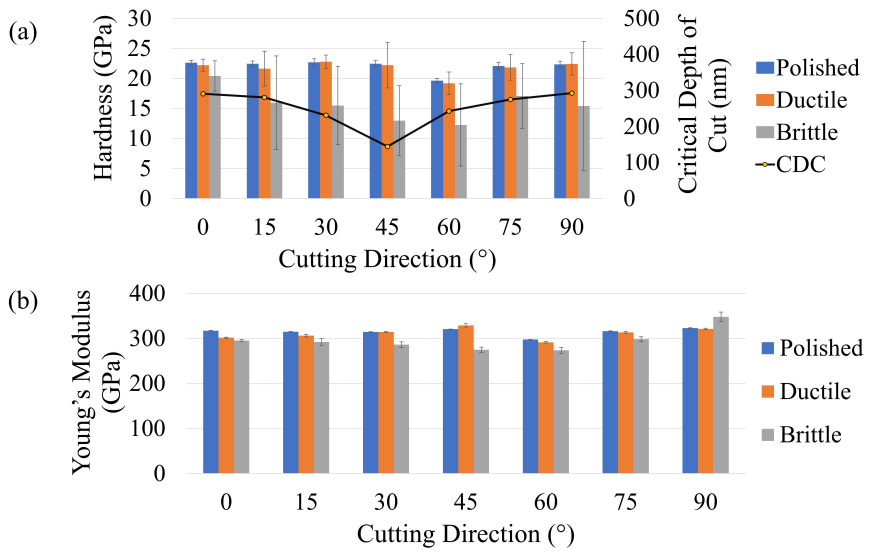

Figure 3.15: (a) Variation in hardness with cutting direction and depth of cut for (001) 8YSZ; (b) Variation in Young's modulus with cutting direction and depth of cut for (001) 8YSZ.

Figure 3.15 shows the variation in Hardness, CDC and Young's modulus for different cutting directions on the (001) plane of 8YSZ. It was observed that the hardness in the brittle region was lower than that of the ductile or polished regions. On average, the hardness was 22.05 ±0.5 GPa in the polished region, 21.76 ±2.1 GPa in the ductile region, and 15.66 ±6.5 GPa in the brittle region which indicates a reduction in compliance in the brittle regions. The variation in the Young's modulus showed a similar trend for most of the cutting directions. The average value of Young's modulus in the polished region was 314.85 ±4.6 GPa, 311.07 ±17.9 GPa in the ductile machined region, and 295.45 ±73.3 GPa in the brittle region.

The average value of residual stress for each cutting direction with increasing depth of cut in 20 nm increments on the (001) plane of 8YSZ is plotted in Figure 3.16. The common trend observed was that in the ductile region, the residual stress magnitude was fairly consistent for a given cutting direction and there were large variations in the brittle region, starting around the CDC. The residual stresses ranged from -200 MPa (compressive) to 400 MPa (tensile) in the ductile region. For the 0°, 15°, and 75° cutting directions predominantly exhibited tensile residual stress in the ductile region whereas the 30° and 90° cutting directions mostly displayed a compressive residual stress magnitude. In the brittle region, the residual stress values ranged

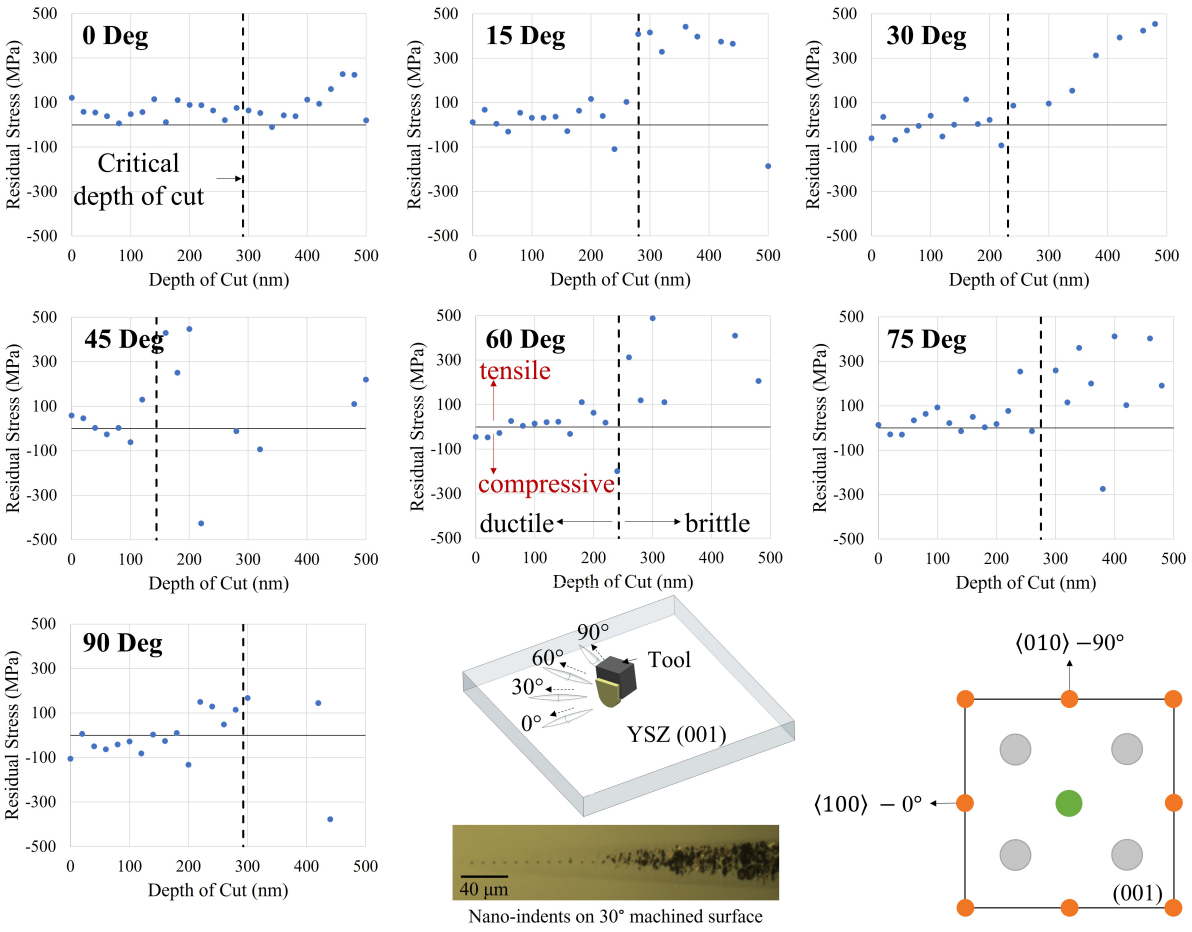

Figure 3.16: Variation in residual stress magnitude with cutting direction and depth of cut for (001) 8YSZ.

more widely from ≈ -2 GPa to ≈ 850 MPa. The large variation in the residual stress magnitude in the brittle regions might be a shortcoming of the approach followed and is discussed further in section 3.3.3.

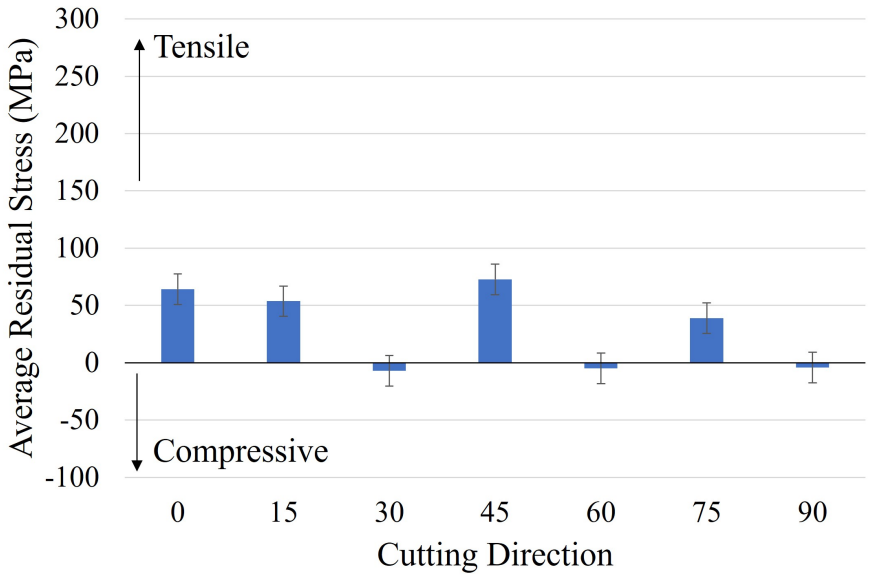

Figure 3.17: Variation in average value of residual stress with cutting direction in the ductile region on (001) 8YSZ.

Figure 3.17 shows the average magnitude of residual stress in the ductile regions for different cutting directions on the (001) plane of 8YSZ. Only the ductile regions were selected due to the fairly constant residual stress magnitude. Due to the very large fluctuations in the brittle regions, a average residual stress value might not make much sense. From the Figure, it was evident that 4 out of the 7 cutting directions (0°, 15°, 45°, and 75°) investigated exhibited a tensile residual stress of about 50 - 60 MPa whereas the residual stress magnitude in the other 3 cutting directions (30°, 60°, and 90°), were negligible.

Figure 3.18 shows the variation in Hardness, CDC and Young's modulus for different cutting directions on the (011) plane of 8YSZ. It was observed that the reduction in hardness in the brittle region was lower than that compared to the results from the (001) plane. This could likely be due to the sparse cracks observed in some of the cutting directions which produce a machined surface similar to the one observed in the R-plane of sapphire in the 180° cutting direction (Figure 3.7). On average, the hardness was 20.36 ±0.5 GPa in the polished region, 20.46 ±1.9 GPa in the ductile region, and 19.44 ±4.11 GPa in the brittle region. A reduction in hardness was observed in the 75° and 90° cutting directions as these cutting directions display a large density of cracks in the brittle region. Similarly, the Young's modulus values showed smaller variations across the different regions where measurements were made. The average

values of Young's modulus were 288.79 ±4.5 GPa in the polished region, 284.40 ±20.4 GPa in the ductile machined region, and 285.44 ±51.5 GPa in the brittle region.

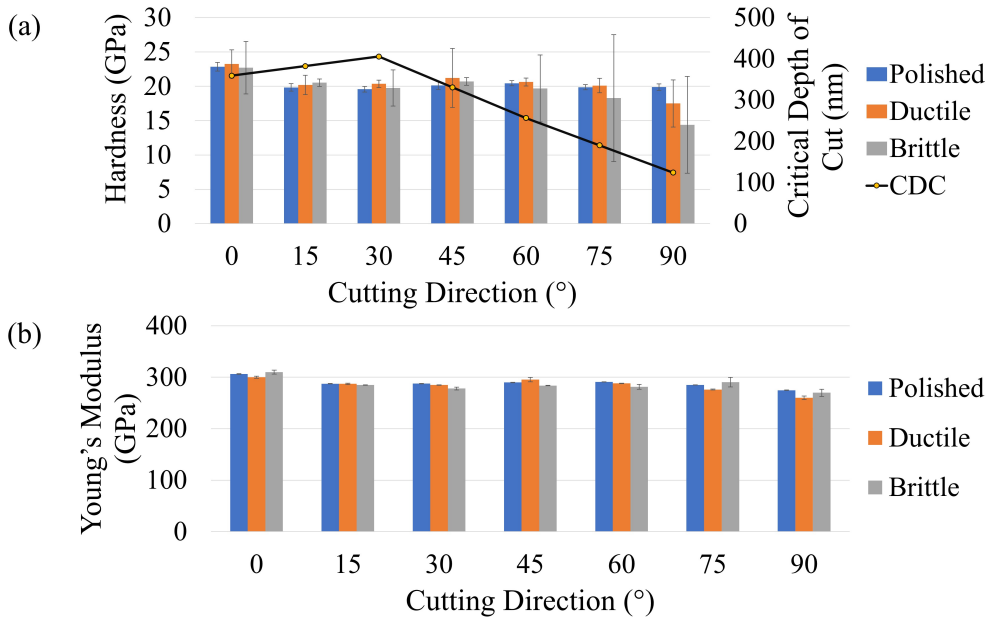

Figure 3.18: (a) Variation in hardness with cutting direction and depth of cut for (011) 8YSZ; (b) Variation in Young's modulus with cutting direction and depth of cut for (011) 8YSZ.

The average value of residual stress for each cutting direction with increasing depth of cut in 20 nm increments on the (011) plane of8YSZ is plotted in Figure 3.19. Since the crack morphology was different on the (011) plane for most cutting directions, compared to the (001) plane, the residual stress values were fairly consistent for those cutting directions with sparse cracks (0°, 15°, 30°, and 45°) where as the residual stress magnitude varied in the brittle region of those cutting directions where a lot of dense cracks were present (60°, 75°, and 90°). The 15°, 45°, and 60° cutting directions exhibited predominantly tensile residual stresses in the ductile region whereas the 0° cutting direction exhibited compressive residual stress in the ductile region of the cut. The residual stress magnitude ranged from -172 MPa (compressive) to 455 MPa (tensile) in the ductile region. In the brittle region, the residual stress values ranged more widely from ≈ -2 GPa to ≈ 550 MPa.

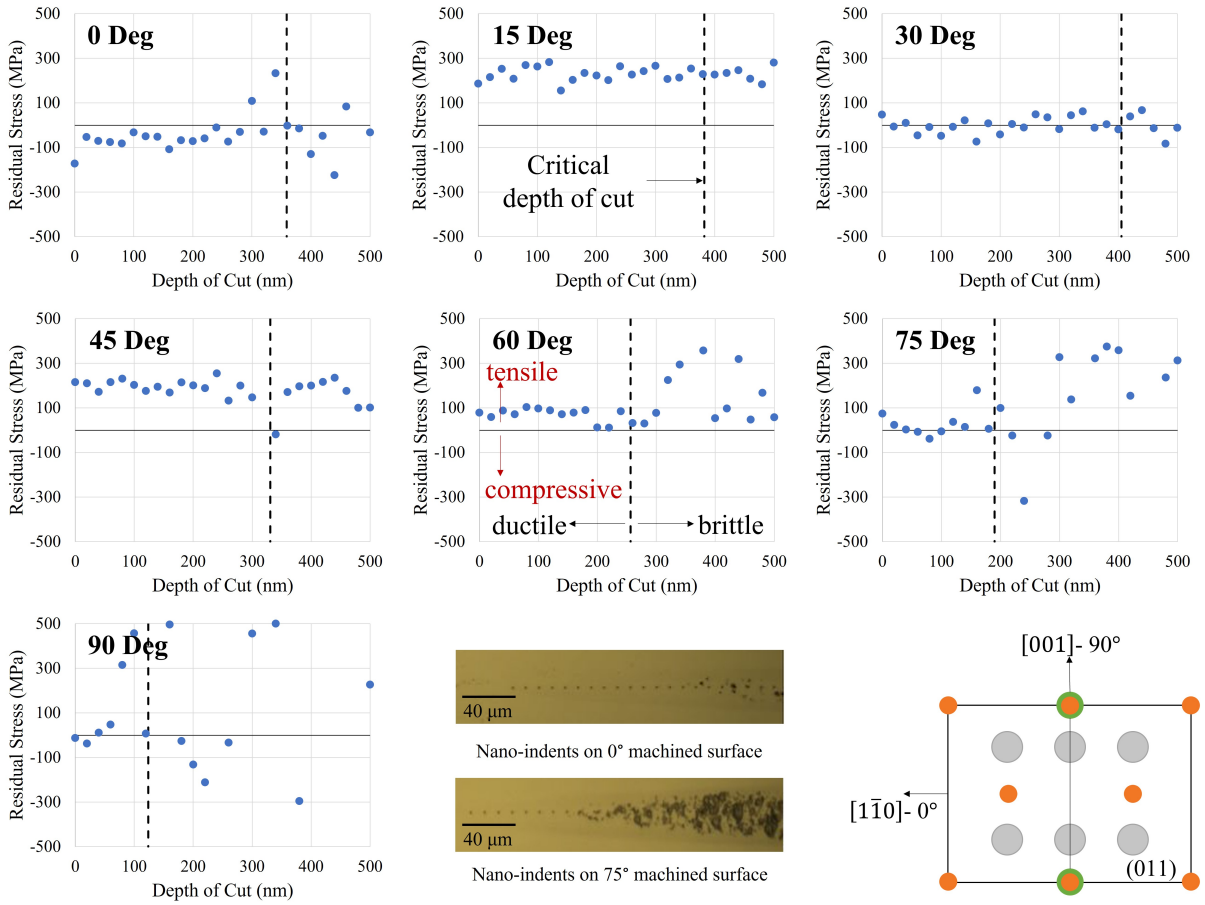

Figure 3.19: Variation in residual stress magnitude with cutting direction and depth of cut for (011) 8YSZ.

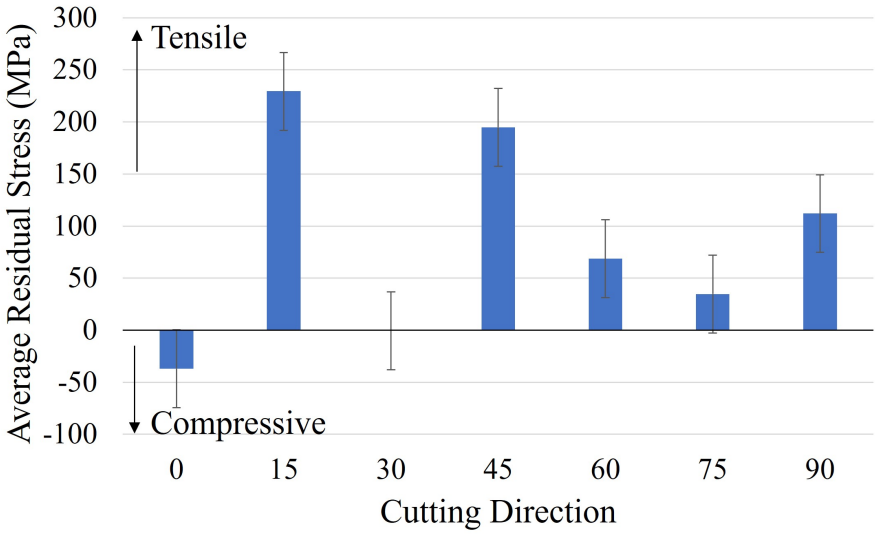

Figure 3.20: Variation in average value of residual stress with cutting direction in the ductile region on (011) 8YSZ.

Figure 3.20 shows the average magnitude of residual stress in the ductile regions for different cutting directions on the (011) plane of 8YSZ. It was observed that compared to the (001) plane, the magnitude of residual stress in the (011) plane was much larger. The residual stress magnitude varied between -35 MPa to 238 MPa. The 15° cutting direction exhibited the maximum tensile residual stress among the different cutting directions investigated. From the Figure, it was evident that 5 out of the 7 cutting directions (15°, 45°, 60°, 75°, and 90°) investigated exhibited a tensile residual stress. The residual stress magnitude in the 60° cutting direction was compressive and that in the 30° cutting direction was negligible.

3.3.3 Understanding Residual Stress in 8YSZ from the Perspective of Elastic and Plastic Energy of Indentation

In the previous section, the residual stress calculation for 8YSZ from nanoindentation data was carried out using the model proposed by Dahmani et al. [100]. This equation used in this method is developed by considering the how the stress field around a crack tip would affect the hardness of the material surrounding the crack. However, when this model was applied to the brittle regions of machined 8YSZ, large variations in the residual stress magnitude were observed. This is likely due to the sudden increase in stress in the immediate vicinity of a crack. Also, it is possible that some of the indents in the brittle area were performed within the crack itself and thus affecting the measurement. To overcome this drawback, an alternate method is presented in this section to study the residual stress distribution in machined 8YSZ by looking at the energy partition during indentation.

Figure 3.21 shows the proportion of elastic and plastic energy in indentation between 100 nm and 440 nm depth of cut for the 30° cutting direction on the (001) plane of 8YSZ. The elastic energy was calculated by measuring the area under the unloading portion of the load-displacement curve and the plastic energy was calculated by subtracting the elastic energy from the area under the loading portion of the load-displacement curve (total energy) (See Figure 3.14). It was observed that the energy partition for the polished reference surface was at 47% elastic and 53% plastic and this was used as a reference value. In the ductile portion of the cut, small variations in the energy contributions were observed but beyond the CDC, the fraction of plastic energy increased significantly.

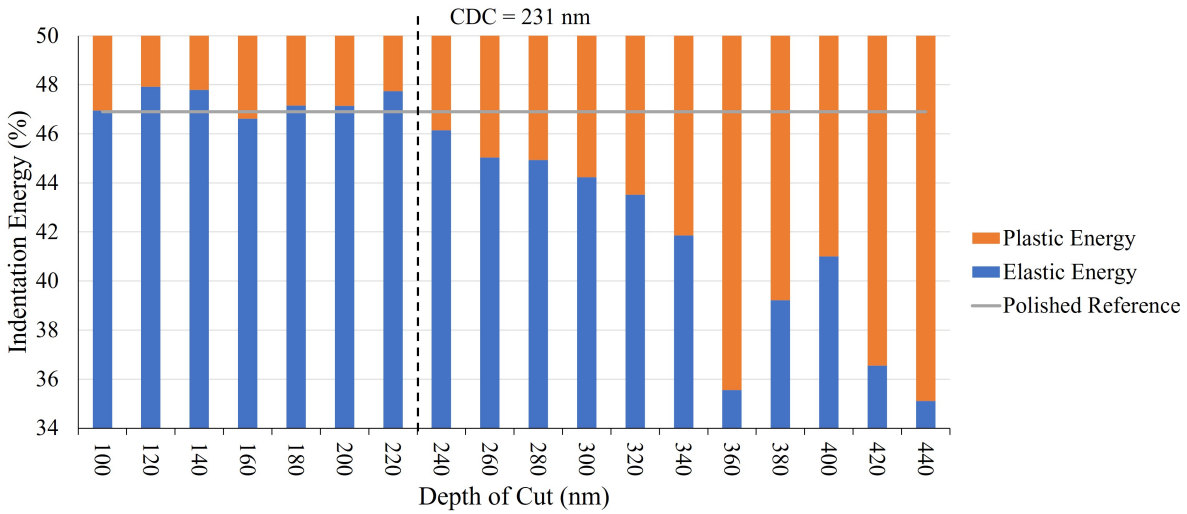

Figure 3.21: Variation in indentation energy composition with depth of cut for (001) 8YSZ in the 30° cutting direction.

One possible analysis method is the approach by Alao and Yin [105], where the resistance to machining-induced cracking was calculated. This term is akin to the fracture energy which represents the amount of energy necessary to open a unit area of a crack. In the cited literature, this term is derived with the assumption that during crack initiation, all the potential strain energy is converted to surface energy.

$$U_t - U_r = R_c \sum_{i=1}^{n} A_i \tag{3.14}$$

where U_t is the total indentation energy (area under the loading curve), U_r is the plastic energy during indentation, R_c is the fracture energy,and A_i is the area of the i^{th} damage or crack. From Irwin's model,

$$R_c = \frac{K_{IC}^2}{E'} \tag{3.15}$$

where K_{IC} is the fracture toughness and E' is the plane strain modulus. Substituting Eq. 3.15 in Eq. 3.14,

$$U_t = \frac{R_c}{1-D} \sum_{i=1}^{n} A_i \tag{3.16}$$

where $D = U_r/U_t$ is defined as the degree of damage. The term resistance to machining-induced cracking (M) can be defined as the inverse degree of damage per unit applied work which is expressed as,

$$M = \frac{U_t}{\sum_{i=1}^{n} A_i} = \frac{R_c \sum_{i=1}^{n} A_i}{(1-D)\sum_{i=1}^{n} A_i} = \frac{K_{IC}^2}{E'(1-D)} \tag{3.17}$$

Based on this equation, if the deformation is purely elastic, $D = 0$ and M will reduce to the fracture energy. On the other hand, if the deformation is completely plastic, $D = 1$ and M will tend to infinity. To summarize, as the amount of plastic deformation increases, the value of M also increases. At this stage, an assumption is made that as the tensile residual stress increases in a material, it becomes easier to plastically deform it leading to an increase in the value of resistance to machining-induced cracking and if the compressive residual stress increases in the material, larger amount of stress would be necessary to plastically deform the material and the value of resistance to machining-induced cracking would decrease.

Using this approach, the resistance to machining-induced cracking was calculated for the 7 different cutting directions on the (001) and (011) planes of 8YSZ as shown in Figures 3.22 and 3.23, respectively.

From Figure 3.22, it can be observed that the in the ductile region of the cut, the resistance to machining-induced cracking is about 23 J/m^2 for most of the cutting directions on the (001) plane of 8YSZ which is of similar value to the polished reference. As the depth of cut is increased, the value of resistance to machining induced cracking generally increases up to 60 J/m^2 in some cases. The large variation in the brittle region could potentially be attributed to the dense crack morphology observed for most of the cutting directions on the (001) plane of 8YSZ The higher value of resistance to machining induced cracking potentially implies there is more plastic deformation activity in the brittle regions around the cracks. Although crack initiation would relieve the built up stresses, it is likely that there would still be plastic deformation activity around the cracks and needs to be investigated further.

Figure 3.23 shows the resistance to machining induced cracking in the case of the (011) plane of 8YSZ. Compared to the (001) plane, the values of resistance to machining induced cracking in the ductile region in the (011) plane were closer to 30 J/m^2 and the values in the brittle

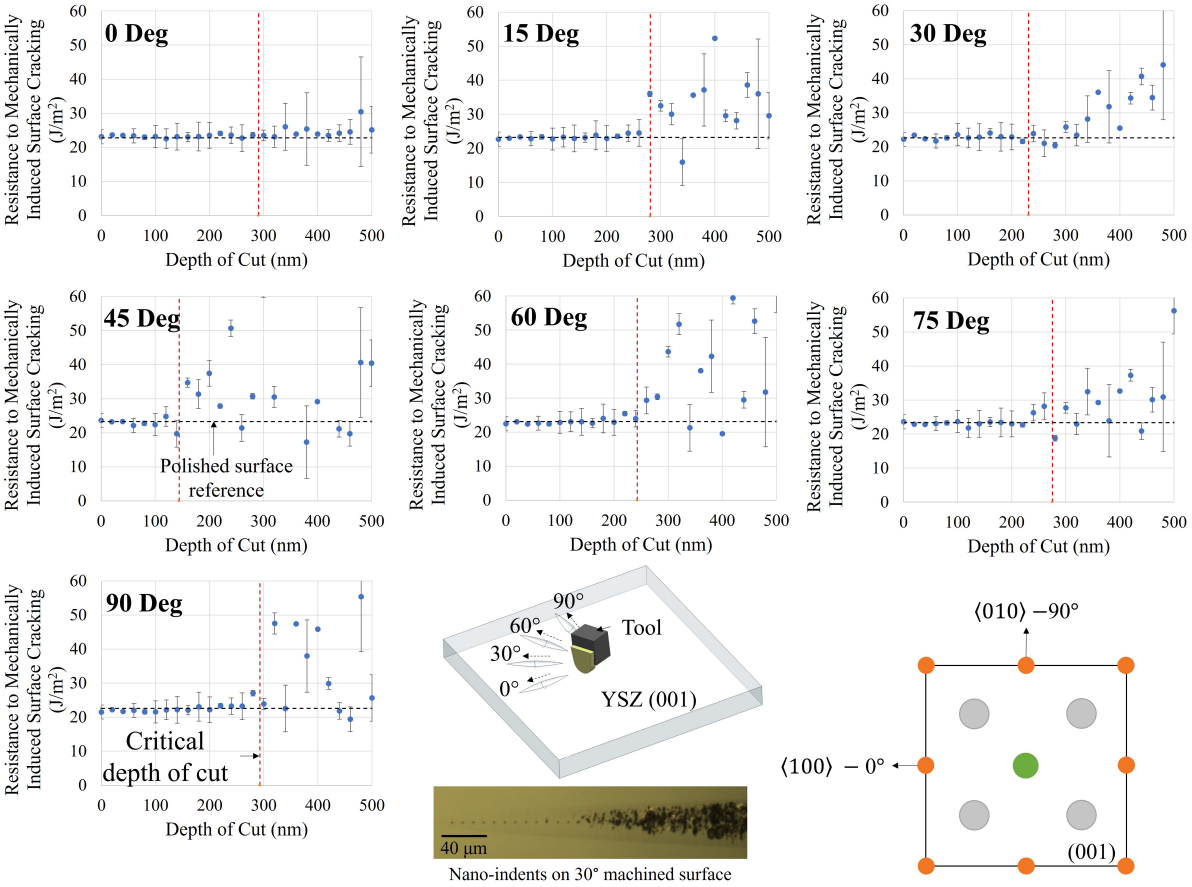

Figure 3.22: Variation in resistance to mechanically induced surface cracking with cutting direction and depth of cut for (001) 8YSZ.

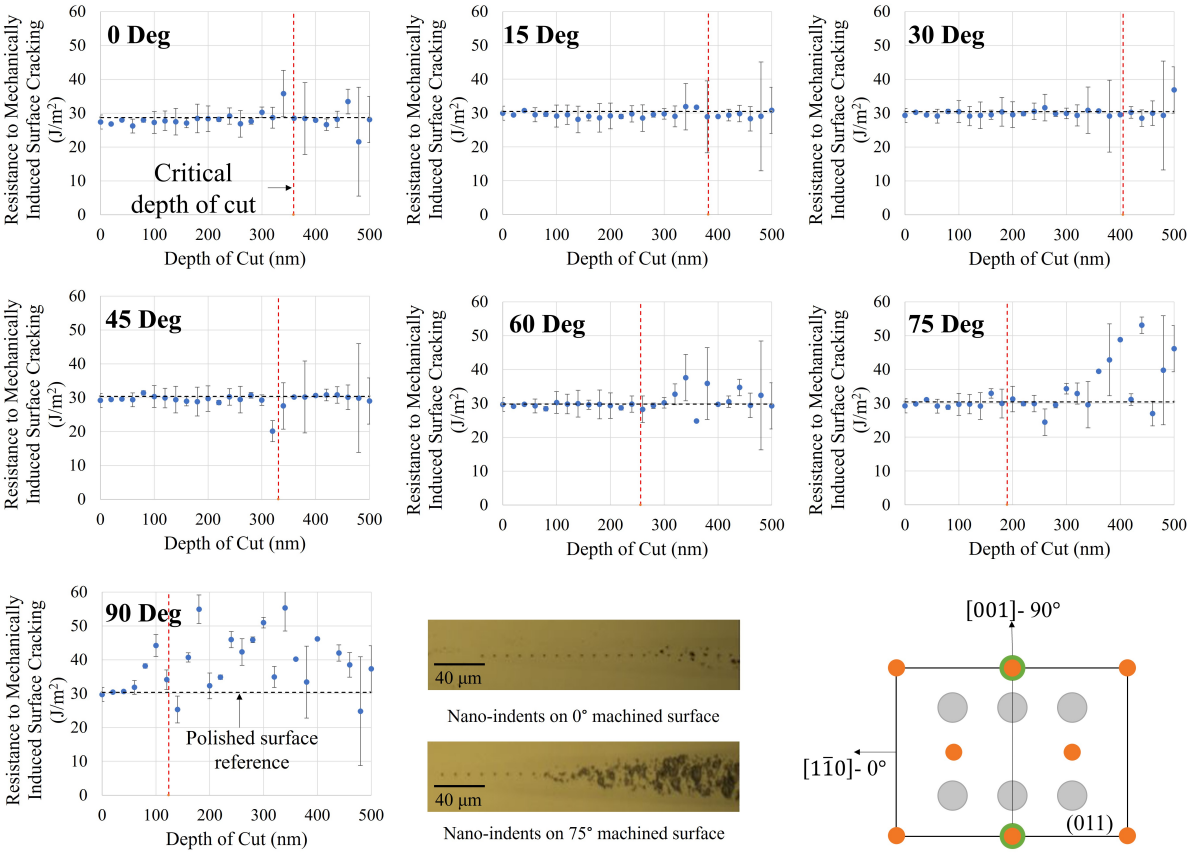

Figure 3.23: Variation in resistance to mechanically induced surface cracking with cutting direction and depth of cut for (011) 8YSZ.

region went up to 55 J/m^2. This higher value of resistance to machining induced cracking could potentially explain the larger magnitude of residual stress compared to the (001) plane. Further, unlike the (001) plane, it was observed that the cracking was not as severe in some of the cases such as 0°, 15°, 30°, and 45° cutting directions and as a result showed smaller variations. In the ductile region of these cutting directions, it was observed that the resistance to machining induced cracking was about 2-4 J/m^2 lower than the value of the polished reference.

To summarize, this chapter aimed to measure the anisotropy in residual stresses in machined sapphire and 8YSZ. Two different measurement techniques - Raman spectroscopy and nano-indentation were used to measure the residual stress magnitude in the case of sapphire and 8YSZ respectively. It was observed that the cutting direction and depth of cut had an impact on the magnitude of residual stress and this was explained from the perspective of activation of different plastic deformation mechanisms and the amount of plastically deformed material left behind in the workpiece. From these results, it is clear that residual stress formation, especially in the DBT and brittle regions is a complex interplay between plastic deformation and stress relief by crack initiation. These topics will be explored in more detail in the next chapter on subsurface damage.

Chapter 4

Subsurface Damage

During the machining process of hard and brittle materials like ceramics, subsurface damage has been known to influence the outcome of the machining process. Broadly, this chapter deals with the measurement of subsurface damage and understanding the correlation between activation of different deformation mechanisms and the magnitude of subsurface damage. This chapter is divided into four sections - the first section is a literature review on subsurface damage during machining of ceramic materials. This section mainly addresses the different types of subsurface damage, causes, modeling of subsurface damage formation, and the different methods used to quantify subsurface damage. The next section deals with the application of Raman spectroscopy to quantify subsurface damage in sapphire and also examines the effect of crack morphology on influencing the damage magnitude. The third section covers results from the MD simulation studies performed to better understand the evolution of damage mechanisms in the subsurface and provides a qualitative estimate of subsurface damage for different cutting orientations in sapphire. The final section of this chapter goes into the details of using TEM to study subsurface damage in machined ceramics. Additionally, this section covers TEM sample preparation in detail, explaining the common challenges and methods to overcome them. Finally, the TEM observations are compared with the predictions from the P- and F- parameter deformation model presented in Chapter 2.

4.1 Literature Review

In addition to the residual stress, it is also important to investigate different types of subsurface damages and defects as some types of defects like micro-cracks and voids can cause the initiation of larger cracks whereas other types of defects like dislocations and twin boundaries can affect plastic deformation or initiate micro-voids under some conditions [106–108]. Subsurface defects have been studied using a variety of techniques such as angle polishing, transmission electron microscopy (TEM), dimpling, chemical etching, etc. The method selected mainly de-

pends on the size and type of defects being investigated and the material being studied. In the case of UPM of ceramics, methods such as TEM and bonded interface technique are useful as the region that needs to be investigated is generally small and defects such as dislocations and microcracks can be visualized using these techniques [109]. Yuta et al. investigated the effect of crystal anisotropy on subsurface damage during ultra-precision turning of calcium fluoride using TEM and showed that the amount of subsurface damage varied depending on crystal orientation and tool geometry [110]. Zhou et al. reported an increase in subsurface damage with increase in machining depth during the diamond grinding of silicon [111]. In ultra-precision turning studies on silicon and germanium conducted by Blake et al., dislocation layers extending up to a few tens of micrometers below the surface were observed [112]. Yan et al. investigated the influence of cutting direction on extent of subsurface damage in machined silicon using micro-Raman spectroscopy and correlated the subsurface damage magnitude to the slip factor [113]. Through TEM evaluation of nano-scratching tests on sapphire, Lin et al. observed dislocations on various slip systems and micro-crack extending to the depth of about 2.5 μm depending on the scratching direction [114]. Through these studies it is evident that subsurface damage is dependent on factors such as the cutting direction and machining process parameters. Also, the presence of multiple types of defects such as dislocations and microcracks in the same TEM image could indicate a potential for interactions between these defects which would have an effect on subsequent deformation in the material. The evolution of different types of defects and their interactions during UPM of single crystal ceramics is not fully understood and need to be addressed to develop machining strategies that minimize surface and subsurface damage.

4.2 Using Raman Spectroscopy for Subsurface Damage Measurements

Based on the studies by Yan et al., Raman spectroscopy can be used to investigate subsurface damage in machined ceramics. Typically, the less defects in a single-crystalline material, the narrower will be the Raman peak width and as the number of defects or amorphization increases, the Raman peak will tend to broaden. In certain materials like silicon, the appearance of new peaks and broadening of specific peaks can be correlated to phase transformation

and amorphization, respectively [115, 116]. However, even though this type of granular analysis might not be possible for other materials, Raman spectroscopy still provides valuable information about the extent of subsurface damage for a qualitative comparison between different processing conditions. This approach was followed by Onuki et al. for their investigations on subsurface damage in polished sapphire samples [117]. In this section, results from 2 sets of experiments are presented. The first set of experiments investigated the variation in peak width with respect to the depth below the machined surface for a few cutting directions. The second set of experiments mainly investigated the peak width variations in the vicinity of the machined surface and compared the variations in the peak width with the crack morphology for different cutting directions on the A-, C-, M-, and R- planes of sapphire.

4.2.1 Variation in Subsurface Damage with Depth

To investigate the variation in peak width with respect to the depth beneath the machined surface, 4 different cutting directions were chosen from the R-plane of sapphire (R180, R210, R240, and R270). The reason for selecting these directions was mainly due to the large differences in surface crack morphology and residual stress magnitude (see Figure 3.6). Raman measurements were carried out using the parameters detailed in section 3.2.1 except that, instead of mapping the Raman spectrum over an area on the machined surface, a depth-wise map was created up to a depth of 4 μm in increments of 0.8 μm in the brittle regions of the cutting directions mentioned. Following the data collection, the Full Width at Half Maximum (FWHM) was calculated for the 417 cm^{-1} Raman peak. Akin to previous Raman measurements (section 3.2.2), the 417 cm^{-1} peak was selected due to it's large intensity compared to other Raman peaks at the short exposure times used for the measurements. Although it is not possible to point out the kind of defects or the exact depth of subsurface damage through this method, a qualitative comparison between different cutting directions allows for a better understanding of how crack morphology might influence subsurface damage depth.

As per the results shown in Figure 4.1, the amount of peak width variation differed based on the cutting direction with bluer shades representing narrower peak widths - highly crystalline regions with minimal defects and redder shades representing regions with higher peak width due to the presence of defects. The maximum damage depth was observed in the 180° cutting

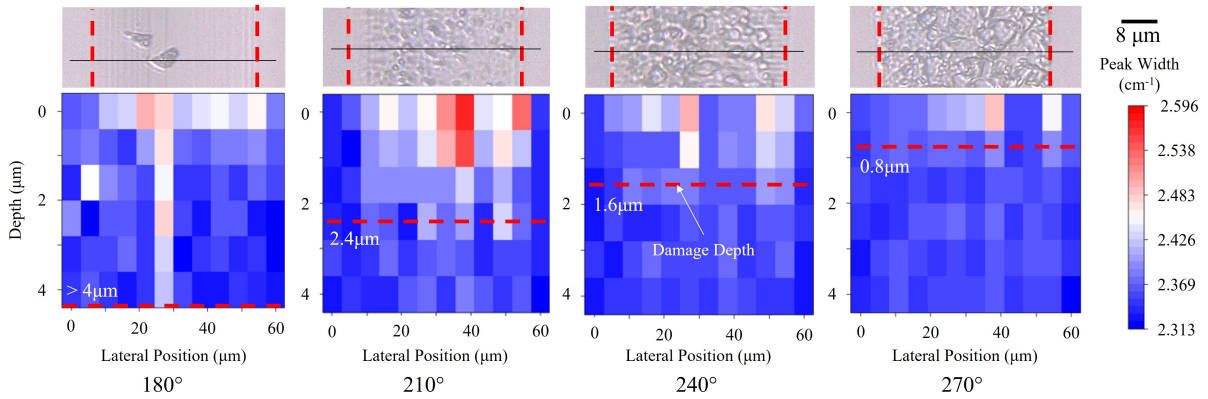

Figure 4.1: Variation in 417 cm^{-1} Raman peak width and crack morphology with cutting direction on R-plane of sapphire.

direction which showed significant peak broadening at depths grater than 4 μm. Although, it must be noted that this peak broadening was observed only below the region with a crack. The 210° cutting direction on the other hand showed significant peak broadening up to a depth of 2.4 μm, but at lower depths the magnitude of peak broadening was higher than that of the 180° cutting direction. In the case of the 240° cutting direction, the peak broadening was limited to a depth of about 1.6 μm and in the case of the 270° cutting direction, the peak broadening was even closer to the surface. It was also observed that in the case of the the 180° cutting direction, the cracks were isolated and there were large regions of ductile machining around them, whereas in the other cutting directions, the cracks were more evenly distributed across the machined surface. Following the results by Kwon et al., the crack morphology is dominated by activation of rhombohedral and prismatic cleavages in the case of the 180° cutting direction which could potentially lead to deeper cracks and greater subsurface damage but, in the other cutting directions, only prismatic cleavages are dominant which potentially leads to the formation of shallower cracks [63]. Something to be noted here is that the cracks in the surface and subsurface have a three-dimensional structure and it might not be able to always capture the entire region in a single spot/line scan with the Raman confocal laser and the results could be biased by the measurement region selected. However, due to time and resource constraints, full three-dimensional mapping of peak width variations was not carried out in this study.

4.2.2 Variation in Subsurface Damage on Different Crystallographic Planes

In this section, the effect of cutting orientation, cutting depth, and crack morphology on Raman peak broadening and subsequently subsurface damage is investigated in more detail. Raman measurements were carried out using the parameters detailed in section 3.2.1 along the 7 cutting orientations previously selected on the A-, C-, M-, and R-planes of sapphire and in the ductile, ductile-brittle transition, and brittle regions. The 2D mapping measurements were carried out over the machined area, with the laser focus being on the plane of the machined surface. The measurements were then compared to the polished region of the sample to determine the difference in peak width between the machined and polished regions of the sample. Once again, the 417 cm^{-1} peak was selected due to it's large intensity compared to other Raman peaks at the short exposure times used for the measurements. While analyzing this larger sample of data, it was observed that the intensity of the peaks peaks changed depending on the crystal orientation mainly due to the anisotropic nature of the laser-phonon interactions [92]. To account for this, the subsequent analysis presents a normalized peak width value which is the FWHM value normalized over the average peak intensity for the given cutting direction and depth of cut. Additionally, in this section, the variation in peak width is compared to SEM images showing the crack morphology for the different cutting directions. The SEM images were acquired in collaboration with Suk Bum Kwon at the MIN lab and some of the images or a version of the images have been published in [63] and [118] which explain the activation of specific types of cleavage fracture systems during cutting. In this study, the crack morphologies are used from the perspective of understanding their effect on the subsurface damage magnitude.

Figure 4.2 shows the variation in normalized Raman peak width for different cutting directions and depths of cut on the A-plane of sapphire. In general, the peak width variations followed a similar tendency to the that of the residual stress magnitude shown in Figure 1.2. In general, the variation in peak width in the ductile-brittle transition and brittle regions was larger than that in the ductile regions of the cut. This observation further makes the link between the crack morphology and subsurface damage amount. Like the case of the residual stress measurements, the 30° and 60° cutting directions showed the maximum amount of peak width variations whereas the 150° and 180° cutting directions showed the minimum peak width

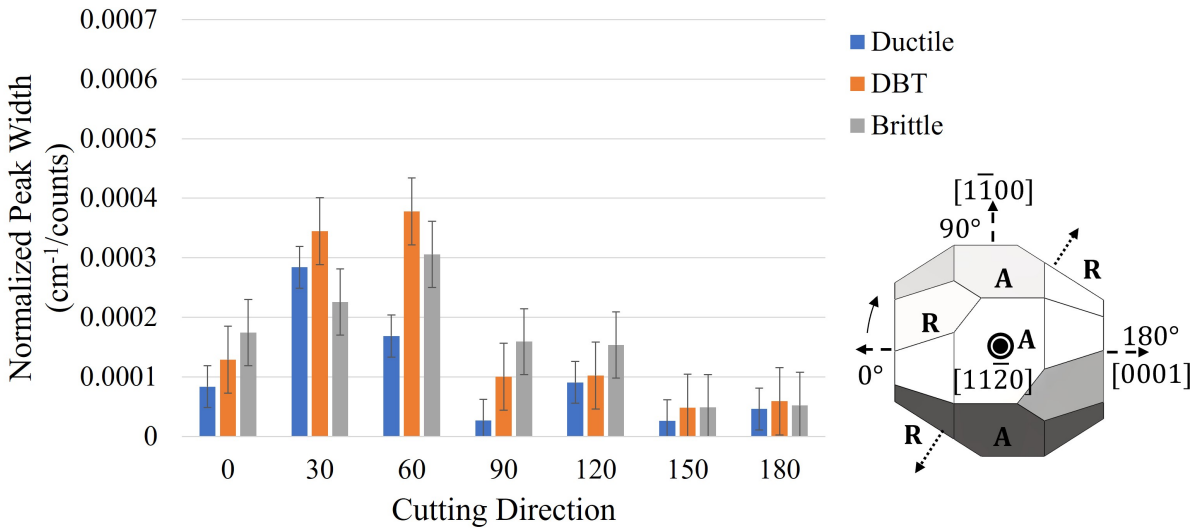

Figure 4.2: Variation in Raman peak width with cutting direction and depth of cut on A-plane of sapphire.

variation.

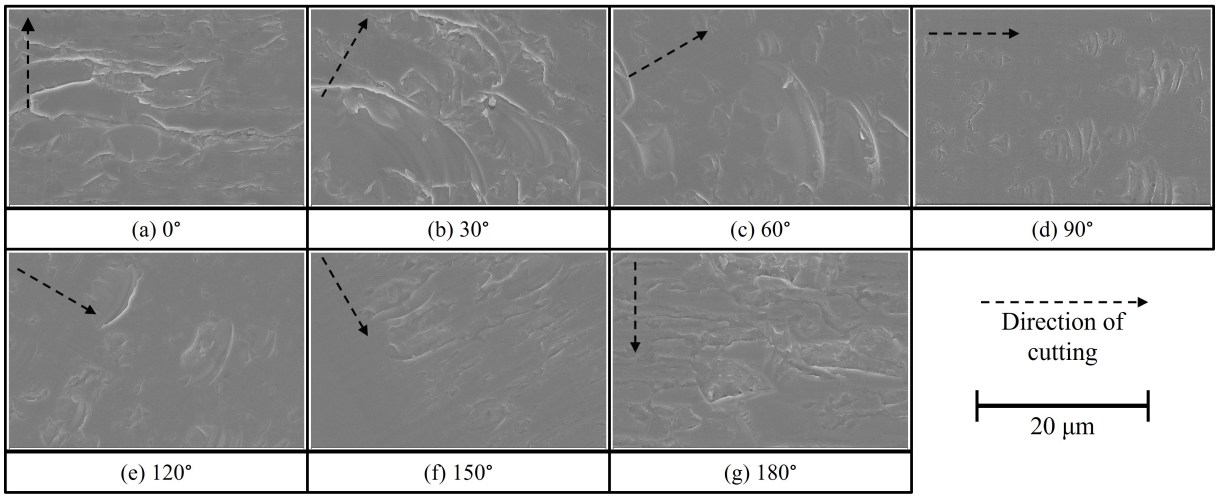

Figure 4.3: Variation in crack morphology with cutting direction on A-plane of sapphire [63,118].

Figure 4.3 shows the crack morphology observed on different cutting directions on the A-plane of sapphire. Most of the cracks on the A-plane of sapphire were lamellar or fan-shaped. Although, depending on the cutting direction, the severity of the cracking, size and density of the cracks on the machined surface varied greatly. In cutting directions such as 0°, 30°, and 60°, the cracks appear to be in a higher density and deeper than the other cutting orientations whereas cutting directions like 90° and 150° show much more sparse and shallow cracks. On

the A-plane, most of the cracks were governed by the activation of prismatic and rhombohedral cleavages in varying amounts, depending on the cutting direction which influenced the depth and density of the cracks formed and subsequently the subsurface damage [118].

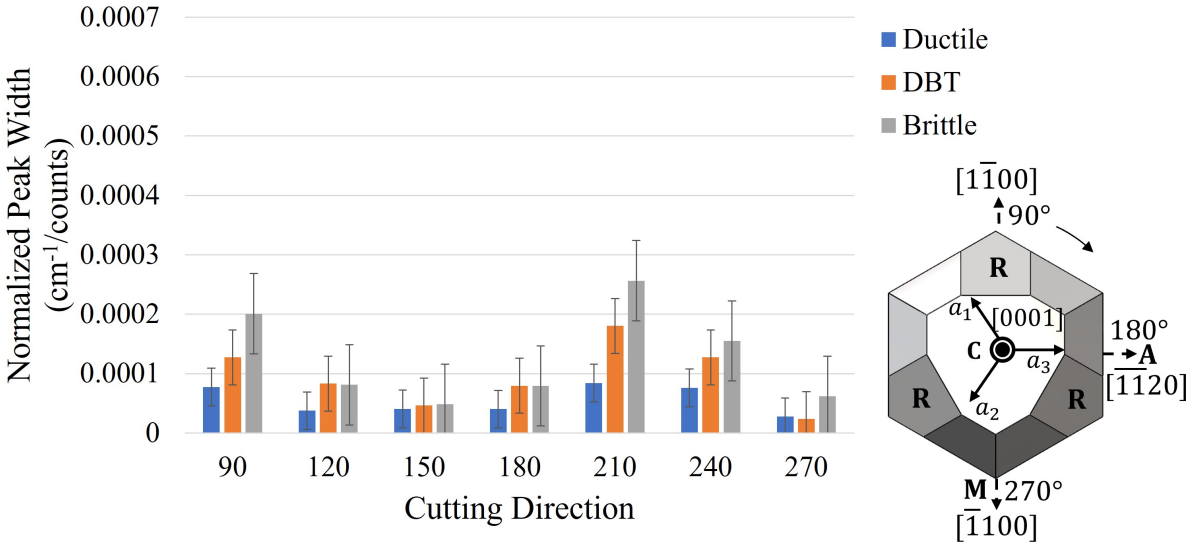

Figure 4.4: Variation in Raman peak width with cutting direction and depth of cut on C-plane of sapphire.

The variation in normalized Raman peak width for different cutting directions and depths of cut on the C-plane of sapphire is shown in Figure 4.4. In general, the peak width variations on the C-plane were among the lowest compared to the other crystallographic orientations studied. Unlike the uniformly low residual stress magnitude shown in Figure 3.4, some of the cutting directions on the C-plane (90° and 210°) showed higher peak width magnitudes compared to other cutting directions. Like the case of the A-plane, variation in peak width in the brittle regions was larger than that in the ductile-brittle transition and ductile regions of the cut. Among the other cutting directions, 90°, 150°, and 270° cutting directions showed the minimum peak width variation.

Figure 4.5 shows the crack morphology observed on different cutting directions on the C-plane of sapphire. In the case of the C-plane, most of the appeared to be shallow in nature compared to all the other cutting directions and cutting planes. The crack morphology on the C-plane predominantly consisted of layered and spalling cracks triggered by the activation of the basal cleavage system. In the 90° and 210° cutting directions, lamellar sculptured cracks

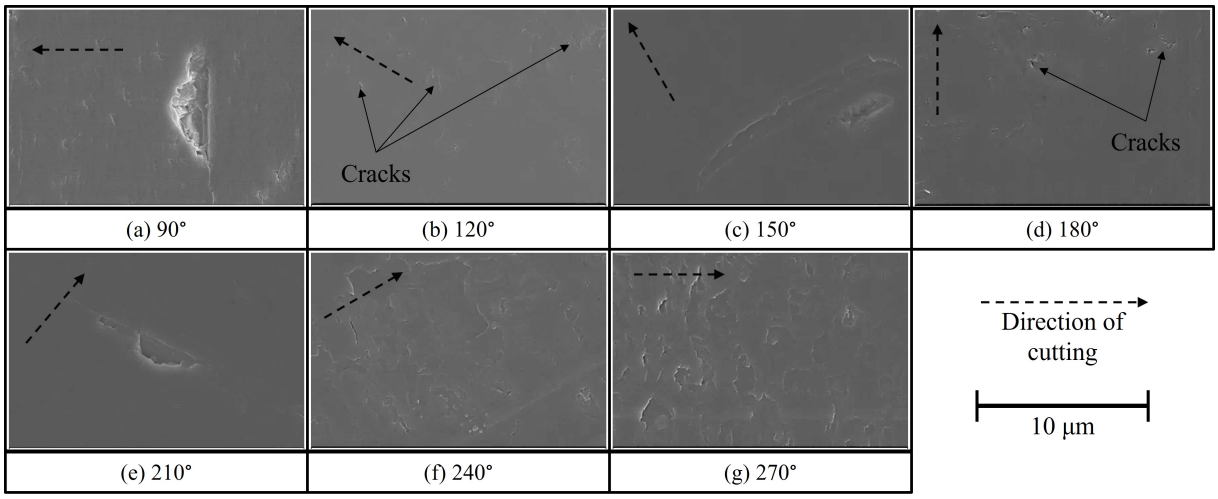

Figure 4.5: Variation in crack morphology with cutting direction on C-plane of sapphire [63,118].

were also observed caused mostly by the activation of prismatic cleavages resulting in cracks that extend further into the subsurface. As a result, the peak width variation observed was also larger in these cutting directions. Overall, due to the smaller number of cracks over a given area and shallow nature of cracks in most cutting directions on the C-plane, the subsurface damage is lower [118].

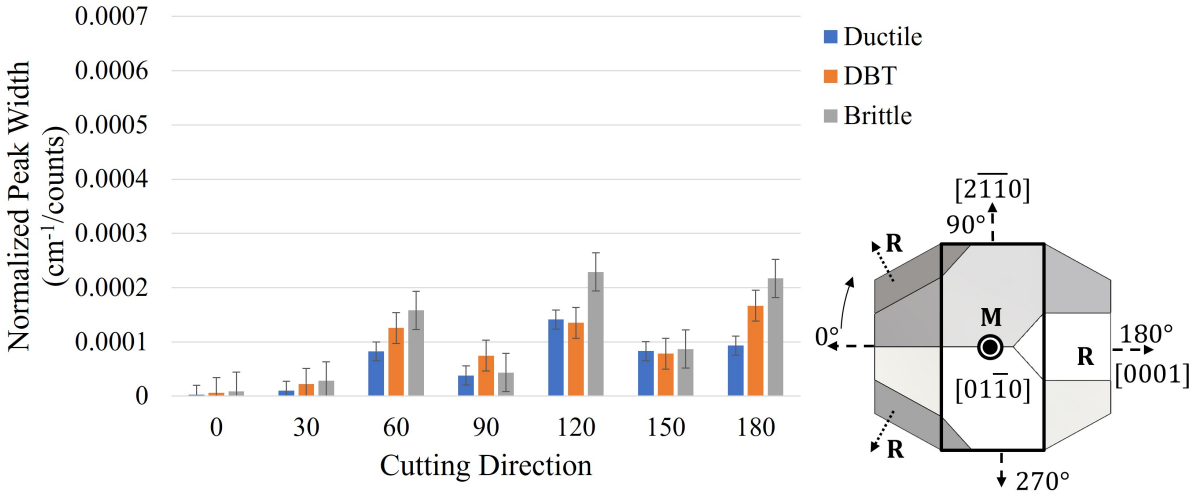

Figure 4.6: Variation in Raman peak width with cutting direction and depth of cut on M-plane of sapphire.

Figure 4.6 shows the variation in normalized Raman peak width for different cutting directions and depths of cut on the M-plane of sapphire. The peak width variations followed a similar trend to the that of the residual stress magnitude shown in Figure 3.5. In the case

of the M-plane, the variation in the peak width magnitudes were large for the 60°, 120°, and 180° cutting directions whereas it was minimal in the case of the 0°, and 90° cutting directions. Overall, compared to the other crystallographic planes, the variation in magnitude of the peak width was similar to the C-plane, i.e. lower than the values observed in the A- and R-planes of sapphire. Once again, the magnitude of peak width variation was larger in the ductile-brittle transition and brittle regions compared to the ductile depths of cut.

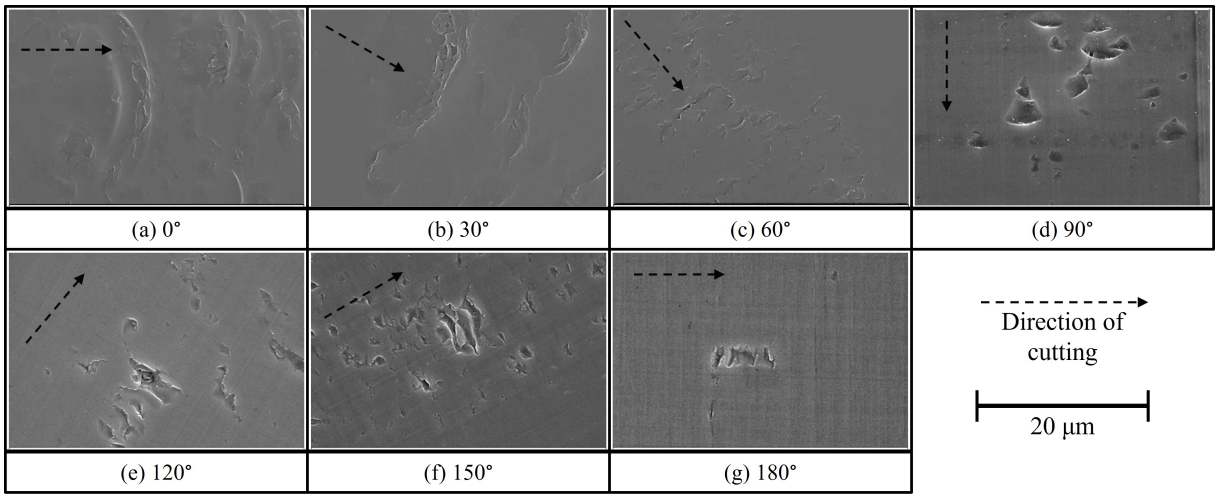

Figure 4.7: Variation in crack morphology with cutting direction on M-plane of sapphire [63,118].

Figure 4.7 shows the crack morphology observed on different cutting directions on the M-plane of sapphire. On the M-plane, the crack morphology was predominantly fan-shaped lateral cracks in the case of the 0°, 30°, 60°, and 90° cutting directions and hybrid cracks comprising of spalling and sculptured cracks in the case of the 120°, 150°, and 180° cutting directions. All the crack morphologies observed in the M-plane were caused by varying activation of rhombohedral and prismatic (A-plane cleavages). The fan shaped cracks were shallower in nature and had a higher activation probability of rhombohedral cleavage but in the case of the cutting directions with hybrid cracks, the tendency of activation of prismatic cleavages had increased considerably [118]. Also, as the prismatic plane is perpendicular to the M-plane, the cracks tended to be deeper and subsequently showed higher amount of peak width broadening in the Raman measurements.

Variations in the normalized Raman peak width for different cutting directions and depths of cut on the R-plane of sapphire are shown in Figure 4.8. The R-plane showed a clear anisotropy

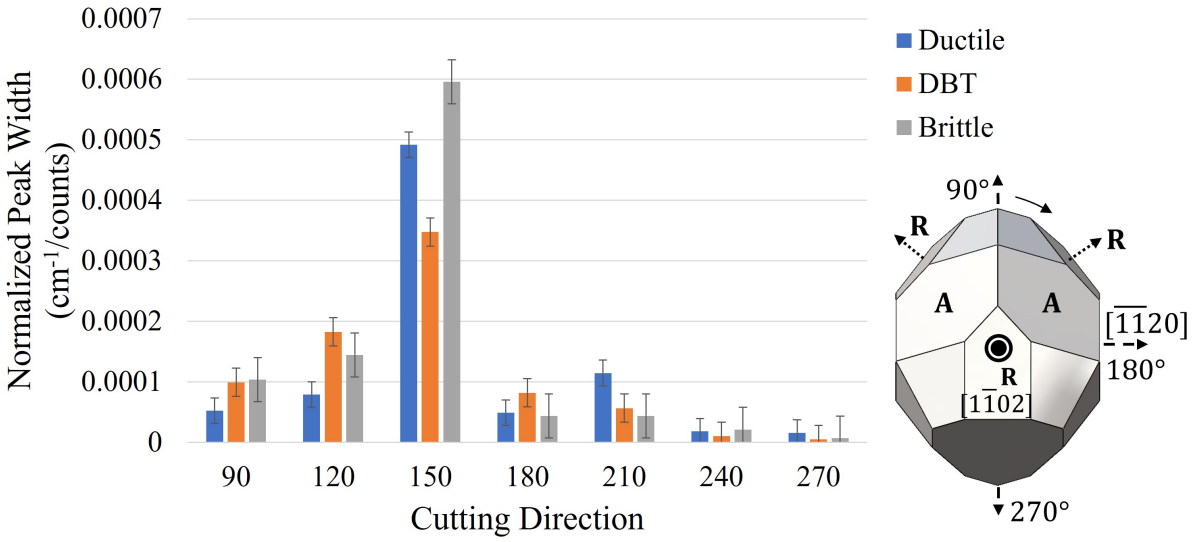

Figure 4.8: Variation in Raman peak width with cutting direction and depth of cut on R-plane of sapphire.

when it came to variations in the peak width. The 150° cutting direction had the maximum peak width variation compared to all the directions evaluated followed by 90° and 120° cutting directions which showed a sizable peak width variation and the 240° and 270° cutting directions showed very small variations in the peak width. This type of trend was similar to that observed with the residual stress magnitude for the case of the R-plane (Figure 3.6). Like the other cutting directions and cutting planes, the magnitude of peak width variation was larger in the ductile-brittle transition and brittle regions compared to the ductile regions.

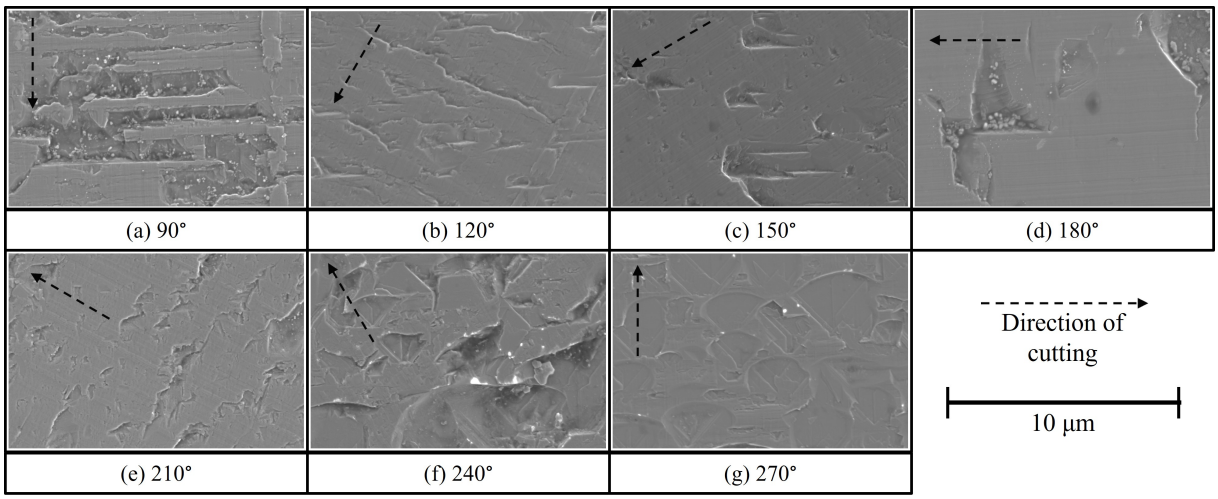

Figure 4.9: Variation in crack morphology with cutting direction on R-plane of sapphire [63,118].

Figure 4.9 shows the crack morphology observed on different cutting directions on the R-plane of sapphire. Compared to all the crystallographic planes evaluated, the R-plane had the most diverse crack morphology. The 90° cutting direction showed lamellar and sculptured cracks, the 120° cutting direction showed sculptured cracks, sculptured and spalling cracks were observed in the 150° cutting direction, and spalling cracks were observed for the remaining cutting directions. In the case of the 90° and 120° cutting directions, the crack initiation was dominated by basal cleavage which resulted in mostly linear features on the brittle machined surfaces. As the cutting direction changed towards 150° and 180°, prismatic cleavages started to become more dominant. Further, in the 210°, 240°, and 270° cutting directions, there was an influence of rhombohedral cleavages which resulted in the bottom surfaces of the spalling cracks which limited the depth of crack propagation resulting in smaller amount of Raman peak width variation [118].

Although Raman spectroscopy can be an useful tool in understanding subsurface damage in machined ceramics, some limitations exist while investigating sapphire. Firstly, as the Raman signal from sapphire is not as strong as that of silicon, longer scan times are necessary. This could lead to annealing due to laser heating. Next, as the method relies on peak width data, it is difficult to identify the specific deformation mechanisms contributing to the subsurface damage. And lastly, as Raman is a volumetric analysis technique, it is difficult to identify the exact depth of subsurface damage which could be useful while determining machining parameters such as the depth of cut. To overcome these drawbacks, TEM evaluations were also conducted to better understand the phenomenon of subsurface damage generation and validate some of the Raman spectroscopy results. These results are presented in section 4.4. Prior to that, results from the analysis of MD simulations are presented first to better understand how defects evolve in the subsurface with respect to the cutting direction.

4.3 MD Simulations

It is evident from the investigations thus far that, the subsurface damage and residual stresses in machined single crystal ceramics are strongly influenced by the activation of specific plastic deformation and cleavage mechanisms and it is important to develop a deeper understanding on material deformation to better predict residual stresses and subsurface damage. Additionally,

due to the small scale of the machining and deformation process, observing the experiments temporally is challenging and MD simulations help in this regard. As part of a collaborative study with colleagues at the University of Cincinnati, MD simulations were used to understand the activation of different deformation mechanisms and their contribution to residual stresses and subsurface damage, the details of which are described in section 2.4. The substrate deformation was quantified by the mean-square-difference between the actual displacement and the ideal displacement due to the affine transformation denoted by D^2 [119] which was then plotted to visualize the activation of different slip/twinning and fracture mechanisms using the OVITO software [120]. Although it is difficult to conduct MD simulations at the same processing conditions as the experiments, a one to one comparison might not be possible. However, MD simulations provide a general trend of how deformation mechanisms might change with cutting direction and temporally. Especially, the evolution of different defects over time.

From these simulations, the maximum depth of deformation was measured after 250 ps of cutting and plotted for the different cutting directions (Figure 4.10 (a)). In some of the cutting directions (A-plane - 60°, C-plane - 270°, and R-plane - 90°), a crack initiation was observed underneath the tool and these cutting directions are highlighted in red [121]. Comparing the trends in the subsurface damage depth with the values of critical depth of cut measured by Yoon et al. [30], the cases of A60 and C270 which show higher values of damage depth than the other cutting direction on the same plane exhibited a lower CDC in the experiments. Also, the R90 and R270 cutting directions had a low but similar value of CDC and show similar values of maximum damage depth in the MD simulations.

Figure 4.10 (b) shows the material deformation as per MD simulations for those cutting directions where a crack was not observed beneath the tool. In the case of the A120 cutting direction, a crack was observed in front of the tool and it is likely that this region would be removed during chip formation. As a result, these cutting directions are expected to show a more ductile surface. In the case of A120 cutting direction, the deformations were mostly driven by rhombohedral twinning and slips on the lesser known n-plane of sapphire $\{22\bar{4}3\}\langle 10\bar{1}0\rangle$. In the case of the C180 cutting direction, the deformation was mostly driven by basal and rhombohedral twinning, with the basal twinning being the more dominant mechanism. In the R270 cutting direction, the deformation was predominantly on the n-plane of sapphire. In the

MD simulations, the deformations along the n-plane of sapphire were identified based on the angle formed by the regions of higher deformation compared to the workpiece surface and cutting direction and these observed slips did not match any of the other well known slip directions listed in Table 2.1. Based on this observation, the crystallography of sapphire was revisited and the other lesser known slip systems were identified [29]. It is likely that this and few other slip systems could get activated in sapphire at much higher temperatures or under high strain rates as in the case of the MD simulations. Additionally, as the CRSS values for this system were not found in literature, it was not included in the analysis predicting deformation behavior.

Figure 4.10 (c) shows the MD simulations of those cutting directions where a crack was observed beneath the tool. In these cases, it is unlikely that the crack would be removed by chip formation and these cutting directions are expected to have higher amounts of subsurface damage. In the case of the A60 cutting direction, the deformation was dominated by deformation on the n-plane but rhombohedral twinning was observed as well. In this cutting direction, the fracture observed was initiated along the rhombohedral cleavage plane. In the case of the C270 cutting direction, the deformation was mostly driven by basal and rhombohedral twinning, with the rhombohedral twinning being the more dominant mechanism. As a result, the deformation extended deeper in to the subsurface region. The fracture observed in the cutting direction was along the basal cleavage plane. In the case of the R90 cutting direction, basal, prismatic, and rhombohedral deformations were observed. As a result of the activation of multiple systems with very different directions of activation, the slips/twinning likely interacted and caused a crack to initiate resulting in a low value of CDC. In this cutting direction, the cleavage was initiated along the prismatic M-plane.

Comparing the MD simulation results with the prediction of subsurface damage through Raman spectroscopy (section 4.2), the trends observed in the MD simulations mostly matched the experiments. Except for the case of the C180 and C270 cutting directions where the trend was reversed which needs to be investigated further.

Figure 4.11 shows the temporal evolution of deformation during the MD simulation on C- and R-plane of sapphire in the 180° cutting direction. In the case of the C180 simulation, activation of basal deformation mechanisms can be clearly seen in front of the tool. The interesting aspect of the basal activations is that it extends well ahead of the tool, almost to the end of

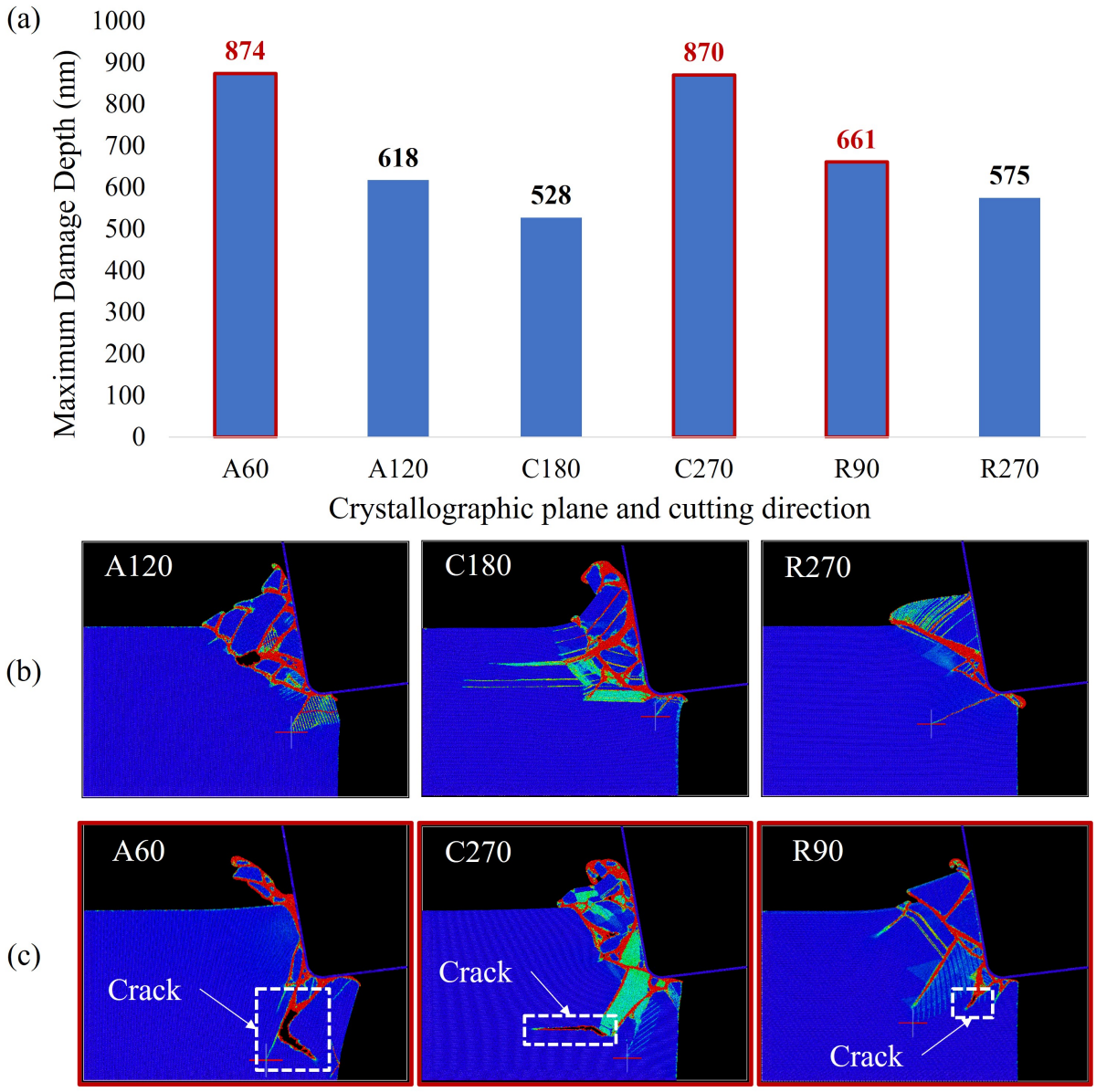

Figure 4.10: (a) Maximum damage depth for different cutting directions in sapphire from MD simulations; (b) MD simulation for cutting directions where no crack was observed beneath the tool; (c) MD simulation for cutting directions where a crack was observed beneath the tool.

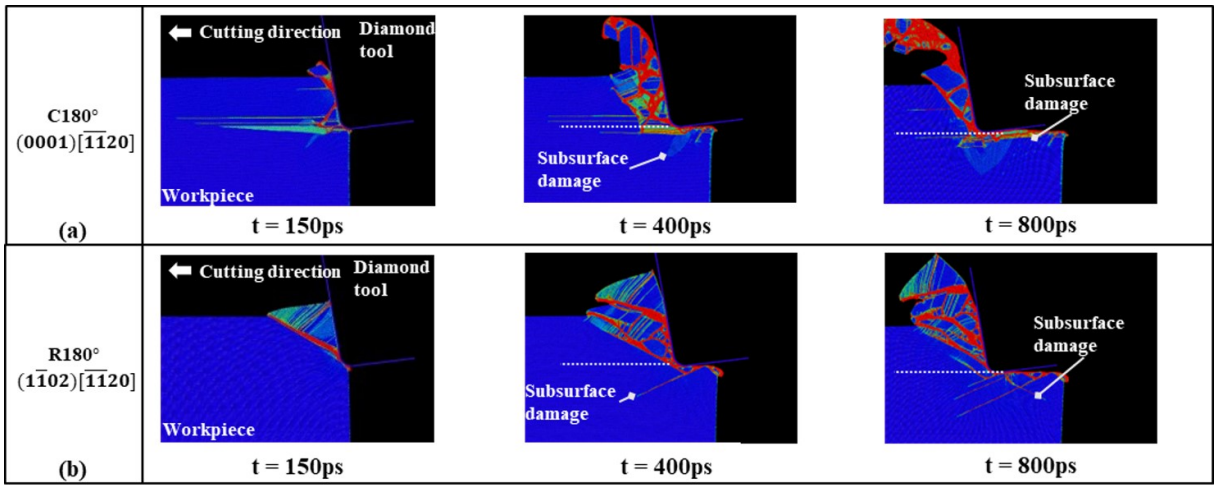

Figure 4.11: MD simulation of machining in the 180° cutting direction on the (a) C-plane and (b) R-plane of sapphire showing the temporal evolution of deformation.

the simulation boundary. In addition to this, a few rhombohedral mechanisms were observed but were seen to extend to a limited depth into the subsurface. In the case of the R-plane, deformations on different rhombohedral planes were observed which extended deeper into the subsurface compared to the C-plane.

Overall, the MD simulation results validated the hypothesis about the anisotropic nature of subsurface damage as well as the activation of different slip and fracture systems leading to varying amounts of deformed material remaining in the workpiece, contributing to the subsurface damage. In the next section, TEM evaluation is presented to better understand the deformations observed in the subsurface post machining and to explain the discrepancy observed in the case of subsurface damage prediction on the C-plane of sapphire.

4.4 Transmission Electron Microscopy (TEM) Observations

This section deals with the different TEM observations of subsurface damage carried out in this work. As this was one of the more challenging tasks carried out in this research, the first part of this section is dedicated to sample preparation, which took a long time to figure out. As most of the work was concerned with observing subsurface damage at the nanometer scale, FIB milling had to be used to prepare TEM samples from selected regions on the workpiece. Although other techniques such as cleaving or grinding and polishing can be used for TEM sample preparation, the micrometer sized areas of interest on the machined sapphire workpieces limited the choice

to FIB milling. The sample preparation process involved cutting out thin lamella from the selected regions using a FIB, separating the lamella from the sapphire substrate, attaching it to a TEM grid, and finally thinning the lamella until it became electron transparent. The different challenges encountered during sample preparation are first described, followed by the techniques used to resolve these problems. Once the sample preparation was figured out, a number of samples were created from the C- and R-planes of sapphire which were analyzed using the TEM and are then discussed in the subsequent subsections. Following this, the section contains comparisons between TEM observations and MD simulation results and a comparison between the TEM observations and prediction of material deformation using the P- and F-parameters introduced in section 2.2.

4.4.1 Sample Preparation

All the TEM samples used in this study were fabricated using an SEM with dual beam capabilities (Zeiss Auriga, Carl Zeiss Microscopy GmbH, Germany) which uses a gallium ion source to remove or deposit material. TEM sample preparation using FIB is a topic in itself which involves many steps of rotating and translating the workpiece while manipulating the ion beam and other peripheral equipment and are not be covered here. Rather, the different challenges faced during TEM sample preparation from an uneven, machined surface of a single crystal are introduced. These issues are illustrated using the images in Figure 4.12.

As seen in Figure 4.12(a), the machined surface of sapphire, especially in the brittle regions can have a significant amount of roughness. As a result of this, when the protective platinum and carbon caps are deposited, they follow the topography of the surface and are deposited unevenly across the surface. This affects the subsequent FIB milling process and is explained later. As sapphire is harder to ion mill compared to other ceramics like silicon, higher milling currents or longer milling times need to be used (especially in the earlier stages where lot of material needs to be removed). The disadvantage of using higher milling currents is the reduction in control over the milling area due to beam spreading and introduction of subsurface damage due to ion implantation. On the contrary, higher milling times while using lower beam currents have monetary implications and can also cause subsurface damage due to prolonged exposure to the ion beam. Although a compromise is often found, the milling still takes about 8-15 minutes

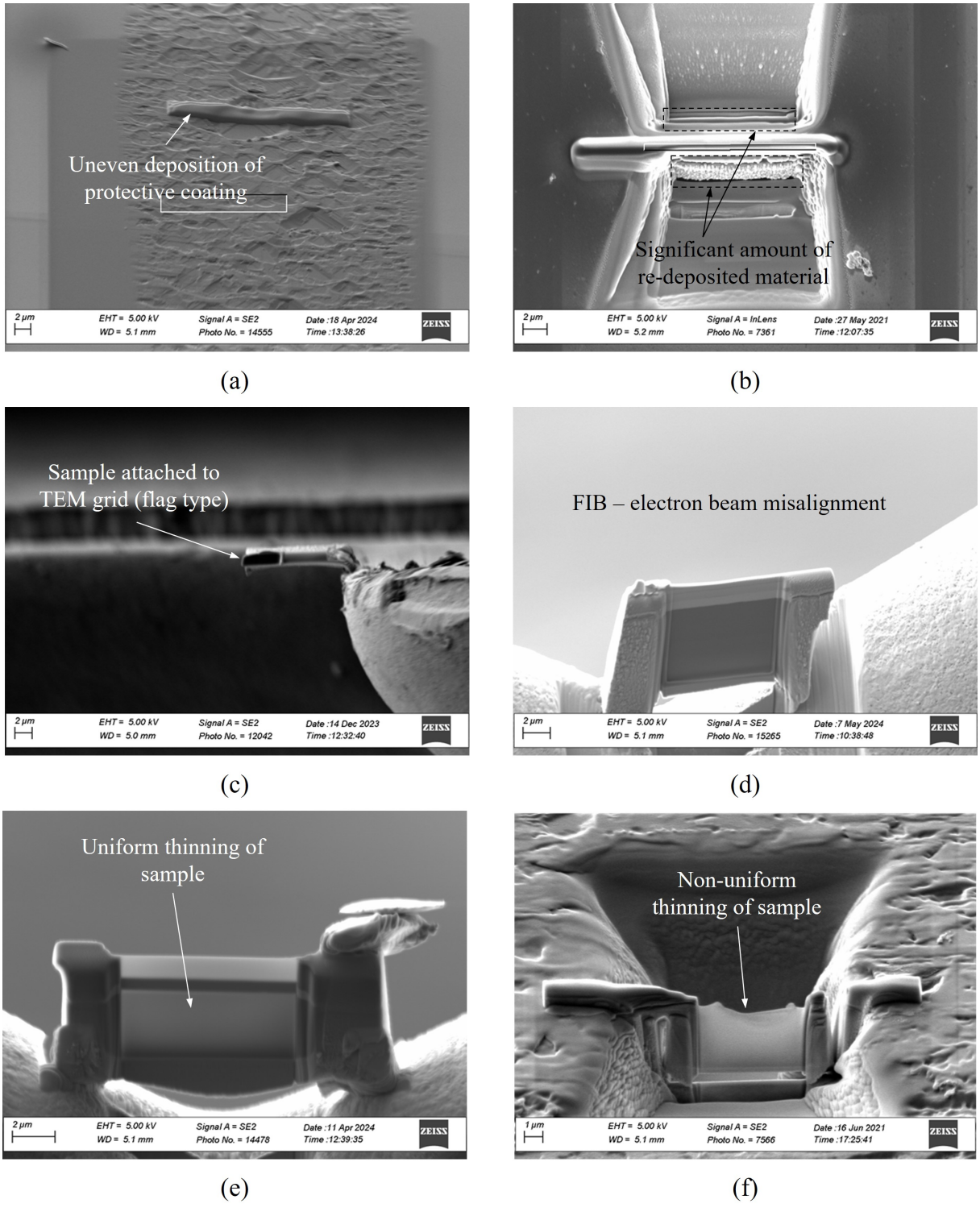

Figure 4.12: Different challenges faced during TEM sample preparation using FIB. (a) Uneven deposition of protective coatings; (b) re-deposition; (c) attachment to TEM grid; (d) beam misalignment; (e) ideal TEM lamella; (f) TEM lamella showing non-uniform thinning.

compared to 3-5 minutes often encountered while milling silicon. As a result of this added time, another issue that props up is material re-deposition caused by vaporized ions re-depositing on to the sample surface around the beam skirt. This is illustrated in Figure 4.12(b). This re-deposited material makes it difficult to judge the TEM lamella thickness and decipher when the lamella is separated from the substrate during the lift-out procedure.

The next challenge faced was during the step of attaching the lamella to TEM grid. For this purpose, copper PELCO® FIB lift-out grid with 2 posts (Ted Pella Inc., U.S.A.) were used. The main challenge during this step was ensuring a secure attachment to the TEM grid while also ensuring relative straightness of the lamella. As the lamella is held to the lift-out probe by a small deposition of platinum at this stage, it is extremely fragile and can get dislodged very easily, even with a small bump. The fragile attachment of the lamella on the TEM grid in flag style is shown in 4.12(c). Once the lamella was attached, the next challenge that had to be solved was with respect to the FIB-electron beam alignment. Due this is style of FIB instrument using apertures to control the milling/imaging currents, small amounts of misalignment during aperture switching is inevitable due to the mechanical linkages used in the aperture switching mechanism. This problem is a major concern during the final thinning steps where care must be taken to select the milling regions correctly. An example of the misalignment is shown in Figure 4.12(d). If the alignment was perfect, the SEM image would not be showing the thickness of the lamella.

Finally, Figures 4.12(e) and (f) compare the effect of surface roughness on the final thinning process as introduced previously. Like the deposition, having a rough or machined surface to begin with can cause uneven milling across the length of the lamella and can cause parts of the machined region to be milled away while trying to make the lamella electron transparent.

All of these challenges were overcome by trial and error and carefully varying and recording different FIB milling parameters such as milling current, number of layers, angle of slope, adjustments to the sample tilt, etc. Subsequently, the steps followed for a successful sample preparation are discussed in the following paragraphs. This process is divided into 2 steps - the first set deals with processes followed until lift-out and the second set deals with steps followed after lift-out. The first set of steps is shown in Figure 4.13.

The first step in preparing a successful TEM lamella from a machined sapphire workpiece

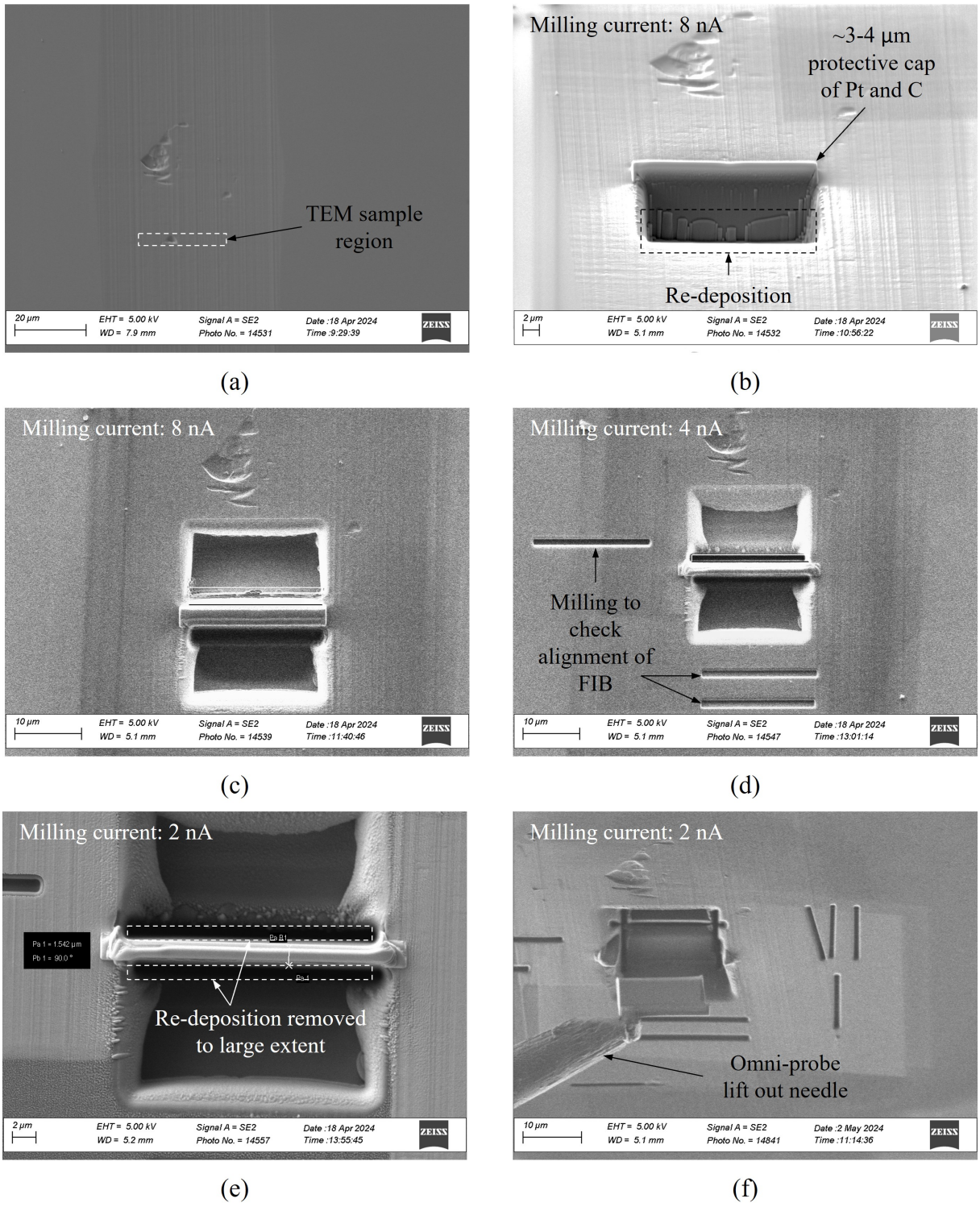

Figure 4.13: Steps involved in preparing a TEM lamella from a machined sapphire sample.

involves selecting the region from which it needs to be milled Figure 4.13(a) and depositing about 3-4 μm of platinum and carbon as protective caps. Generally, the smoother the surface, better is the quality of the lamella, but through careful experimentation, suitable FIB milling process parameters were determined and the surface roughness is no longer a major issue. Next, for the large material removal step, a current of 8 nA was used to make a trench around the sample (Figure 4.13(b)). Under these conditions, the beam spread is limited and the milling can be completed in a reasonable amount of time. Under these conditions however, significant amount of re-deposition occurs, and as a result, the lamella thickness varies with the depth. At this stage, it is advised to move the milling box away from the sample by about 1-2 μm. Once this was completed, a rectangular box was milled at 8 nA current to ensure that the walls of the lamella are more even (Figure 4.13(c). Next, a lower currents of 4 nA and 2 nA were chosen to clean up the re-deposition and a rectangular box was milled (Figures 4.13(d) and (e), respectively). At these lower currents, the milling box size was reduced to minimize the milling time and also thin the sample slightly. It should also be noted that prior to milling, the alignment of the ion beam needs to be verified by milling slots in an inconsequential region of the sample and checking the deviation from the specified rectangular box. Further, at lower currents, the amount of re-deposition is significantly reduced. Having cleaned up the walls of the lamella, it is also easier to spot the J-cut performed to separate the lamella from the substrate. But prior to that, the Omni-probe lift out needle was inserted and attached to the lamella (Figure 4.13(f)) and the lift-out was completed.

Once the TEM lamella was lifted out, the TEM grid had to be prepared for the sample attachment. Generally, different types of attachment such as side mount (flag), or top mount are possible. It was found that top mounting at the bottom of the "M" shaped structure on the TEM grid post was most suitable. The reason for this selection is that the side mount has a much smaller attachment area and being on the side of the post, can get knocked off inadvertently. To ensure an even attachment to the grid, small slots were milled in the grid to accommodate the lamella (Figure 4.14(a)). It must be noted that in this configuration, Energy-Dispersive X-ray Spectroscopy (EDS) analysis can be hard to perform as the detector may not be able to see the sample clearly. Upon successful attachment of the lamella to the TEM grid, the milling current was further reduced to 300 pA and the lamella was thinned (Figure 4.14(b)) followed by

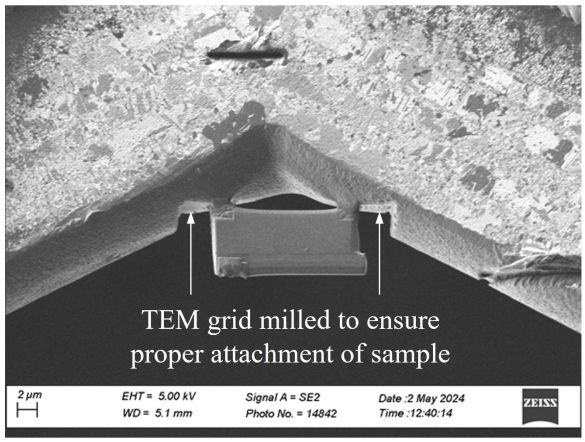

(a)

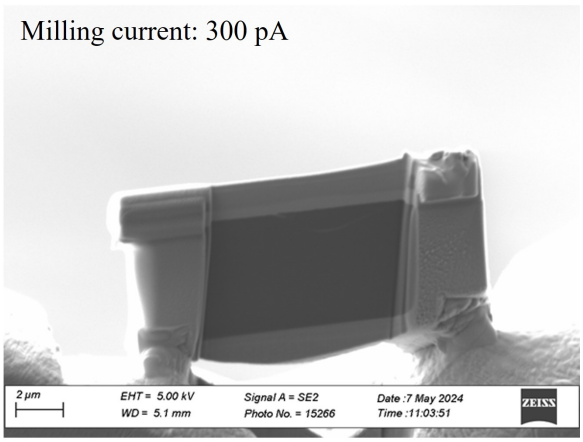

(b)

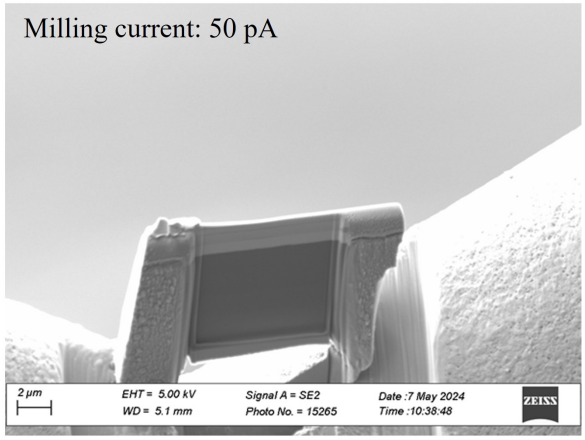

(c)

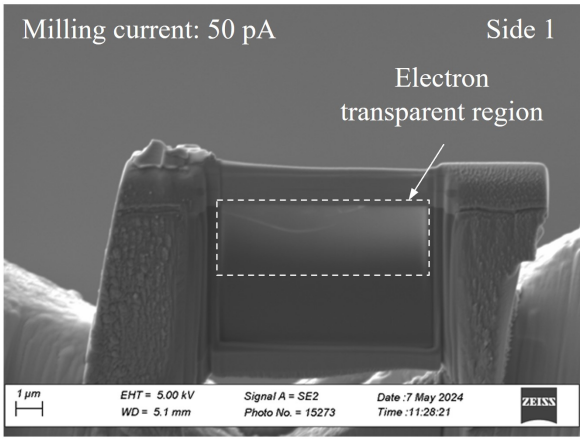

(d)

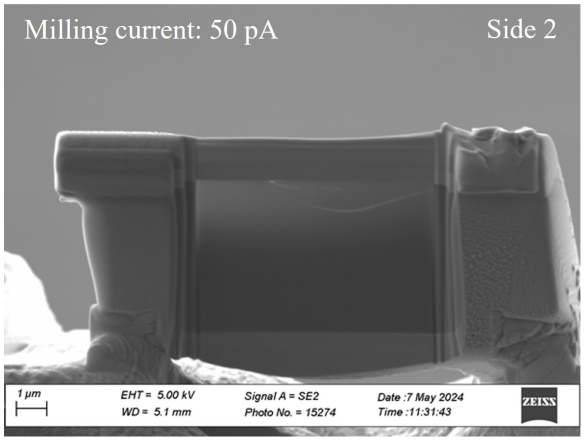

(e)

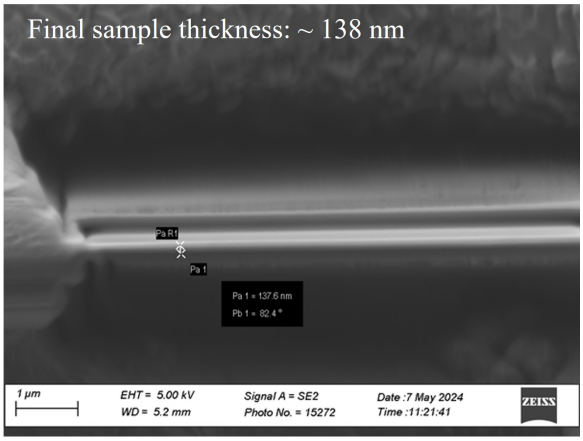

(f)

Figure 4.14: Steps involved in attaching the lamella to a TEM grid and thinning it.

a further reduction to 50 pA (Figure 4.14(c)). Upon completion of the milling on one side and lamella thickness about 600 nm, the process was repeated on the other side of the lamella. For the final thinning, 50 pA milling current was used but at a lower voltage of 2 kV. This process was important to prevent introducing any defects or amorphization to the lamella. The milling process was stopped as soon as the lamella started become electron transparent (Figure 4.14(d) and (e)) and had a thickness on the order of about 100 - 160 nm (Figure 4.14(f)). Next, the TEM grid was carefully removed and placed in an air-tight container lined with lint-free delicate task wipes for storage. Any subsequent handling of the TEM grid was carried out using vacuum tweezers. In the next subsections, analysis of different TEM samples is discussed. The TEM observations are divided into the two sets. The first set compares the subsurface damage on the C- and R-planes of sapphire with the samples being fabricated perpendicular to the cutting direction. The second set of results compares two different cutting directions on the C-plane of sapphire where the samples were fabricated parallel to the cutting direction. While the first set of experiments provides insight into the different cutting planes of sapphire and information about how the defects spread laterally during machining, the second set of experiments provides information about deformation in front of the tool and how the deformation evolves as the tool removes material in the workpiece.

4.4.2 Comparison of Subsurface Damage Between Crystallographic Planes Through TEM

The results presented in this section have been published in the proceedings of the 20th International Conference on Precision Engineering (ICPE 2024), 23-27 October, 2024 and is being prepared for journal publication [69].

In the first set of experiments, one cutting direction from the C- and R-planes of sapphire were chosen for TEM observation and analysis. In order to observe atomic scale defects, High Resolution Transmission Electron Microscopy (HRTEM) images are necessary. However, to capture these images, the sample needs to be oriented along a zone axis - a condition where the incident electron beam is parallel to a crystallographic direction contained by at least 2 unique crystallographic planes. Due to the low symmetricity of sapphire, there are a limited number of zone axis available for HRTEM imaging and analysis. As a result, the samples in this study

were prepared to be viewed from the $[\overline{1}\overline{1}20]$ zone axis.

Further, from the residual stress analysis presented in section 3.2.2, the C- and R-planes showed a large differences in the residual stress magnitude most probably resulting from the varying amounts of plastic deformation remaining in the subsurface after machining. Subsequently the samples were made from the 180° cutting directions on both the C- and R-plane of sapphire - $[\overline{1}\overline{1}20]$. The regions from which the TEM samples were created is shown in Figure 4.15. The sample regions were selected in such a way to overlap a few cracks to understand the extent of subsurface damage, as well as some of the ductile regions around the crack to study the surrounding plastic deformation. Subsequently, all the TEM images were captured using a FEI Tecnai TF-30 300 kV TEM (FEI Technologies Inc, USA).

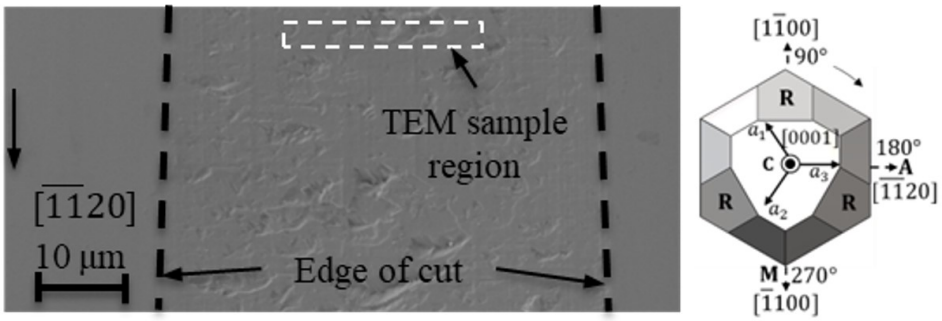

(a)

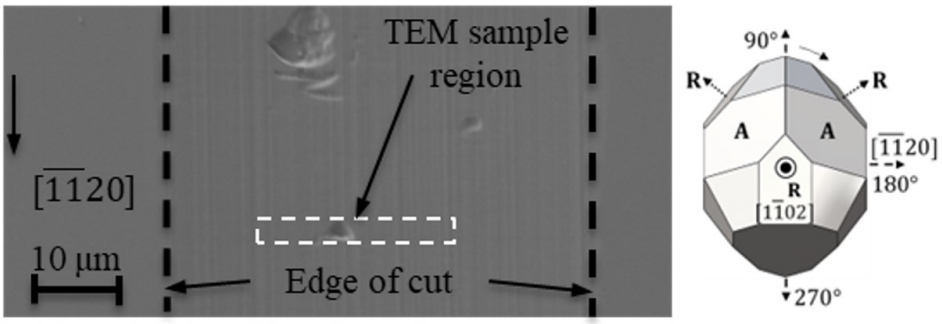

(b)

Figure 4.15: (a) SEM image of brittle region on C-plane of sapphire showing the TEM sample region; (b) SEM image of brittle region on R-plane of sapphire showing the TEM sample region [69].

Figure 4.16 shows the set of TEM images captured from a cross section of the machined sample on C-plane of sapphire. In this sample, 3 regions were selected for analysis. The first region of interest was a reference image from the bulk sample, several micrometers below the

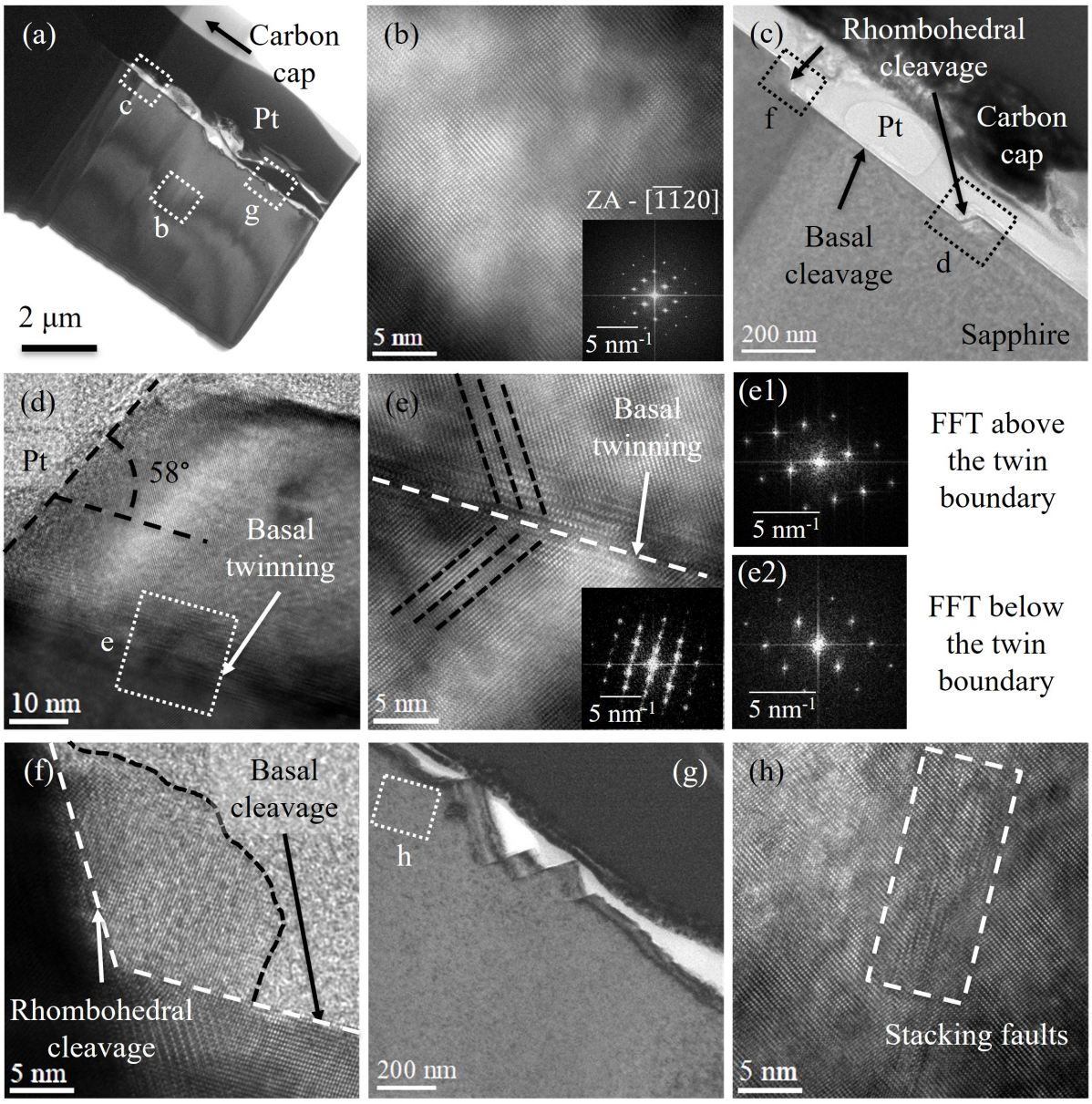

Figure 4.16: (a) Bright field image of the TEM sample from 180° cutting direction on the C-plane; (b) HRTEM and FFT of the bulk sample (region b); (c) Region showing basal and rhombohedral cleavage (region c); (d) HRTEM image from a portion of (c); (e) HRTEM and FFT of a basal twin; (f) HRTEM image of intersection between basal and rhombohedral cleavage; (g) TEM image showing pulled out crack formed by intersection of multiple cleavage systems (region g); (h) HRTEM image of region in (g) showing stacking faults [69].

machined surface (region b), the second region exhibited distinct cleavage fractures on the machined surface (region c), and the third region, which showed a more complex fractured surface (region g). In Figure 4.16(b), HRTEM image of the bulk sample, no significant damage to the crystal lattice was observed and by taking a Fast Fourier Transform (FFT) of the image and analyzing the resulting diffraction pattern, it was confirmed that the zone axis for observation was $[\overline{1}\overline{1}20]$.

Looking at region c, it was observed that two different cleavage facets had formed – parallel to the basal plane and rhombohedral planes (Figure 4.16(c)). The orientation of the cleavage faces was confirmed by measuring the angle with respect to the workpiece surface and comparing it to the crystal structure of sapphire (Figure 4.16(d)). Looking closely at the image, basal twinning was observed in the region adjacent to the cleaved region. This was confirmed through HRTEM images and taking FFT from the regions above and below the twin boundary and looking for a mirror symmetry in the diffraction pattern (Figure 4.16(e)).

Looking at the intersection of the basal and rhombohedral cleavages (Figure 4.16(f)), it was observed that the basal cleavage produced nearly atomically flat surfaces whereas on the rhombohedral cleaved surface, there were small regions of crystalline material that had not cleanly separated from the surface indicating a mix of rhombohedral cleavage and plastic deformation (region marked by the black dashed line in Figure 4.16(f)).

In literature, it has been shown that twin boundaries can act as sites for crack initiation and it is possible that the basal twin was formed first and as the stress in the region increased, it was relieved by crack initiation. The basal twinning was about 50 nm below the machined surface and acted as a barrier to prevent further plastic deformation or fracture from extending into the subsurface. Looking at region g (Figure 4.16(g)), multiple different cleavage faces were observed (mostly basal and rhombohedral cleavages). The subsurface in this region did not have many distinct features other than a few stacking faults at a depth of about 150 nm from the machined surface.

Figure 4.17 shows the TEM images captured from the R-plane sample. Unlike the C-plane sample, clear plastic deformation and large cracks were observed in the R-plane sample. In this sample, 4 different regions were selected for further investigation. The first region was for reference several micrometers below the machined surface (region b), the second region was from

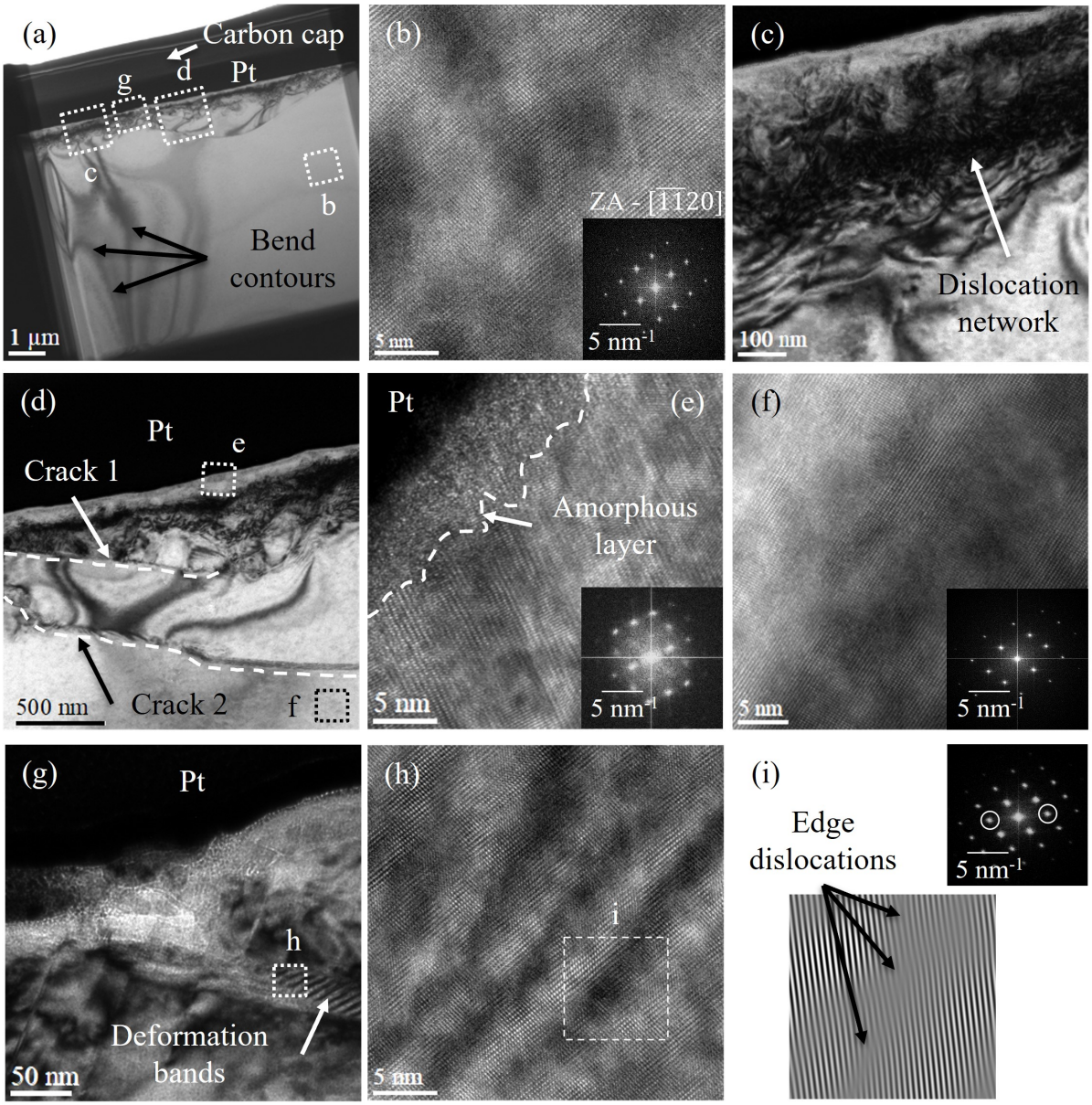

Figure 4.17: (a) Bright field image of the TEM sample from the 180° cutting direction on the R-plane; (b) HRTEM image and FFT of the bulk sample (region b); (c) Bright field image of the region adjacent to the crack (region c); (d) Bright field image of the cracked region (region d); (e) HRTEM and FFT of the cracked region close to the surface; (f) Subsurface HRTEM and FFT of the region below the crack; (g) Bright field image of region where the crack reaches the machined surface (region g); (h) HRTEM of deformation bands observed in (g); (i) FFT of (h) and selection of diffractions spots for masking and subsequent FFT from highlighted region in (h) [69].

the ductile portion of the sample (region c), the third region was from the cracked portion of the sample (region d), and the final region was from the location where a crack intersected with the sample surface (region g). Similar to the C-plane sample, the zone axis was confirmed to be $[\overline{1}\overline{1}20]$ by analyzing the FFT from region b (Figure 4.17(b)).

Looking at the region from the ductile portion of the machined surface (Figure 4.17(c)), the bright field TEM images provide higher contrast between regions with dislocations and those without. The image showed that large dislocation networks extending to about 700 nm below the machined surface were present. Due to the presence of a large number of likely entangled dislocations, it is difficult to determine exactly which slip system the dislocations belong to, and it is possible that dislocations from different slip systems might have been activated.

Focusing on the region with the crack (Figure 4.17(d)), it was observed that two cracks were formed in the subsurface. The first crack extended to about 500 nm below the machined surface and the second crack extended deeper to about 1 μm below the machined surface. Unlike the cleavage type fractures on the C-plane surface, the subsurface cracks in the R-plane sample did not have any particular crystallographic directionality and likely originated from regions of stress build up due to dislocation entanglement and plastic deformation and followed the path of least resistance. Examining this region further, it was observed that an amorphous layer of about 5-10 nm had formed just below the machined surface (Figure 4.17(e)). This is likely the case across the entire machined surface of the sample as reported in other machining studies in sapphire [122].

However, a discernible amorphous layer was not observed in the C-plane sample. Below the amorphous layer, the material was observed to have undergone considerable amount of plastic deformation as indicated by the fuzzy diffraction spots in the FFT image. Moving to the region below the second crack, the crystal structure seemed to be unaffected by the plastic deformation (Figure 4.17(f)) as indicated by the FFT. Like the basal twinning in the case of the C-plane, the second crack seemed to prevent any deformation from extending deeper into the subsurface. Looking at the region where the first crack meets the surface (Figure 4.17(g)), severe plastic deformation was observed around the initiation point. In this region, distinct deformation bands were observed adjacent to the crack.

To determine the composition of the deformation bands, HRTEM images were captured

(Figure 4.17(h)). As the crystal structure did not show any mirror symmetries, twinning could be ruled out. However, slips and dislocations are much harder to detect in images with large fields of view. To overcome this challenge, FFT was applied to the image and only one family of diffracted planes was selected to apply a masking filter (Figure 4.17(i)) and an FFT operation was applied on the original image. Based on the analysis, the FFT image shows edge dislocations to be present in the same region as the deformation bands whereas the regions surrounding the bands seemed to have a regular, defect free crystal structure. Identifying the exact type of dislocations would require further analysis and is reserved for future work.

In summary, the trends observed in the TEM observations were similar to that seen in the MD simulations (section 4.3) where the R-plane of sapphire showed deeper subsurface damage depth compared to the C-plane for the 180° cutting direction. In the next part of the analysis in this study, the analytical model presented in section 2.2 was used to predict the most likely slip/twinning and fracture mechanisms that would get activated using the resultant force values as an input to the model. The results of the calculations are shown in Figures 4.18 and 4.19.

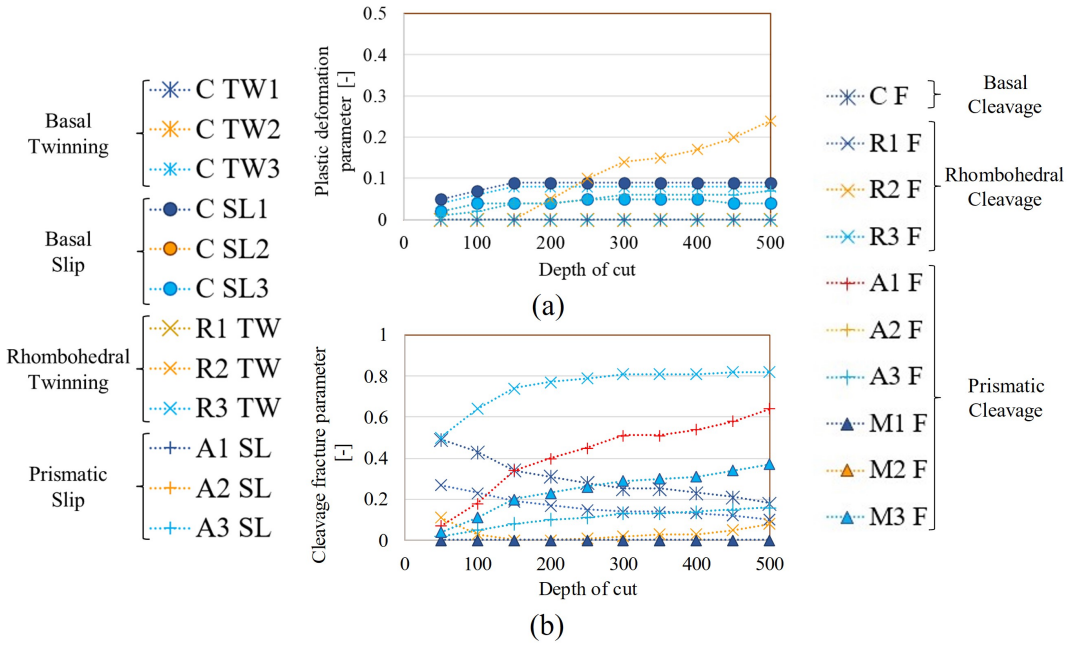

Figure 4.18: (a) Calculation of the plastic deformation parameter and (b) Fracture cleavage parameter on the 180° cutting direction of C-plane [69].

Starting with the plastic deformation on the C-plane (Figure 4.18(a)), it was observed that at low depths of cut, basal slip and basal twinning (C TW3) was predicted to be the dominant

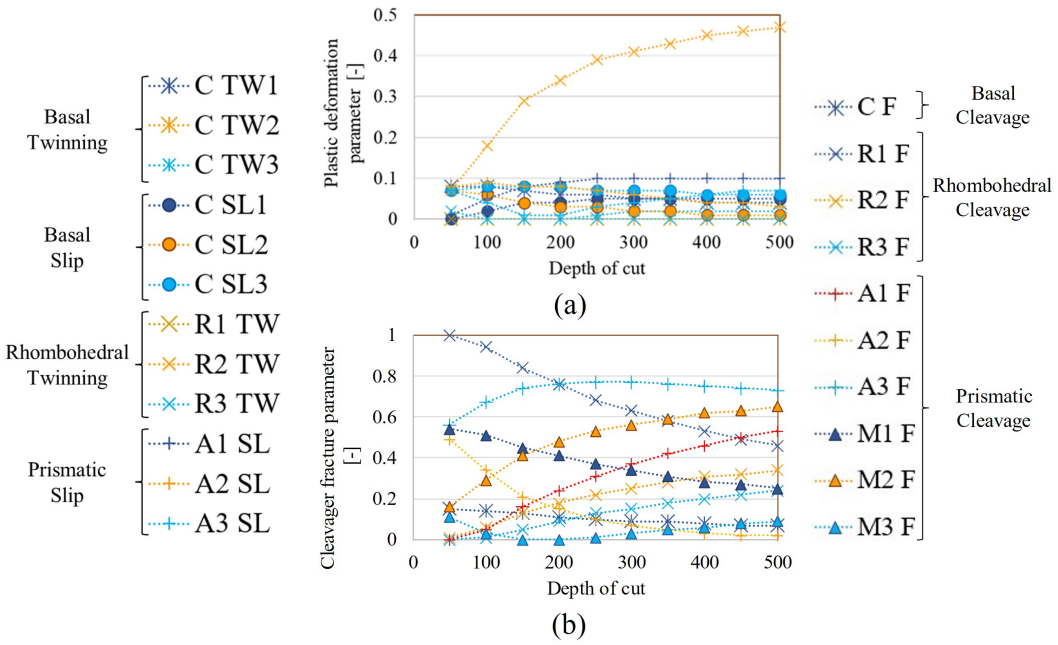

Figure 4.19: (a) Calculation of the plastic deformation parameter and (b) Fracture cleavage parameter on the 180° cutting direction of R-plane [69].

mechanism. As the depth of cut increased, rhombohedral twinning (R2 TW) became dominant, but the second most likely systems were basal. In terms of the cleavage fracture parameter, many systems seemed likely, particularly rhombohedral (R3 F) followed by the prismatic systems (Figure 4.18(b)). Comparing the analytical calculations with the TEM results, it is likely that the basal twining activated at lower depths of cut extend well ahead of the tool and influence further material deformation by preventing other mechanisms from extending into the subsurface. Extension of basal twinning ahead of the tool for this cutting direction in sapphire has been observed in MD simulation results [70] (also see Figure 4.10). As a result, most of the plastic deformation is concentrated close to the surface and removed by chip formation. Comparing the fractures on the surface, rhombohedral and other cleavages were clearly visible in the TEM images (Figure 4.16(c) and Figure 4.16(g)).

Investigating the deformation in the R-plane of sapphire, right from low depths of cut, rhombohedral twinning (R2 TW) was the dominant mechanism followed by basal and prismatic systems that had a similar likelihood and this trend continued at higher depths of cut as well (Figure 4.18(a)). Looking at the fracture cleavage parameter, multiple systems had a high likelihood with prismatic systems (A3 F, M2 F, A1 F) dominating at higher depths of cut

(Figure 4.19(b)). In terms of plastic deformation, it was difficult to determine the exact plastic deformation systems from the TEM results as a large number of dislocation networks were observed (Figure 4.17(c)). Although it is known that R2 TW mechanism forms an angle of 42° with the machined surface and causes plastic deformation deeper in the subsurface [24]. Contrary to the C-plane, while comparing fracture, clear cleavage facets were not visible but subsurface fracture activation as a result of likely dislocation entanglement was observed.

4.4.3 Comparison of Subsurface Damage Between Cutting Directions on C-plane Through TEM

In the second set of TEM analysis performed, two cutting directions on the C-plane of sapphire were selected - 180° and 270°. However, in this case, the TEM lamella were prepared parallel to the cutting direction. The main reason for selecting these two cutting directions was to resolve the discrepancy observed between the Raman peak width measurements and the MD simulations where subsurface damage depth measurements did not show the same trend. Additionally, in these two cutting directions, it would be possible to capture HRTEM images due to the alignment with the $[\bar{1}100]$ and $[\bar{1}\bar{1}20]$ zone axis for the 180° and 270° samples, respectively. In these experiments, the machining process parameters for sample preparation were as described in section 2.3, however, the tool path was slightly modified. Upon reaching a depth of 500 nm, the tool was lifted up vertically. The reason for choosing this type of tool path was to better understand the deformation that occurs in front of the tool, especially after having seen the MD simulation results.

Figure 4.20 shows the slightly modified tool path, machined surface, and sample area used for the TEM analysis along the 180° cutting direction on C-plane of sapphire. Figure 4.21 shows a low magnification bright field TEM image of the sample. In the low magnification image, two subsurface cracks were visible along with some deformation in the end of cut region where the tool was lifted up from the workpiece. From the low magnification image, it was evident that the crack extended to about 1.3 μm below the machined surface. It was of interest to observe these subsurface cracks in more detail, as well as the deformation in the region ahead of the tool. The region in front of the tool is of particular interest to researchers to better understand the effect of the tool edge radius on deformation and the stress field developed at the tool-workpiece

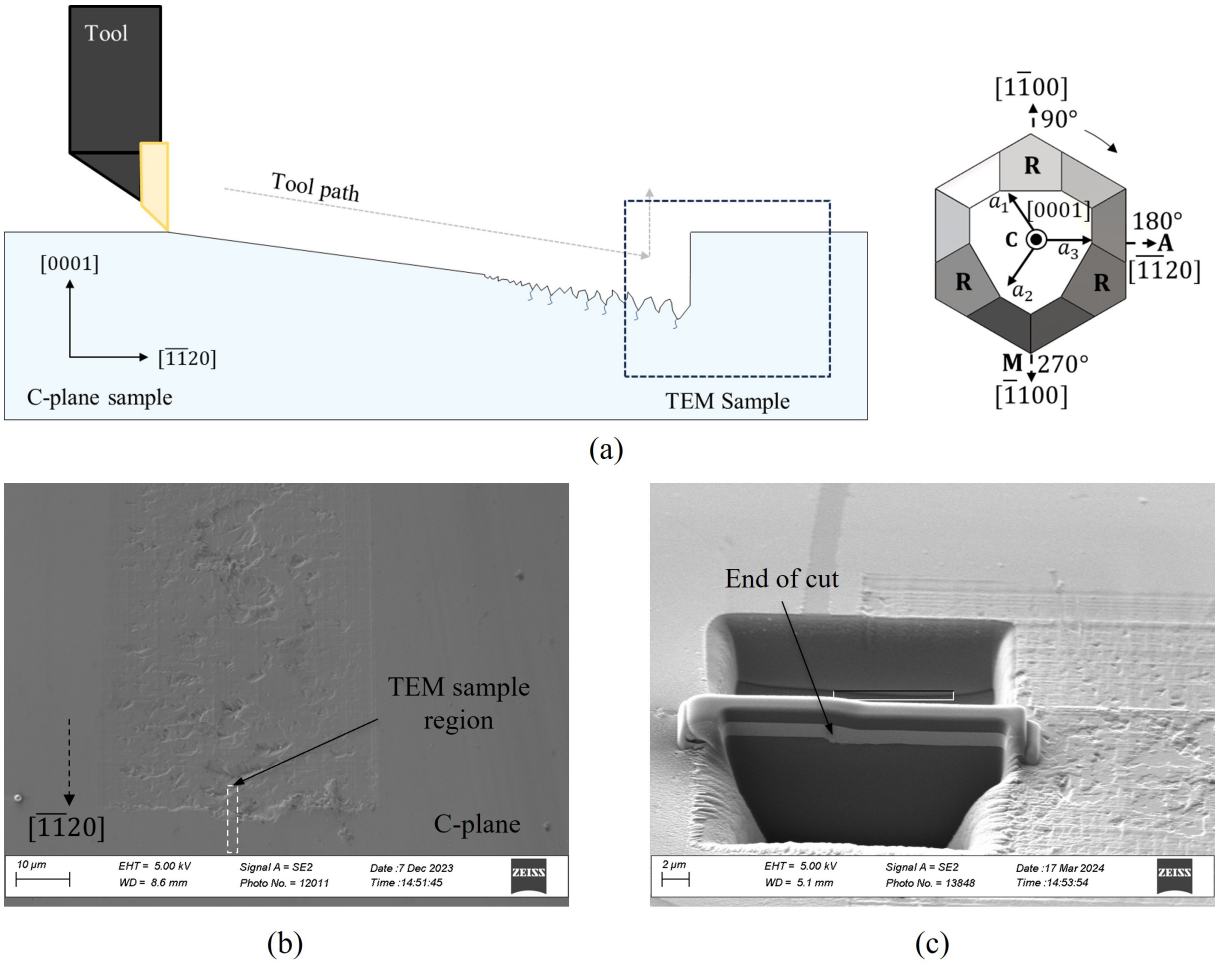

Figure 4.20: (a) Schematic of plunge cutting experiment and TEM sample area along the 180° cutting direction on C-plane of sapphire; (b) SEM image showing the TEM sample region; (c) Sample preparation using FIB milling showing the end of the cut region.

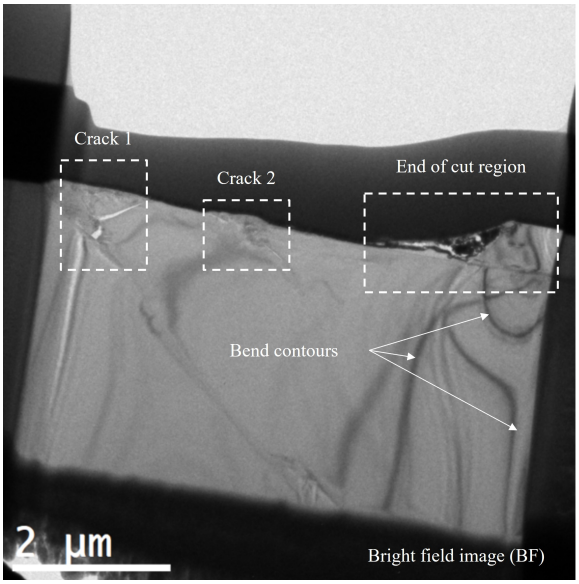

Figure 4.21: Bright field TEM image of the entire lamella showing the different features and regions of interest for the C-plane 180° cutting direction sample.

interface. As the cutting tools can have various geometries, the stress-field in front of the tool can change significantly and thereby affect the deformation in the workpiece.

Figure 4.22 shows magnified (a), (c), and HRTEM (b), (d) images of the two cracks observed in the subsurface region of the 180° cutting on C-plane of sapphire. It was observed that crack 1 (Figure 4.22(a) extended to about 1.3 μm below the machined surface whereas crack 2 extended to a depth of about 800 nm below the machined surface. Further, it was observed that crack 1 extended up to the surface and had a smooth cleaved surface (probably rhombohedral fracture) - Figure 4.22(b). On the other end of crack 1, significant plastic deformation and crack branching was visible. Investigating the FFT patterns on either side of the crack, it was observed that the material was still highly ordered and single crystalline in nature. On the other hand, crack 2 was much smaller compared to crack 1 and seemed to originate from significant amount of plastic deformation just below the machined surface (Figure 4.22(c)). The material on either side of the crack still appeared to be crystalline in nature but there was rotation of about 6° in the crystal lattice (Figures 4.22(d1 and d2)). At this moment, it is not clear if the lattice rotation was caused by the plastic deformation surrounding the crack or due to the separation of material during crack initiation and needs to be investigated further.

Figure 4.23 shows the magnified images of the end of cut region. In Figure 4.23(b), two

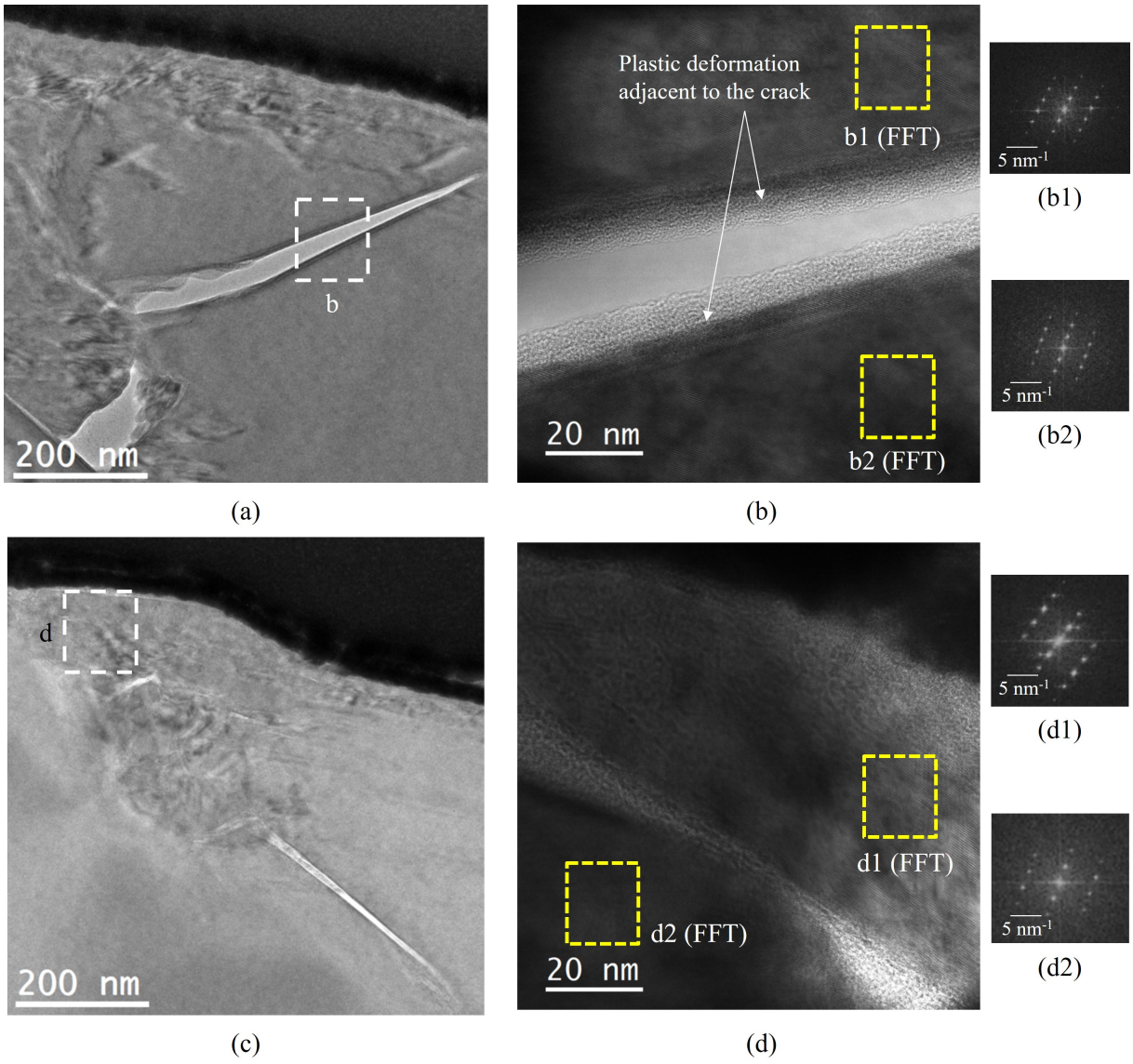

Figure 4.22: Magnified images of cracks 1 and 2 observed in the subsurface region of the machined surface along 180° cutting direction on C-plane and FFT analysis carried out around the crack.

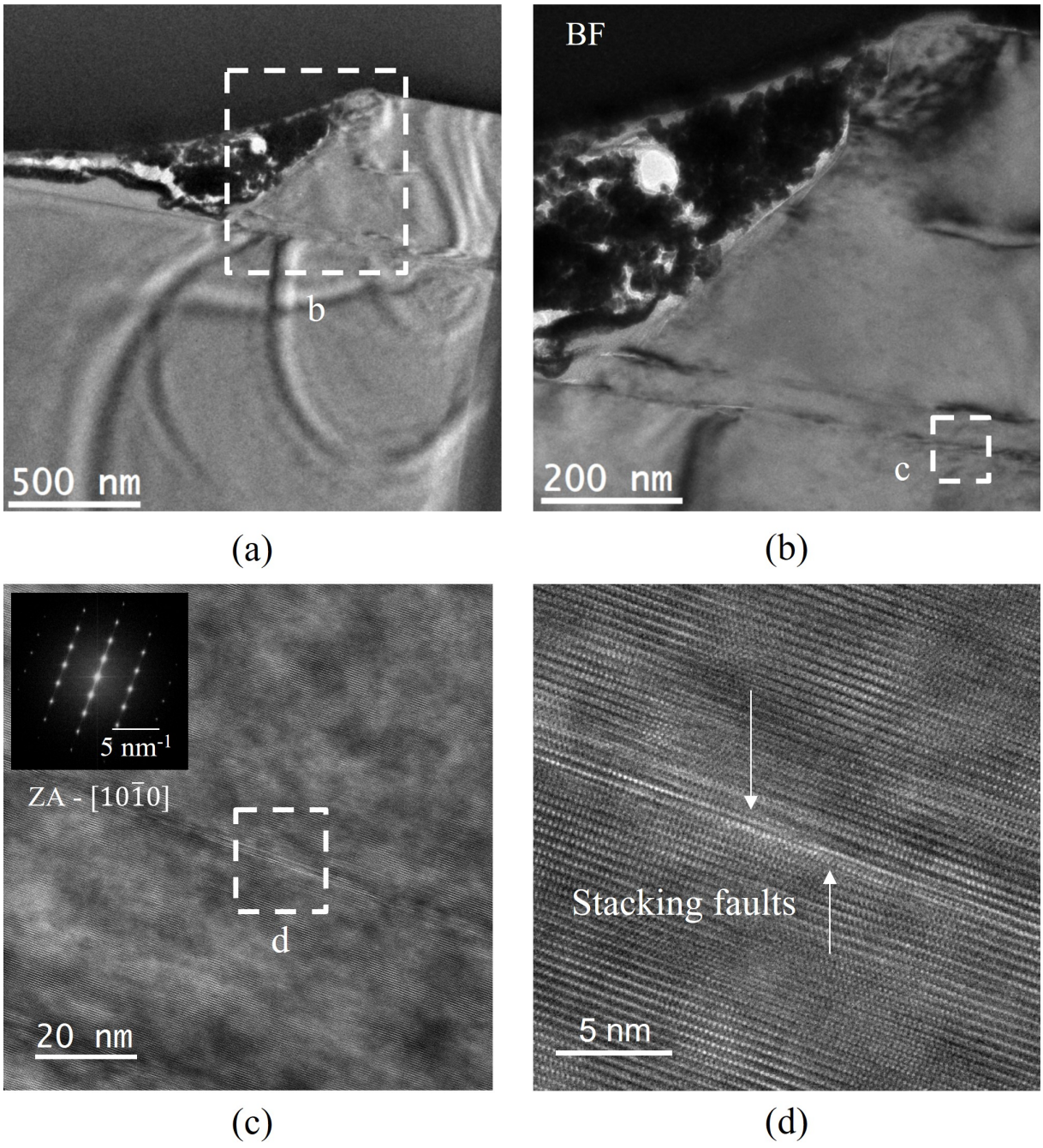

Figure 4.23: (a) and (b) Magnified images of the end of cut region along the 180° cutting direction on C-plane; (c) HRTEM image of deformation band observed in front of the tool; (c) Magnified HRTEM image of a region from (c) showing stacking faults.

deformation bands emanating from the cutting edge of the tool are clearly visible and are parallel to the basal plane of sapphire as well as to each other. Although one of the dominant deformation mechanisms in this cutting direction is basal twinning, a clear twin boundary was not observed around the deformation bands in the HRTEM images (Figures 4.23(c) and (d)). Rather, a lot of stacking faults were visible in the regions close to the bands. It is possible that the twin boundary might not be visible in this particular zone axis or orientation of the sample. The interesting takeaway from this image is that the basal deformation extends well ahead of the tool as observed in the MD simulations (Figure 4.11). Further, this might be an interesting approach to measure the cutting edge radius of diamond tools used in UPM.

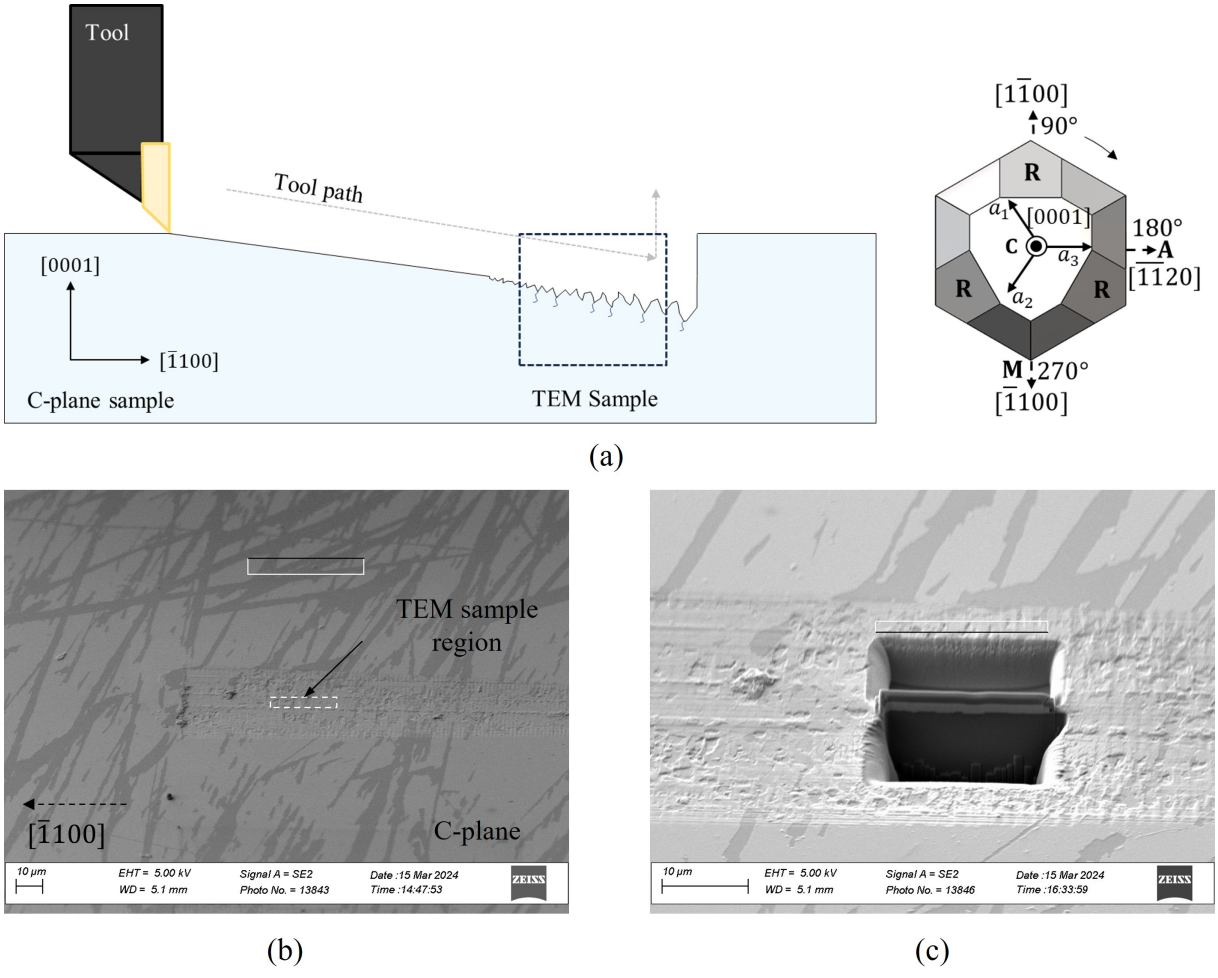

Figure 4.24: (a) Schematic of plunge cutting experiment and TEM sample area along the 270° cutting direction on C-plane of sapphire; (b) SEM image showing the TEM sample region; (c) Sample preparation using FIB milling showing the end of the cut region.

Figure 4.24 shows the slightly modified tool path, machined surface, and sample area used

for the TEM analysis along the 270° cutting direction on C-plane of sapphire. In this sample, the TEM lamella was FIB milled from a region that was not the end of the cut to understand subsurface deformation in regions that the tool has already passed over. Figure 4.25 shows a low magnification bright field TEM image of the sample. Unlike the 180° sample, this sample did not show any cracks in the subsurface and the plastic deformation was concentrated very close to the machined surface. It must be noted that since the TEM sample examines a very small region of the machined surface, the presence of subsurface cracks in other regions should not be ruled out. Other than the deformation parallel to the basal plane, there were no other features in this sample that stood out.

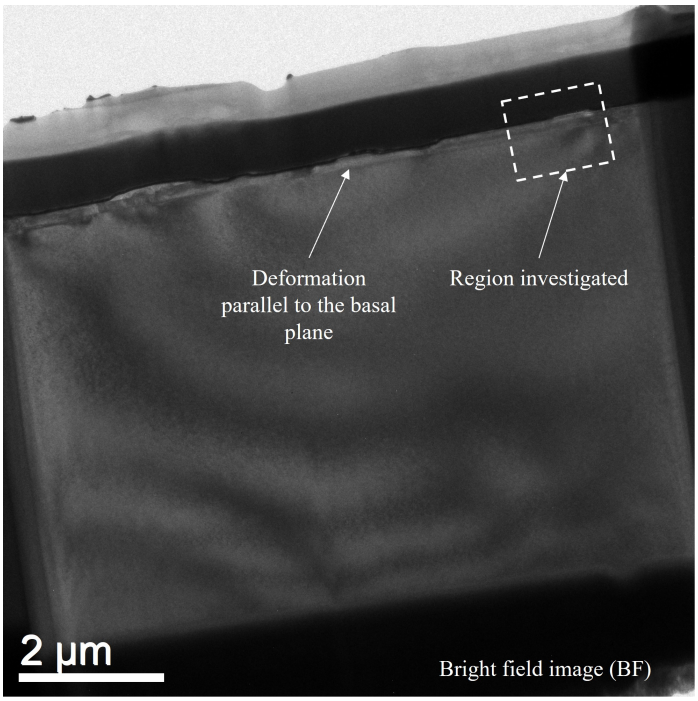

Figure 4.25: Bright field TEM image of the entire lamella showing the different features and regions of interest for the C-plane 270° cutting direction sample.

Figure 4.26(a) shows the plastically deformed regions immediately below the machined surface of the 270° cutting direction on the C-plane of sapphire. In this case, the maximum depth of the deformed region was observed to be about 200 nm below the surface and looked very similar to the region in front of the tool in Figure 4.23 with deformation activation in the basal plane. To investigate this further, HRTEM images were captured from around the two banded regions observed as shown in Figure 4.26(b) and Figure 4.26(c). From the onset, looking at the atomic

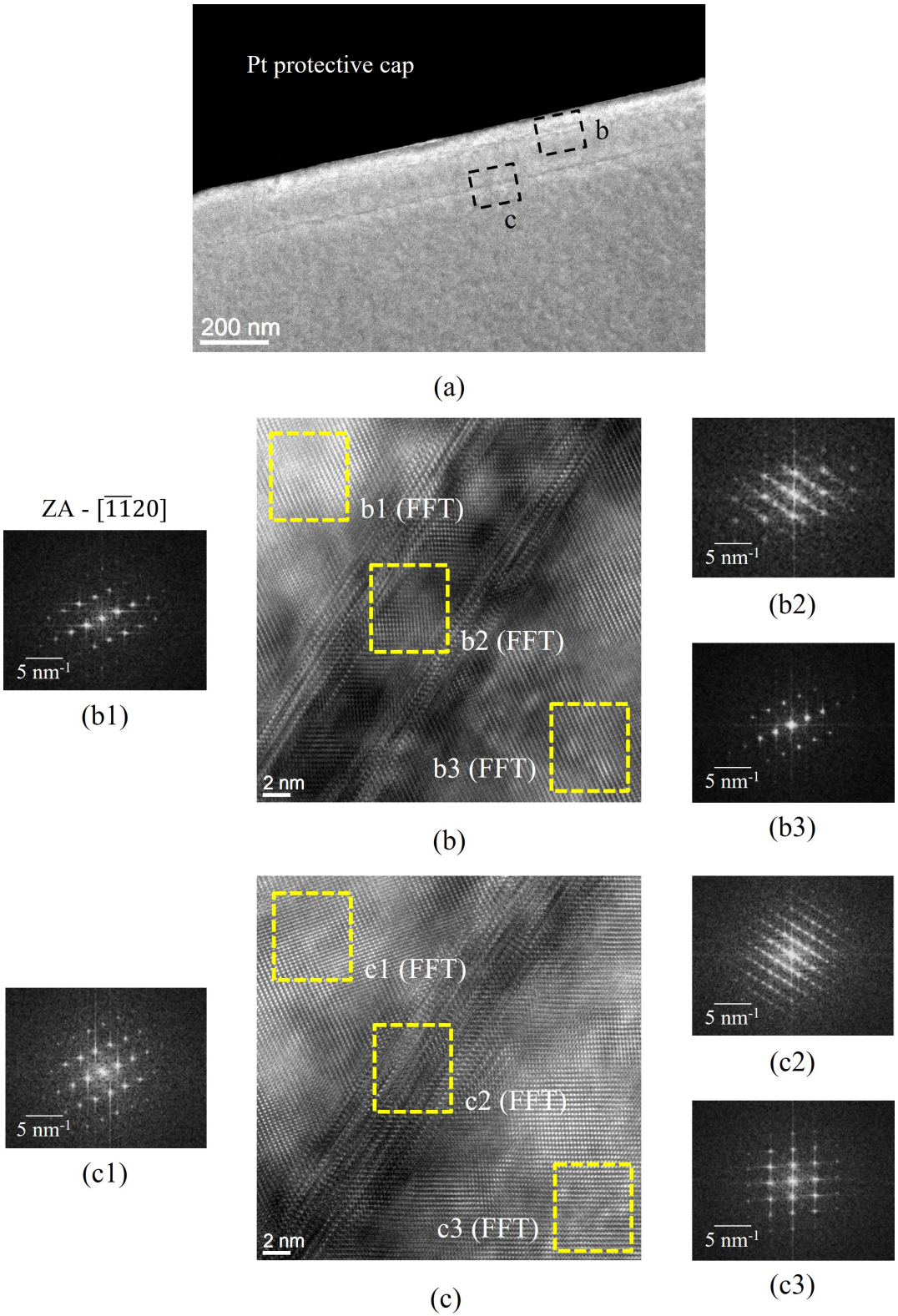

Figure 4.26: Magnified and HRTEM images of the region of interest identified in Figure 4.25 showing basal twinning deformation and FFT analysis of different regions (yellow boxes) around the twin bands.

arrangement in the HRTEM images, twinning parallel to the basal plane was visible. This was further confirmed by performing FFT in reduced regions of the image. In the case of region (b) which is closer to the machined surface, two twinning bands were visible and the FFT pattern in the region between the two bands a combination of different crystallographic orientations (Figure 4.26(b2)). In region (c), only one twinning band was observed (Figure Figure 4.26(c)) and a clear mirroring of the diffraction spots was seen through the FFT analysis.

Based on the results in this section, it was observed that the subsurface damage amount was greater in the case of the 180° cutting direction on the C-plane as compared to the 270° cutting direction which was similar to the observations from Raman spectroscopy as well. This could mean that the MD simulation results need to examined in more detail to better understand the causes for the deviations and whether the increase in the strain rate compared to experiments plays a role in influencing the deformation mechanisms.

In summary, this chapter evaluated the effect of crystal anisotropy on subsurface damage in sapphire using 3 methods - Raman spectroscopy, MD simulations, and TEM. It was found that depending on the cutting direction, there was a noticeable difference in the amount of subsurface damage. Further, it was also observed that the crack morphology played a role in influencing how the damage extended into the subsurface regions, with the shallow cracks generally limiting the damage close to the surface whereas deeper cracks extending the damage to higher depths. Through the TEM evaluations, it was observed that many different types of subsurface damage are formed during UPM of single crystal ceramics such as amorphization, fracture, twinning, and other plastic deformation mechanisms. It was also observed that in the case of the C-plane of sapphire, which predominantly has basal twinning as the dominant plastic deformation mechanism under the machining conditions used in this study, the basal twins can act as a blocking mechanism to prevent other kinds of deformation from extending into the subsurface thereby limiting the amount of subsurface damage. These insights provide ideas to think about practical machining scenarios from the perspective of controlling the mechanisms of material deformation and subsequently minimizing the surface and subsurface damage left behind after machining and are investigated in the following chapter.

Chapter 5

Influence of Process Parameters on the Characteristics of Machined Surfaces

The previous chapters aimed at understanding the influence of crystal anisotropy on residual stresses and subsurface damage formation during machining of single crystalline ceramics. To develop a fundamental understanding of the phenomenon, isolated, single machining cuts were made in various cutting directions and investigated using different techniques. However, in industry, most machining operations involve multiple machining passes over the same region of a workpiece, to get from the raw material to the final desired part geometry. As briefly explained in section 1.1, the surface and subsurface damage accumulates with each machining operation. Further, apart from the depth of cut and cutting direction, additional machining process parameters such as the machining pitch (feed rate in case of turning) need to be carefully selected. This chapter tries to develop a deeper understanding of some of these phenomenon and is presented in three sections. In the first section, the effect of horizontal overlap cutting on the CDC and crack morphology is discussed. In the second section, the effect of vertical overlap cutting on CDC is presented. The analysis in this section is also carried out from the perspective of activation of different plastic deformation mechanisms, following the methodology presented in section 2.2. In the final section, a machining strategy developed based on the knowledge gained from the previous chapters is presented. The aim of the machining strategy was to improve the throughput of machining process while minimizing surface cracking and residual stresses.

5.1 Effect of Horizontal Overlap Cutting on Critical Depth of Cut

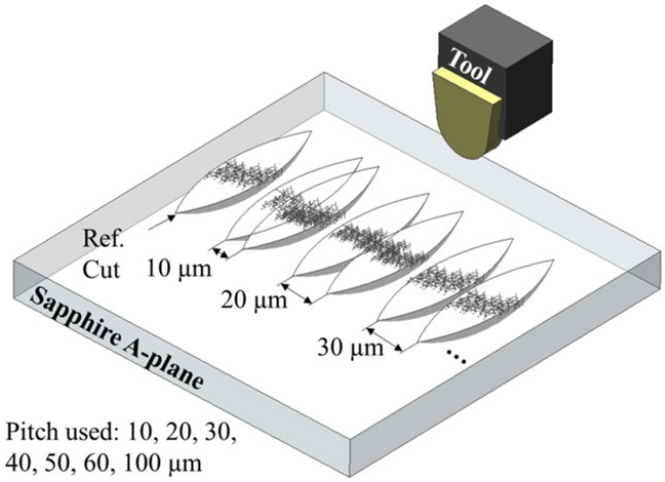

Figure 5.1: Schematic of horizontal overlap machining with different values of pitch.

The first process parameter to be tested was the machining pitch. For these experiments, the A-plane of sapphire was selected as it has a fairly large and uniform CDC around 280 nm [30] and diverse crack morphology [20] for different cutting directions. The experimental procedure followed was similar to that detailed in section 2.3. Machining was performed in the 0°, 60°, and 90° cutting directions. The reason for selecting these cutting directions was the large differences in residual stress magnitude (section 3.2.2) and alignment of the cutting directions to different slip/fracture systems. To study the effect of the machining pitch, subsequent cuts were performed at different lateral spacing values from the first cut as shown in Figure 5.1. The CDC and crack morphology were evaluated using an optical microscope.

Figure 5.2 shows the machined surfaces for different values of machining pitch. It was observed that in the case of 60° and 90° cutting directions, the crack density and size increased up to a pitch of 30 μm. This is likely caused due to the formation of lamellar cracks which are perpendicular to the cutting direction. When the second cut was performed at a pitch smaller than 30 μm, the cracks appear to extend into the newly machined regions. In the case of the 0° cutting direction, the size and density of cracks did not increase during secondary cutting. At machining pitch greater than 30 μm, the crack morphology was not influenced by the first cut.

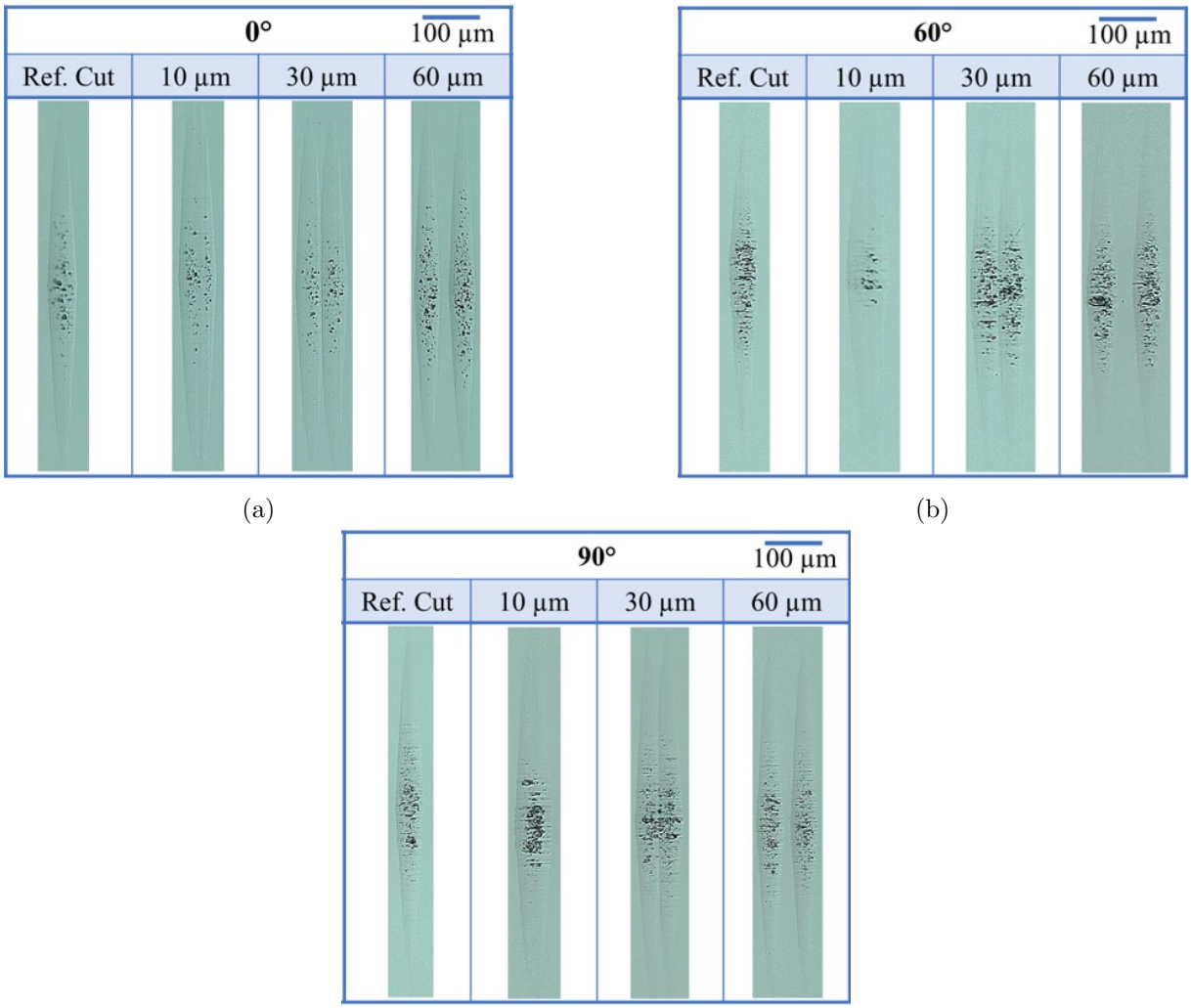

Figure 5.2: Images of cut surface for different values of machining pitch in 3 different cutting directions on the A-plane of sapphire.

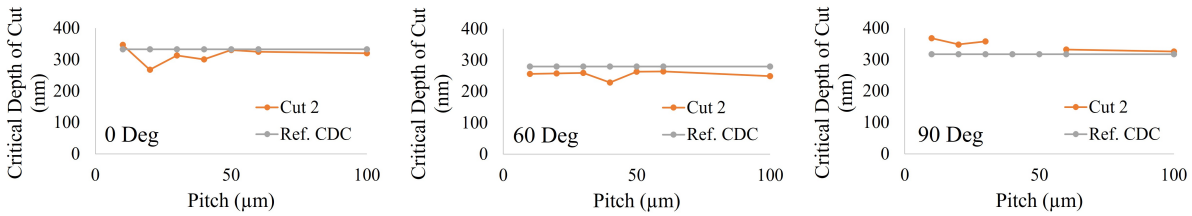

Figure 5.3: Variation in CDC for different values of machining pitch in 3 different cutting directions.

Figure 5.3 shows the variation in CDC with respect to the pitch for the three different cutting directions investigated. The horizontal overlap cutting did not seem to have a significant effect on the CDC for any of the cutting directions. One of the likely reasons for this could be due

to the rounded nose of the tool which would result in smaller material removal volume at the edges of the cut.

5.2 Effect of Vertical Overlap Cutting on Cutting on Critical Depth of Cut

The results presented in this section have been published in the proceedings of the 19th International Conference on Precision Engineering (ICPE 2022), November 28 - December 2, 2022 [123].

In the next set of experiments, vertical overlapping cuts were performed to understand the influence of the depth of cut of the first cut on subsequent machining, as shown in Figure 5.4.

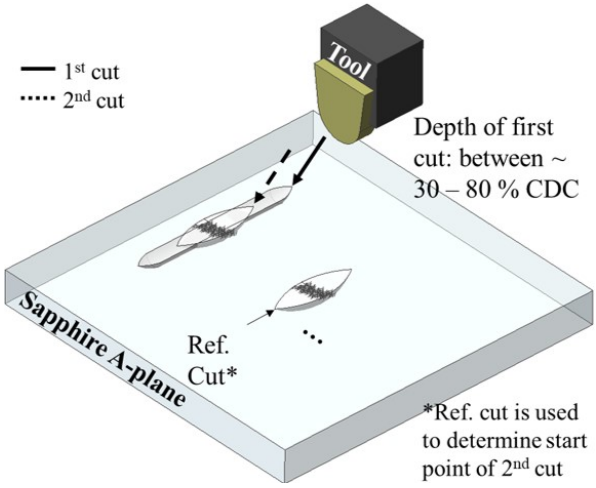

Figure 5.4: Schematic of vertical overlap machining [123].

For the reasons mentioned in section 5.1, machining was performed in the same 3 cutting directions on the A-plane of sapphire. In this experiment, the depth of cut of the first cut was varied between 30 % - 80 % of the CDC and hence no cracks were observed in the machined region. The second cut was a plunge cut over this machined area. Due to the presence of the first cut, it is difficult to identify the start point of the second cut. Hence, a reference cut was machined 150 μm away from the previous cuts. The CDC was then determined using an optical microscope. The variation in the CDC with respect to the depth of first cut is shown in Figure 5.5(a).

In the case of 0° and 60° cutting directions, as the depth of first cut was increased, the

critical depth of the second cut decreased (Figure 5.5(a)). This implies that as the depth of the first cut increases, residual stresses and subsurface damage build up which initiates cracks at a premature load during the subsequent machining operation. However, in the case of 90° cutting direction, the CDC of the second cut remained fairly consistent as the depth of first cut was increased. This implies that in the case of 90° cutting direction, either the subsurface damage and residual stresses are very low or an interaction between multiple deformation mechanisms could be acting complementary to each other which suppresses crack initiation. These results are supported by the residual stress and subsurface damage measurements discussed in sections 3.2.2 and 4.2, respectively where it was observed that the 60° cutting direction had the highest magnitude of tensile residual stress and shows the largest decline in the CDC value on subsequent cutting. In the case of 0° cutting direction, although the residual stress magnitude was lower compared to other cutting direction, displayed a sizable peak width broadening indicating the presence of subsurface damage. Lastly, the 90° cutting direction showed a small magnitude of residual stress and peak width broadening and subsequently a negligible reduction in the CDC.

In order to better understand the differences in the CDC of the second cut for different cutting directions, the tendency of activation of different plastic deformation mechanisms were calculated using the methodology described in section 2.2 and shown in Figure 5.5(b). In all the cases, rhombohedral twinning (R2, R3) was observed to be the dominant plastic deformation mechanism. However, the relative likelihood and variation with respect to depth of cut of the second cut were different for each of the cases which could possibly explain the reason for the trends observed in Figure 5.5(a). In the case of 0° and 60° cutting directions, the tendency of activation of R2 and R3 twinning are fairly similar at lower depths of cut which could lead to both the mechanisms getting activated leading to dislocation pile ups which are potential sites for crack initiation. In the case of 90° cutting direction, the tendency of activation of R3 twinning rapidly decreases which leaves behind only one dominant mechanism driving plastic deformation (R2 twinning). As a result, not much subsurface damage or residual stress accumulates in this cutting direction thus maintaining a constant CDC during subsequent machining.

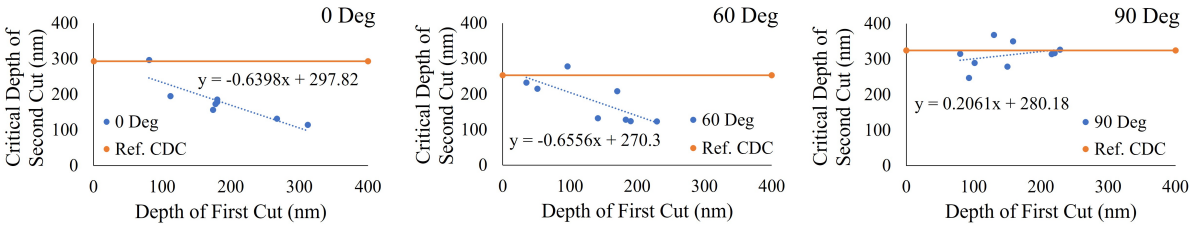

(a)

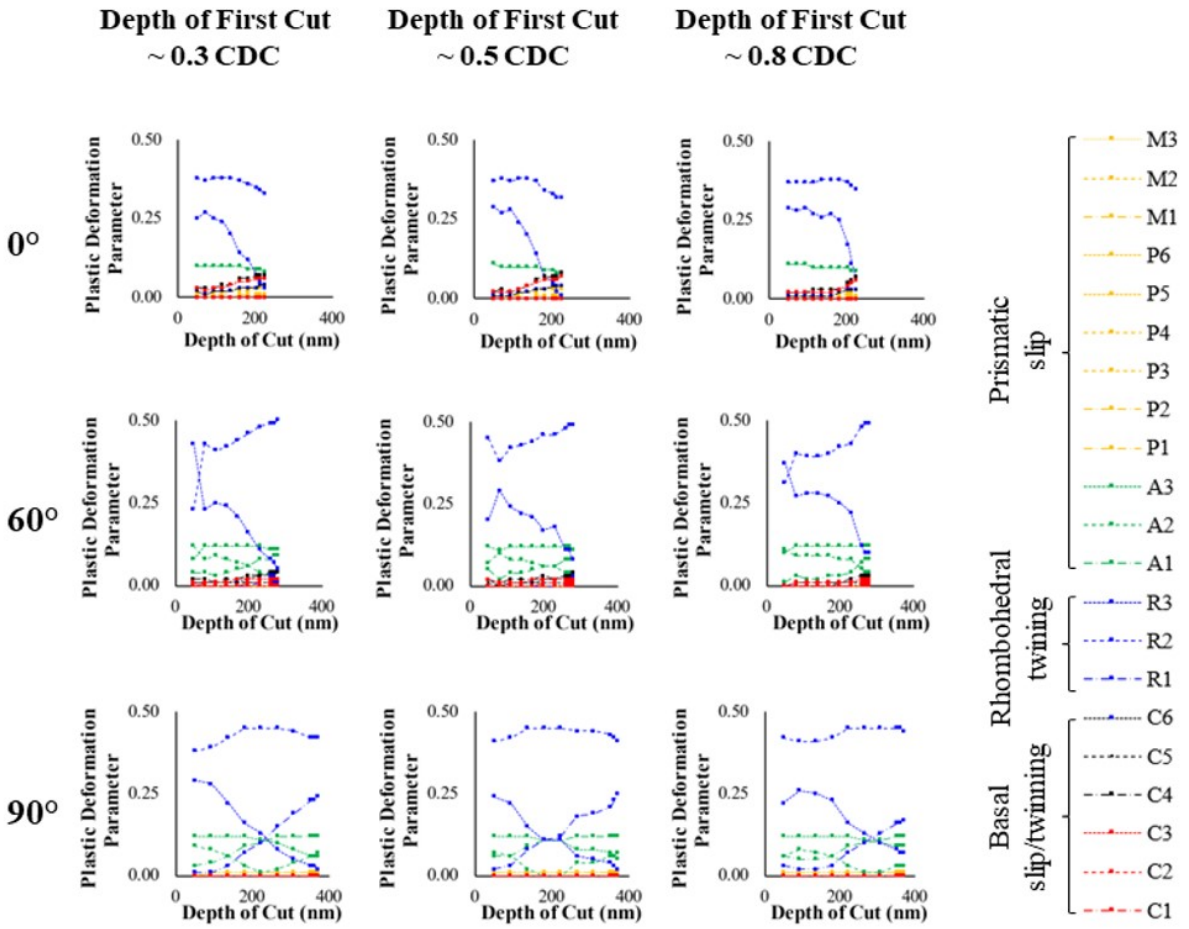

(b)

Figure 5.5: (a) Variation in CDC for different values of depth of first cut in 3 different cutting directions and (b) corresponding variations in P-parameter values on A-plane of sapphire [123].

The above two experiments on the A-plane of sapphire indicate that machining in the 90° cutting direction is favorable for rough cutting as the residual stress magnitude is low and there is not a large effect on the CDC during subsequent machining. As a result, large amounts of material can be removed in the brittle regime initially improving the throughput of the machining

process.

5.3 2-Step Machining Strategy

The aim of this experiment was to test a 2-step machining strategy that improves the machining throughput while producing a ductile surface with minimal residual stresses. This test experiment was conducted on the R-plane of sapphire since there was a clear trend of anisotropy in residual stress magnitude (Section 3.2.2). For the machining strategy, first, a machined area (1 mm × 0.6 mm) was created by cutting in the 270° cutting direction at a constant depth of 300 nm (≈3 x CDC) and a pitch of 15 μm. The subsequent machined area was created by cutting in the 180° cutting direction over the previously machined region. For the subsequent machining, plunge cuts with a maximum depth of cut of 400 nm (≈0.7 × CDC) and pitch of 15 μm were used. The 270° cutting direction was chosen for the first cut due to the low residual stress magnitude in the brittle region and a high concentration of cracks would likely cause local regions of compressive stresses [124]. The 180° cutting direction was chosen for the subsequent cut due to the high value of CDC which would aid in removing cracks on the surface and low value of residual stresses in the ductile region [21]. A schematic of the strategy is shown in Figure 5.6.

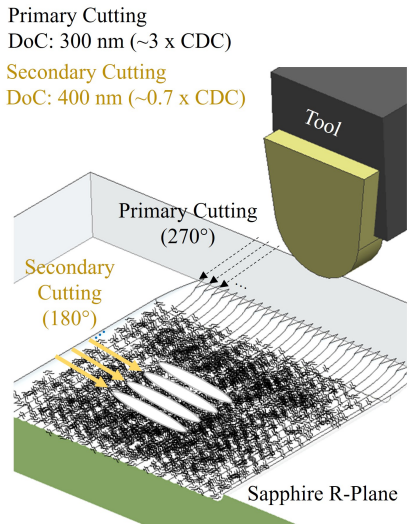

Figure 5.6: Schematic of 2-step machining on R-plane of sapphire [24].

Residual stress measurements were performed using the same parameters described in Section 3.2.1. The magnitude of residual stress was estimated by comparing the peak position in

the polished region, primary machining region (270° cutting) and subsequent machined region (180° cutting) by considering the average peak position from 72 points in a ≈36 μm × 12 μm area. Compared to the polished region, the region machined in the 270° cutting direction had an equivalent residual stress value of about -70 MPa (compressive). Although the value was closer to 0 MPa in the case of the single cut, the high density of cracks in the machined area and overlapping machining may contribute to the compressive stresses [124]. The subsequent machined area in the 180° cutting direction had an equivalent residual stress value of about -40 MPa (compressive) with respect to the polished region. This reduction in compressive magnitude of stress is likely due to ductile machining and removal of surface cracks by the subsequent machining. Evaluating the surface of the subsequent machined region, the cracks from primary cutting were partially removed. Further optimization of the depths of cuts of the primary and subsequent cutting would be necessary to remove the remaining cracks from the surface (Figure 5.7).

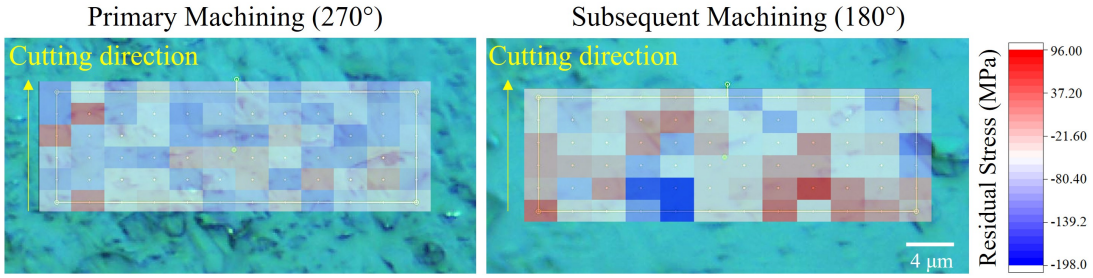

Figure 5.7: Schematic of 2-step machining on R-plane of sapphire [24].

The key takeaway from this chapter is that by developing a solid understanding of material deformation in single crystal ceramics during UPM, the material anisotropy can be exploited to improve the throughput of the machining process. Although different machining strategies and process parameters were explored in this Chapter, the number of different scenarios that can be studied are endless and it would be impossible to cover all combinations of tool geometry, machining, and crystallographic parameters. Hence, a more structured and algorithmic approach to tool path planning and G-code generation by incorporating the material deformation models would be more productive. This is discussed in more detail in the section on future work (section 6.2).

Chapter 6

Conclusion and Future Work

6.1 Summary

The seeds for the present research were sown during my master's research work where repeated cutting operations over the same area of a workpiece did not show the same values of CDC as a single cut during UPM of sapphire. These phenomenon inspired me to dig deeper and uncover the fundamental causes for this behavior and is the basis for this present work. In this regard, the phenomenon of residual stress and subsurface damage formation during UPM of sapphire and 8YSZ was investigated. The measurements of residual stress were carried out using Raman spectroscopy and nanoindentation in the case sapphire and 8YSZ respectively. Following the residual stress measurements, the residual stress magnitude in sapphire was investigated from the perspective of material deformation and activation of different slip and twinning systems. In the next step, subsurface damage evaluation was carried out using Raman spectroscopy, TEM, and MD simulations. In the final stage, the effect of a few machining parameters on the CDC and residual stress magnitude during repeated machining were tested.

The present work began with the understanding that factors such as residual stress and subsurface damage could be influencing the material removal behavior during subsequent machining operations on single crystalline ceramics. Based on the preliminary experimental results, it was hypothesized that the residual stresses and subsurface damage would be anisotropic in nature depending on the cutting direction and depth of cut due to activation of distinct deformation mechanisms in different cutting directions. To test this hypothesis, machining was performed on 4 different crystallographic planes of sapphire (A-, C-, M-, and R-) and two planes on 8YSZ ((001) and (011)). Subsequently the residual stress magnitude was quantified for 7 cutting directions on each plane of sapphire and 8YSZ. Particularly, these measurements were made at different depths of cut, focusing on the ductile, DBT, and brittle regions of the cut.

In the case of sapphire, the residual stresses were tensile in nature for most of the cases

and the ductile regions had a higher residual stress magnitude than the brittle region. The magnitude of residual stress varied from -65 MPa in a couple of cases to 148 MPa. There was a clear anisotropy in the residual stress magnitude in terms of the cutting direction and depth of cut. In crystallographic planes like the C-plane, the residual stress magnitude was almost negligible, but in some other planes like the M- and R-plane much larger magnitudes of residual stress was observed. To further understand the reason for this anisotropy, the most likely modes of plastic deformation on the C- and R-planes were calculated and compared. It was found that based on the alignment of the dominant slip/twinning system with respect to the machined surface, more plastically deformed material was likely to remain in the workpiece post machining in certain directions on the R-plane that exhibited higher magnitudes of residual stress. On the contrary, most of the plastically deformed material on the C-plane and few R-plane directions would be removed by chip formation, thus confirming the hypothesis initially presented.

In the next section, efforts were made to understand the residual stress tensor post machining. This was carried out by simultaneously accounting for the peak shift across three different peaks in the Raman spectrum of R-plane sapphire. As only three peaks were considered, the analysis was approximated to a plane strain case. It was observed that the normal stresses were in the order of -190 to 312 MPa and the trends in the principal stress closely matched the measurements from the previous section.

Next, residual stress measurements were carried out on the 2 planes of 8YSZ through analysis of nano-indentation data. For the analysis, two different approaches were followed. The first approach involved using the fracture toughness to estimate the residual stress magnitude. The residual stresses were generally tensile in nature however, in the brittle regions of the cut, very large fluctuations in the residual stress measurements were observed. The residual stresses in the ductile region varied between -35 and 240 MPa. The second approach followed a slightly different methodology by looking at the partition of elastic and plastic energy during indentation and introduced a term called resistance to machining induced cracking which indicates the amount of plastic deformation activity in the subsurface and can be indirectly related to the residual stress. It was found that the cutting directions on the (011) plane of 8YSZ exhibited higher values of resistance to machining induced cracking and thereby tensile residual stress compared to cutting directions on the (001) plane.

The second phase of this study involved understanding subsurface damage through Raman spectroscopy, TEM, and MD simulations. This portion of the study was limited to sapphire. To begin with the subsurface damage across different cutting directions was evaluated by investigating the relative peak broadening of the 417 cm^{-1} peak. These evaluations were done both in the depth wise direction (selected directions on the R-plane) and along the machined surface (A-, C-, M-, R-planes). It was observed that the crack morphology played an important role in influencing the subsurface damage and generally the directions with lateral and sculptured cracks which extended deeper into the subsurface by way of the alignment of the cleavage plane with respect to the machined surface led to higher amounts of peak broadening and subsurface damage whereas cutting directions with shallower spalling or fan shaped cracks that were restricted closer to the surface showed smaller amounts of peak broadening.

In the next section, MD simulations results from selected cutting directions were analyzed and the trends in the damage depth were compared with the results from the Raman evaluation of subsurface damage. It was observed that most of the cutting directions followed the same trends as the Raman results except for the 2 cases on the C-plane of sapphire. The likely cause for this discrepancy could be the differences in the time and length scales of the MD simulations which were performed at much higher strain rates compared to the experiments.

In the last section of this phase of the study, TEM evaluation was carried out for different cases. In the first set of cases, the subsurface damage was compared between the C- and R-plane of sapphire. It was observed that in the case of the C-plane, the damage was limited very close to the surface and the basal twinning acted like a blocking mechanism to prevent any deformation from extending deeper into the subsurface. On the contrary, larger amount of subsurface damage in the form of cracks, plastic deformation, amorphization, and stacking faults was observed on the R-plane of sapphire. These results supported the Raman spectroscopy results and the hypothesis presented at the beginning of this study. In the second set of experiments, two samples were made on the C-plane of sapphire parallel to the cutting direction along 180° and 270°. In both these samples, deformation parallel to the basal plane and just below the machined surface was observed. In the case of the 180° cutting direction, additional subsurface cracks and large amounts of plastic deformation in the subsurface were observed. However, in the 270°, the deformation was limited to few bands of basal twinning and no other forms of deformation were

observed. These trends were similar to the subsurface damage predicted from the Raman peak broadening.

The third part of this research involved investigating the effect of different process parameters such as machining pitch and depth of first cut on surface cracking, and residual stress formation during 2-step machining operations. The main objective behind this section was to further our understanding of material deformation and develop machining strategies to improve the material removal rate while minimizing surface and subsurface damage. The first two experiments involved studying the effect of machining pitch and depth of first cut on the critical depth of cut of the subsequent machining operation on the A-plane of sapphire. These experiments provided insight into how to account for different crack morphologies, residual stress state and material deformation mechanisms while choosing a machining strategy. The next stage of this research involved demonstrating a machining strategy on the R-plane of sapphire to improve the machining throughput to obtain a ductile machined surface while minimizing the residual stresses.

6.2 Future Work

As this project looked at the machining process of single crystal ceramics from the lens of three subject areas - manufacturing, materials science, and solid mechanics, potential avenues for improvement and future work were identified in each of these branches or a combination of them. The rationale behind these suggestions are either to explore topics that will further our understanding of material deformation during UPM of single crystal ceramics or help us improve the throughput of the machining process, or help improve the speed and reduce the cost of metrology for different measurements. In this regard, 6 suggested topics are introduced.

Throughout the current work, it was evident that the material deformation models and predictions worked well in the case of sapphire but carrying out work on 8YSZ was much more challenging. It is possible that the low symmetry hexagonal crystal structure of sapphire could result in more definitive modes of deformation whereas in the case of 8YSZ, the higher symmetry cubic structure could result in multiple possibilities of deformation for a given applied stress. Subsequently, it might make sense to take a step back and reevaluate the application of the P- and F- parameter models for 8YSZ and other crystal structures. Additionally, the current ap-

proach used the resultant force values to calculate the likelihood of activation of different plastic deformation and fracture systems. However, the interactions at the tool workpiece interface appear to be more complex due to the non-trivial stress field in front of the tool. Taking into account these intricacies will help improve the predictive models significantly. Further, the current models only consider plastic deformation and fracture along well defined slip and fracture planes. However, many industrially relevant materials like silicon and silicon containing ceramics have shown to deform significantly through amorphization and phase transformations. Incorporating these mechanisms into the deformation prediction models will greatly help in understanding material deformation during UPM.

As eluded to earlier, the stress field at the tool-workpiece interface plays a crucial role in determining how deformation proceeds during UPM. In order to better understand this stress field, two approaches are proposed. The first approach involves using Raman spectroscopy to measure the full residual stress tensor, as presented in section 3.2.4. The experiments suggested for this measurement would be half plunge cuts like the ones used in section 4.4.3 and making Raman measurements at the region where the tool exits the workpiece. It is suggested to perform the Raman measurements for as many different cutting directions as possible and at different depths of cut. Using the stress tensor obtained from the analysis, the P- and F- parameters can be reevaluated to see which deformation mechanisms are more likely to be activated and ideally, this approach should provide a more accurate prediction as all the components of stress would be considered. In the second phase of this study, TEM evaluations will need to be carried out in a similar fashion to section 4.4.3 to verify the predictions from the P- and F- parameter models. Additionally, another avenue to explore in this regard is from the perspective of MD simulations. Although, when using this approach, care must be taken to scale the stress measurements to account for the size and time scale effects.

With regard to the topic of understanding the stress field in front of the tool through TEM lamella parallel to the cutting direction, a new avenue in tool geometry measurement opens up. In the field of UPM, it has been known for a long time that the tool cutting edge radius plays a crucial role in influencing material deformation. Further, with improvements in technology, the edge radii or cutting tools have been becoming smaller and it is now possible to make cutting tools with an edge radius of 10s of nanometers! However, measuring the edge radius at this

scale is extremely challenging. Although Atomic Force Microscopy (AFM) is commonly used, it would be useful to have another measurement technique and TEM can help with that. By looking at the impression of the cutting tool on the workpiece in the TEM cross section, it would be possible to accurately determine the cutting edge radius of the tool. It must be noted that calculations must be done post the measurement to compensate for elastic recovery.

Through the TEM and optical microscope evaluations in section 4.4.2, section 1.1 and MD simulation results (section 4.3, it was observed that more often than not, multiple deformation mechanisms in the form of slips and twinning are often activated simultaneously due to the effect of the stress field in front of the tool. The interesting aspect of this phenomenon is that these different deformation mechanisms seem to interact with one another and influence how the deformation propagates - basal twinning blocking rhombohedral twinning from going deeper into the subsurface or two different slip activations intersecting and leading to crack initiation. Based on the current TEM and MD simulation observations, these interactions seem complex due to multiple activations. Hence to study this phenomenon of mechanism interactions at a fundamental level, it would be interesting to introduce isolated defects into the single crystal ceramic material through processes like FIB milling to simulate cleavage fractures and ion implantation to introduce twins, amorphous layers, or dislocations and then study the effect these individual defects have on the outcome of the machining process. Further, these studies can also be done using MD simulations to better understand defect evolution from a temporal point of view.

During any machining process, one of the most important considerations is the process parameters used. Due to the vast array of possible combinations, only a few items could be tested in this study. However, to improve our understanding of material deformation during UPM of ceramics, residual stress and subsurface damage formation, it is imperative to extend the experiments to include a wider range of process parameters such as different rake angles, cutting speeds, and machining conditions such as assisted machining, mist coolant supply, solid lubricants, etc. Further, it would be useful to explore how residual stresses and subsurface damage form in other machining processes such as milling and turning. In addition to gathering data from a variety of process parameter experiments, this knowledge will be useful only when it is implemented in tool path or G-code generation. Currently there are no CAM software

that take into account the effect of crystal structure and anisotropy while generating tool paths but making this consideration could potentially lead to multifold improvement in the machining throughput by exploiting the deformation anisotropy.

Lastly, due to the vast amounts of data collected in this and related projects, it would be interesting to explore data driven approaches to help speed up some of the metrology tasks. Some ideas in this regard include predicting the residual stress magnitude from optical microscope images. As the Raman data was captured in the form of mapped data in this work, it is possible to assign stress values to different pixels on a microscope image of the machined surface and train a machine learning algorithm. This approach could help reduce the metrology time and cost as optical microscope capture is much quicker than other techniques such as Raman spectroscopy and nanoindentation.

Appendix A

Appendix

A.1 Material Properties

A.1.1 Sapphire

Table A.1: Physical properties of sapphire

Property	Units	Value	Reference
Density	g/cm^3	3.98	[125]
Hardness	Mohs	9	[125]
Elastic Modulus	GPa	322-494	[29]
Melting Point	°C	2040	[125]
Thermal Conductivity	W/(m.K)	46.06 at 0°C	[125]
Fracture Toughness	$MPa.m^{1/2}$	2.14	[126]
Permeable Wavelengths	nm	170-5500	[127]

A.1.2 8-mol % yttria stabilized zirconia (8YSZ)

Table A.2: Physical properties of 8YSZ

Property	Units	Value	Reference
Density	g/cm^3	5.8	[128]
Hardness	Mohs	8 - 8.5	[129]
Elastic Modulus	GPa	220-275	[130]
Melting Point	°C	2500	[128]
Thermal Conductivity	W/(m.K)	2.8 at 27 °C	[131]
Fracture Toughness	$MPa.m^{1/2}$	1.29	[132]
Permeable Wavelengths	nm	$\geq$300	[133]

A.2 List of Equipment Used

Table A.3: Details of equipment used throughout this study.

Description/Purpose	**Equipment Model and Make**
Machine Tool	FANUC ROBONANO α-0iB, FANUC Corp., Japan
Dynamometer	Type 911AA1, Kistler Instrument Corp., Switzerland
Charge Amplifier	Type 5080A, Kistler Instrument Corp., Switzerland
Tilt Stage	IS-1016B, OptoSigma Corporation, USA
Digital Surface Probe	Brown & Sharpe 599-988 indicator probe used with Tesatronic TT10 display, TESA Technology, Switzerland
Tool Setting Microscope	SH140CCD-2R, Shodensha Inc., Japan
Optical Microscope	VHX 5000, Keyence Corp., Japan
Scanning Electron Microscope	LEO 1530, Carl Zeiss GmbH, Germany
Confocal Raman Microscope	LabRAM HR Evolution, Horiba Ltd., Japan
Nanoindenter	Hysitron TI 950, Bruker Corporation, USA
FIB Milling	Zeiss Auriga, Carl Zeiss Microscopy GmbH, Germany
Transmission Electron Microscope	FEI Tecnai TF-30 300 kV TEM, FEI Technologies Inc, USA

A.3 FIB Milling Parameters for TEM Sample Preparation

Table A.4: List of process parameters used during FIB milling for TEM lamella preparation.

Tilt Stage to 54°										
Step 1 - Platinum deposition										
Milling mode	**Width (µm)**	**Height (µm)**	**X frequency**	**Y frequency**	**Milling current**	**Time (s)**	**Gas ID 1**	**Gas ID 2**	**Gas wait time**	**Comments**
Deposition mode	22	3	20,000	1	300 pA	480	None	Platinum	3	Can use GIS 1 or GIS 2
Step 2 - Carbon deposition										
Milling mode	**Width (µm)**	**Height (µm)**	**X frequency**	**Y frequency**	**Milling current**	**Time (s)**	**Gas ID 1**	**Gas ID 2**	**Gas wait time**	**Comments**
Deposition mode	22	3	20,000	1	300 pA	480	Carbon	None	3	Carbon is available only on GIS 1
Step 3a - Trapezoidal milling 1										
Milling mode	**Width (µm)**	**Height (µm)**	**Depth (µm)**	**No. of layers**	**Material**	**Slope (°)**	**Milling current**	**Angle**	**Track WD**	**Comments**
Mill for depth	20	10	15	60	Al2O3	30	12 nA	0	No	Position the milling area ~0.5µm away from Pt/C deposition; Time ~19:54
Step 3b - Trapezoidal milling 2										
Milling mode	**Width (µm)**	**Height (µm)**	**Depth (µm)**	**No. of layers**	**Material**	**Slope (°)**	**Milling current**	**Angle**	**Track WD**	**Comments**
Mill for depth	20	10	15	60	Al2O3	30	12 nA	180	No	Use the flip option and ~5-6µm flip distance to position the milling area ~1µm away from Pt/C deposition; Time ~19:54
Step 4a - Rectangular milling - clean the sample walls - side 1										
Milling mode	**Width (µm)**	**Height (µm)**	**Depth (µm)**	**No. of layers**	**Material**	**Slope (°)**	**Milling current**	**Angle**	**Track WD**	**Comments**
Mill for depth	20	2	15	30	Al2O3	0	8 nA	0	No	Start slightly away from the sample; Time ~ 8:52
Step 4b - Rectangular milling - clean the sample walls - side 1										
Milling mode	**Width (µm)**	**Height (µm)**	**Depth (µm)**	**No. of layers**	**Material**	**Slope (°)**	**Milling current**	**Angle**	**Track WD**	**Comments**
Mill for depth	20	2	15	30	Al2O3	0	4 nA	0	No	Additional steps might be necessary if a clean surface is not obtained; Time ~ 14:12

Step 4c - Rectangular milling - clean the sample walls - side 2										
Milling mode	**Width (µm)**	**Height (µm)**	**Depth (µm)**	**No. of layers**	**Material**	**Slope (°)**	**Milling current**	**Angle**	**Track WD**	**Comments**
Mill for depth	20	2	15	30	Al2O3	0	8 nA	0	No	Use the flip option and ~3-4 µm flip distance to position the milling area ~1µm away from Pt/C deposition ; Time ~ 8:52

Step 4d - Rectangular milling - clean the sample walls - side 2										
Milling mode	**Width (µm)**	**Height (µm)**	**Depth (µm)**	**No. of layers**	**Material**	**Slope (°)**	**Milling current**	**Angle**	**Track WD**	**Comments**
Mill for depth	20	2	15	30	Al2O3	0	4 nA	0	No	Additional steps might be necessary if a clean surface is not obtained (can check only in FIB image); Time ~ 14:12

Tilt Stage to 0°

Step 5 - J-cut Step 5a - bottom										
Milling mode	**Width (µm)**	**Height (µm)**	**-**	**No. of Layers**	**-**	**Time (s)**	**Milling current**	**Angle**	**Track WD**	**Comments**
Mill for time	20	0.75	-	60	-	200	2 nA	180	No	Some adjustment in the position might be necessary for the cut to succeed. Watch for the dark line in the trench cut by trapezoidal cut. 200 - 240 s needed for this operation

Step 5b - Left side										
Milling mode	**Width (µm)**	**Height (µm)**	**-**	**No. of Layers**	**-**	**Time (s)**	**Milling current**	**Angle**	**Track WD**	**Comments**
Mill for time	0.75	0.75	-	60	-	200	2 nA	180	No	Make sure the cut goes below the cut from step 5 a

Step 5c - Right side (partial)										
Milling mode	**Width (µm)**	**Height (µm)**	**-**	**No. of Layers**	**-**	**Time (s)**	**Milling current**	**Angle**	**Track WD**	**Comments**
Mill for time	0.75	0.75	-	60	-	200	2 nA	180	No	Make sure the cut goes below the cut from step 5 a

Step 6 - Insert Omniprobe										
Comments										
- Disable touch alarm ->check SCM on; Can be accessed from Specimen Current Monitor Menu										
Step 6a - Weld Omniprobe to sample										
Milling mode	**Width (µm)**	**Height (µm)**	**X frequency**	**Y frequency**	**Milling current**	**Time (s)**	**Gas ID 1**	**Gas ID 2**	**Gas wait time**	**Comments**
Deposition mode	2.5	2.5	20,000	1	20 pA	300	None	Pt	3	This operation must use GIS 2. It will not work with GIS 1. Check if there is sufficient deposition

Step 5d - Right side (remaining material)										
Milling mode	**Width (µm)**	**Height (µm)**	**-**	**No. of Layers**	**-**	**Time (s)**	**Milling current**	**Angle**	**Track WD**	**Comments**
Mill for time	0.75	0.75	-	60	-	200	2 nA	180	No	Make sure the sample is properly separated

Step 7 - TEM grid preparatory milling										
Milling mode	**Width (µm)**	**Height (µm)**	**-**	**No. of Layers**	**-**	**Time (s)**	**Milling current**	**Angle**	**Track WD**	**Comments**
Mill for time	14	2	-	60	-	200	2 nA	180	No	This is to create a small pocket in the TEM grid to seat the sample; Width should be ~2-3 µm larger than sample width

Step 8 - Weld TEM lamella to grid										
Milling mode	**Width (µm)**	**Height (µm)**	**X frequency**	**Y frequency**	**Milling current**	**Time (s)**	**Gas ID 1**	**Gas ID 2**	**Gas wait time**	**Comments**
Deposition mode	2.5	2.5	20,000	1	20 pA	300	None	Pt	3	This operation must use GIS 2. It will not work with GIS 1. Check if there is sufficient deposition; reposition and repeat as necessary (2-4 times)

Step 9 - Detach Omniprobe										
Milling mode	**Width (µm)**	**Height (µm)**	**-**	**No. of Layers**	**-**	**Time (s)**	**Milling current**	**Angle**	**Track WD**	**Comments**
Mill for time	0.75	0.75	-	60	-	120	2 nA	180	No	Make sure the Omniprobe is detached from the sample; reposition and repeat if necessary

- Re-enable touch alarm -> uncheck SCM on; Can be accessed from Specimen Current Monitor Menu

Tilt Stage to 54°

Step 10a - Side 1 thinning (1 of 4)

Milling mode	Width (µm)	Height (µm)	Depth (µm)	No. of layers	Material	Slope (°)	Milling current	Angle	Track WD	Comments
Mill for depth	17	1.5	10	1	Al2O3	0	2 nA	0	No	Start from slightly outside the sample; May need to be repeated if the sample is too thick

Step 10b - Side 1 thinning (2 of 4)

Milling mode	Width (µm)	Height (µm)	Depth (µm)	No. of layers	Material	Slope (°)	Milling current	Angle	Track WD	Comments
Mill for depth	16	1	10	1	Al2O3	0	300 pA	0	No	May need to be repeated if the sample is too thick

Step 10c - Side 1 thinning (3of 4)

Milling mode	Width (µm)	Height (µm)	Depth (µm)	No. of layers	Material	Slope (°)	Milling current	Angle	Track WD	Comments
Mill for depth	15	0.6	15	1	Silicon	0	140 pA	0	No	

Tilt Stage to 55.5°

Step 10d - Side 1 thinning (4 of 4)

Milling mode	Width (µm)	Height (µm)	Depth (µm)	No. of layers	Material	Slope (°)	Milling current	Angle	Track WD	Comments
Mill for depth	14	0.5	15	1	Silicon	0	50 pA	0	No	

Stage Delta Rotation by 180°

Step 11a - Side 1 thinning (1 of 4)

Milling mode	Width (µm)	Height (µm)	Depth (µm)	No. of layers	Material	Slope (°)	Milling current	Angle	Track WD	Comments
Mill for depth	17	0.7	10	1	Al2O3	0	2 nA	0	No	Start from slightly outside the sample; May need to be repeated if the sample is too thick

Step 11b - Side 1 thinning (2 of 4)

Milling mode	Width (µm)	Height (µm)	Depth (µm)	No. of layers	Material	Slope (°)	Milling current	Angle	Track WD	Comments
Mill for depth	16	0.4	15	1	Silicon	0	300 pA	0	No	If not already switched, must use SE2 detector from this stage

Step 11c - Side 2 thinning (3of 4)										
Milling mode	**Width (µm)**	**Height (µm)**	**Depth (µm)**	**No. of layers**	**Material**	**Slope (°)**	**Milling current**	**Angle**	**Track WD**	**Comments**
Mill for depth	15	0.2	15	1	Silicon	0	140 pA	0	No	

Step 11d - Side 2 thinning (4 of 4)										
Milling mode	**Width (µm)**	**Height (µm)**	**Depth (µm)**	**No. of layers**	**Material**	**Slope (°)**	**Milling current**	**Angle**	**Track WD**	**Comments**
Mill for depth	14	0.3	15	1	Silicon	0	50 pA	0	No	Select the entire sample as the height of the box; Watch for electron transparency

TEM sample preperation is complete!
Tilt stage to 0°

General Comments

- All milling/deposition done at 30 kV (except the last thinning step - done at 5 kV)
- Red line of the rectangles/trapezium should face the sample area
- Disable touch alarm when using Omniprobe (check SCM on), re-enable touch alarm (uncheck SCM on) after detaching Omniprobe (Specimen Current Monitor Menu)
- Each time the GIS is inserted, check the positioning on the FIB image
- Once the stage is moved to a position, limit the movement until all operations in that location are completed
- Once the omniprobe or GIS are inserted DO NOT move the stage
- Constantly check the emission current (should be 2µA)
- If the FIB shuts off after deposition, outgas the Pt (when outgassing, make sure column chamber valve is closed (Airlock menu)); Outgas option can be accessed from Gas Injection System Menu
- If no deposition is happening, Pt could be empty - notify the staff

Bibliography

[1] National Ignition Facility, Lawrence Livermore National Laboratory (2024, Nov. 2), "KDP optical switch." Retrieved from https://lasers.llnl.gov/about/how-nif-works/seven-wonders/optical-switch.

[2] J. Lynch (2024, Nov. 2), "Key Parker Solar Probe sensor bests sun simulator—last launch hurdle." Retrieved from https://news.engin.umich.edu/2018/04/key-parker-solar-probe-sensor-bests-sun-simulator-last-launch-hurdle/.

[3] National Aeronautics and Space Administration (NASA) (2024, Nov. 2), "Ten Inventions Created for James Webb Space Telescope Approved." Retrieved from https://science.nasa.gov/mission/webb/innovations/.

[4] N. Vail, L. Swain, W. Fox, T. Aufdlemorte, G. Lee, and J. Barlow, "Materials for biomedical applications," *Materials & Design*, vol. 20, no. 2-3, pp. 123–132, 1999.

[5] J. Pelleg, *Mechanical properties of ceramics*, vol. 213. Springer Science & Business, 2014.

[6] J. Lu, M. Prabhu, J. Song, C. Li, J. Xu, K. Ueda, A. Kaminskii, H. Yagi, and T. Yanagitani, "Optical properties and highly efficient laser oscillation of Nd: YAG ceramics," *Applied Physics B*, vol. 71, pp. 469–473, 2000.

[7] P. Parikh, "Alumina ceramics: engineering applications and domestic market potential," *Transactions of the Indian Ceramic Society*, vol. 54, no. 5, pp. 179–184, 1995.

[8] J. Cheng, J. Wu, Y. Zhou, Y. Gong, X. Wen, and Q. Wen, "Characterization of fracture toughness and micro-grinding properties of monocrystal sapphire with a multi-layer toughening micro-structure (mtm)," *Journal of Materials Processing Technology*, vol. 239, pp. 258–272, 2017.

[9] D. M. Allen, R. Redondo, and M. Dany, "Fabrication methods for the manufacture of sapphire microparts," *Microsystem technologies*, vol. 18, pp. 1835–1841, 2012.

[10] E. Brinksmeier, Y. Mutlugünes, F. Klocke, J. Aurich, P. Shore, and H. Ohmori, "Ultra-precision grinding," *CIRP annals*, vol. 59, no. 2, pp. 652–671, 2010.

[11] H. Ohmori, "Electrolytic in-process dressing (elid) grinding for optical parts manufacturing," in *International Progress in Precision Engineering*, pp. 134–148, Elsevier, 1993.

[12] M. Jiang, N. O. Wood, and R. Komanduri, "On chemo-mechanical polishing (cmp) of silicon nitride (si3n4) workmaterial with various abrasives," *Wear*, vol. 220, no. 1, pp. 59–71, 1998.

[13] Z. Zhang, W. Yan, L. Zhang, W. Liu, and Z. Song, "Effect of mechanical process parameters on friction behavior and material removal during sapphire chemical mechanical polishing," *Microelectronic Engineering*, vol. 88, no. 9, pp. 3020–3023, 2011.

[14] FANUC Corp. (2022, Jan. 5), "FANUC ROBONANO α-NMiA, Ultra precision machine for mass production." Retrieved from https://www.fanuc.eu/es/en/robonano.

[15] Precitech (2024, Nov. 2), "Freeform MGG – and Ultra Precision Mill." Retrieved from https://www.precitech.com/product/freeform/.

[16] S. Joshi, "Ultraprecision machining (upm)," *Encyclopedia of nanotechnology*, pp. 4253–4260, 2016.

[17] M. Rahman, K. Woon, V. Venkatesh, and M. Rahman, "Modelling of the combined microstructural and cutting edge effects in ultraprecision machining," *CIRP Annals*, vol. 67, no. 1, pp. 129–132, 2018.

[18] A. Aramcharoen and P. Mativenga, "Size effect and tool geometry in micromilling of tool steel," *Precision Engineering*, vol. 33, no. 4, pp. 402–407, 2009.

[19] Y. Mizumoto, *Investigation on Surface Integrity in Ultra-precision Cutting of Single Crystalline Optical Materials for Microcavity.* PhD thesis, Keio University, 2018.

[20] A. Nagaraj, "Study on surface crack removal and effect of subsequent machining in sapphire," Master's thesis, University of Wisconsin–Madison, 2019.

[21] A. Nagaraj, S. B. Kwon, H.-S. Yoon, and S. Min, "Crack removal behavior in ultraprecision machining of sapphire," *Procedia Manufacturing*, vol. 34, pp. 393–398, 2019.

[22] H.-S. Yoon, S. B. Kwon, A. Nagaraj, and S. Min, "Effect of the initial-flaw on crack-propagation in two-step cutting of monocrystalline sapphire," *Journal of Manufacturing Processes*, vol. 56, pp. 1211–1218, 2020.

[23] Y. Mizumoto, P. Maas, Y. Kakinuma, and S. Min, "Investigation of the cutting mechanisms and the anisotropic ductility of monocrystalline sapphire," *CIRP Annals*, vol. 66, no. 1, pp. 89–92, 2017.

[24] A. Nagaraj and S. Min, "Effect of crystallography on residual stresses during ultraprecision machining of sapphire," *CIRP Annals*, vol. 71, no. 1, pp. 101–104, 2022.

[25] B. Jiao, Q. Zhao, Y. Zhao, W. Zhang, Y. Li, Z. Hu, X. Gao, C. Cui, M. Wu, and T. Xin, "A new approach to understand the deformation behavior and strengthening mechanism of molybdenum alloy: From single crystal to polycrystal," *International Journal of Refractory Metals and Hard Materials*, vol. 102, p. 105715, 2022.

[26] A. Simoneau, E. Ng, and M. Elbestawi, "Surface defects during microcutting," *International Journal of Machine Tools and Manufacture*, vol. 46, no. 12-13, pp. 1378–1387, 2006.

[27] K. Saptaji, *Mechanical Micro-machining*, pp. 1–18. London: Springer London, 2013.

[28] S. Goel, A. Stukowski, X. Luo, A. Agrawal, and R. L. Reuben, "Anisotropy of single-crystal 3c–sic during nanometric cutting," *Modelling and Simulation in Materials Science and Engineering*, vol. 21, no. 6, p. 065004, 2013.

[29] E. R. Dobrovinskaya, L. A. Lytvynov, and V. Pishchik, *Sapphire: material, manufacturing, applications.* Springer Science & Business Media, 2009.

[30] H.-S. Yoon, S. B. Kwon, A. Nagaraj, S. Lee, and S. Min, "Study of stress intensity factor on the anisotropic machining behavior of single crystal sapphire," *CIRP Annals*, vol. 67, no. 1, pp. 125–128, 2018.

[31] A. Bagchi and P. K. Wright, "Stress analysis in machining with the use of sapphire tools," *Proceedings of the Royal Society of London. A. Mathematical and Physical Sciences*, vol. 409, no. 1836, pp. 99–113, 1987.

[32] J. B. Levine, T. Burks, J. Ciraldo, M. Montgomery, A. Novoselov, and S. Podlozhenov, "Synthesis and characterization of large optical grade sapphire windows produced from a horizontal growth process," in *Window and Dome Technologies and Materials XIII*, vol. 8708, pp. 80–85, SPIE, 2013.

[33] Y. Akagawa, M. Hashimoto, N. Kondo, K. Satomi, T. Takata, and H. Tsuru, "Initial bone-implant interfaces of submergible and supramergible endosseous single-crystal sapphire implants," *The Journal of prosthetic dentistry*, vol. 55, no. 1, pp. 96–100, 1986.

[34] A. Lanin, E. Muravin, V. Popov, and V. Turchin, "Thermal shock resistance and thermal-mechanical processing of sapphire," *Journal of the European Ceramic Society*, vol. 23, no. 3, pp. 455–468, 2003.

[35] Z. Li, Z. Pei, and P. Funkenbusch, "Machining processes for sapphire wafers: a literature review," *Proceedings of the Institution of Mechanical Engineers, Part B: Journal of Engineering Manufacture*, vol. 225, no. 7, pp. 975–989, 2011.

[36] Z. Liang, X. Wang, Y. Wu, L. Xie, L. Jiao, and W. Zhao, "Experimental study on brittle–ductile transition in elliptical ultrasonic assisted grinding (euag) of monocrystal sapphire using single diamond abrasive grain," *International Journal of Machine Tools and Manufacture*, vol. 71, pp. 41–51, 2013.

[37] X. Wang, G. Lim, H. Zheng, F. Ng, W. Liu, and S. Chua, "Femtosecond pulse laser ablation of sapphire in ambient air," *Applied Surface Science*, vol. 228, no. 1-4, pp. 221–226, 2004.

[38] K. Arvidson, B. Fartash, M. Hilliges, and P. Köndell, "Histological characteristics of peri-implant mucosa around brånemark and single-crystal sapphire implants," *Clinical oral implants research*, vol. 7, no. 1, pp. 1–10, 1996.

[39] A. W. Case, J. C. Kasper, M. L. Stevens, K. E. Korreck, K. Paulson, P. Daigneau, D. Caldwell, M. Freeman, T. Henry, B. Klingensmith, *et al.*, "The solar probe cup on the parker solar probe," *The Astrophysical Journal Supplement Series*, vol. 246, no. 2, p. 43, 2020.

[40] J. I. Mackenzie, "Dielectric solid-state planar waveguide lasers: a review," *IEEE Journal of Selected Topics in Quantum Electronics*, vol. 13, no. 3, pp. 626–637, 2007.

[41] Roditi (2024, Nov. 12), "Sapphire Substrate - A-Plane." Retrieved from https://www.roditi.com/SingleCrystal/Sapphire/A-Plane.html.

[42] M. F. Schubert, S. Chhajed, J. K. Kim, E. Fred Schubert, and J. Cho, "Polarization of light emission by 460nm gainn/ gan light-emitting diodes grown on (0001) oriented sapphire substrates," *Applied Physics Letters*, vol. 91, no. 5, 2007.

[43] J. Sabataitis, C. Mueller, F. Miranda, J. Warner, and K. Bhasin, "Ybco high-temperature superconducting filters on m-plane sapphire substrates," *Advances in Cryogenic Engineering: Part A*, pp. 1755–1760, 1996.

[44] D. Iida, A. Miura, Y. Okadome, Y. Tsuchiya, T. Kawashima, T. Nagai, M. Iwaya, S. Kamiyama, H. Amano, and I. Akasaki, "One-step lateral growth for reduction in defect density of a-plane gan on r-sapphire substrate and its application in light emitters," *physica status solidi (a)*, vol. 204, no. 6, pp. 2005–2009, 2007.

[45] Meller Optics (2024, Nov. 13), "Properties and Applications of Sapphire." Retrieved from https://melleroptics.com/wp-content/uploads/2022/10/SAPPHIRE-WHITE-PAPER-FINAL-REV-A.pdf.

[46] J. Clayton, "A continuum description of nonlinear elasticity, slip and twinning, with application to sapphire," *Proceedings of the Royal Society A: Mathematical, Physical and Engineering Sciences*, vol. 465, no. 2101, pp. 307–334, 2009.

[47] M. Iwasa and R. Bradt, "Fracture toughness of single-crystal alumina," *Advances in ceramics*, vol. 10, p. 767, 1984.

[48] R. H. Hannink, P. M. Kelly, and B. C. Muddle, "Transformation toughening in zirconia-containing ceramics," *Journal of the American Ceramic Society*, vol. 83, no. 3, pp. 461–487, 2000.

[49] P. K. Schelling, S. R. Phillpot, and D. Wolf, "Mechanism of the cubic-to-tetragonal phase transition in zirconia and yttria-stabilized zirconia by molecular-dynamics simulation," *Journal of the American Ceramic Society*, vol. 84, no. 7, pp. 1609–1619, 2001.

[50] J. Chevalier, L. Gremillard, A. V. Virkar, and D. R. Clarke, "The tetragonal-monoclinic transformation in zirconia: lessons learned and future trends," *Journal of the american ceramic society*, vol. 92, no. 9, pp. 1901–1920, 2009.

[51] R. Batista and E. Muccillo, "Structure, microstructure and electrical conductivity of 8ysz containing nio," *Ceramics International*, vol. 37, no. 6, pp. 1929–1934, 2011.

[52] H.-S. Yoon, S. Lee, and S. Min, "Investigation of ductile-brittle transition in machining of yttrium-stabilized zirconia (YSZ)," *Procedia Manufacturing*, vol. 26, pp. 446–453, 2018.

[53] E. Camposilvan, F. G. Marro, A. Mestra, and M. Anglada, "Enhanced reliability of yttria-stabilized zirconia for dental applications," *Acta Biomaterialia*, vol. 17, pp. 36–46, 2015.

[54] L. Chen, "Yttria-stabilized zirconia thermal barrier coatings—a review," *Surface Review and Letters*, vol. 13, no. 05, pp. 535–544, 2006.

[55] U. Anselmi-Tamburini, J. N. Woolman, and Z. A. Munir, "Transparent nanometric cubic and tetragonal zirconia obtained by high-pressure pulsed electric current sintering," *Advanced Functional Materials*, vol. 17, no. 16, pp. 3267–3273, 2007.

[56] P. Vinchhi, M. Khandla, K. Chaudhary, and R. Pati, "Recent advances on electrolyte materials for sofc: A review," *Inorganic Chemistry Communications*, vol. 152, p. 110724, 2023.

[57] O. A. Graeve, "Zirconia," in *Ceramic and glass materials: structure, properties and processing*, pp. 169–197, Springer, 2008.

[58] H. Masuda, K. Morita, M. Watanabe, T. Hara, H. Yoshida, and T. Ohmura, "Ferroelastic and plastic behaviors in pseudo-single crystal micropillars of nontransformable tetragonal zirconia," *Acta Materialia*, vol. 203, p. 116471, 2021.

[59] C.-Y. Yen, S.-R. Jian, Y.-C. Tseng, and J.-Y. Juang, "The deformation behavior and fracture toughness of single crystal ysz (111) by indentation," *Journal of Alloys and Compounds*, vol. 735, pp. 2423–2427, 2018.

[60] A. Pajares, F. Guiberteau, A. Dominguez-Rodriguez, and A. H. Heuer, "Microhardness and fracture toughness anisotropy in cubic zirconium oxide single crystals," *Journal of the American Ceramic Society*, vol. 71, no. 7, pp. C–332, 1988.

[61] G. Yang and S.-J. Park, "Deformation of single crystals, polycrystalline materials, and thin films: A review," *Materials*, vol. 12, no. 12, p. 2003, 2019.

[62] A. Montagne, S. Pathak, X. Maeder, and J. Michler, "Plasticity and fracture of sapphire at room temperature: Load-controlled microcompression of four different orientations," *Ceramics International*, vol. 40, no. 1, pp. 2083–2090, 2014.

[63] S. B. Kwon, A. Nagaraj, H.-S. Yoon, and S. Min, "Study of material removal behavior on r-plane of sapphire during ultra-precision machining based on modified slip-fracture model," *Nanotechnology and Precision Engineering*, vol. 3, no. 3, pp. 141–155, 2020.

[64] A. A. Griffith, "Vi. the phenomena of rupture and flow in solids," *Philosophical transactions of the royal society of london. Series A, containing papers of a mathematical or physical character*, vol. 221, no. 582-593, pp. 163–198, 1921.

[65] P. Hirsch, "Crack-tip plasticity and quasi-brittle fracture of single crystals," in *Plastic deformation of ceramics*, pp. 1–19, Springer, 1995.

[66] H. Sumiya, K. Harano, and D. Murakami, "Application of nano-polycrystalline diamond to cutting tools," *SEI Technical Review*, vol. 75, p. 18, 2012.

[67] Q. Huang, D. Yu, B. Xu, W. Hu, Y. Ma, Y. Wang, Z. Zhao, B. Wen, J. He, Z. Liu, *et al.*, "Nanotwinned diamond with unprecedented hardness and stability," *Nature*, vol. 510, no. 7504, pp. 250–253, 2014.

[68] H.-S. Yoon, S. B. Kwon, A. Nagaraj, and S. Min, "Investigation of the ductile cutting behavior of monocrystalline yttria-stabilized zirconia during ultra-precision orthogonal cutting," *International Journal of Precision Engineering and Manufacturing*, vol. 20, pp. 1475–1484, 2019.

[69] A. Nagaraj, S. B. Kwon, D. Xi, Y. Du, W. K. Kim, and S. Min, "Investigating the effects of crystallography on subsurface damage during ultra-precision machining of sapphire," in *20th International Conference on Precision Engineering*, (Sendai, Japan), October 2024.

[70] S. B. Kwon, A. Nagaraj, D. N. Kim, D. Xi, Y. Du, W. K. Kim, and S. Min, "Prediction of crack initiation in single-crystal sapphire during ultra-precision machining using md simulation-based slip/fracture activation model," *Precision Engineering*, vol. 86, pp. 265–275, 2024.

[71] A. P. Thompson, H. M. Aktulga, R. Berger, D. S. Bolintineanu, W. M. Brown, P. S. Crozier, P. J. in 't Veld, A. Kohlmeyer, S. G. Moore, T. D. Nguyen, R. Shan, M. J. Stevens, J. Tranchida, C. Trott, and S. J. Plimpton, "LAMMPS - a flexible simulation tool for particle-based materials modeling at the atomic, meso, and continuum scales," *Comp. Phys. Comm.*, vol. 271, p. 108171, 2022.

[72] P. Vashishta, R. K. Kalia, A. Nakano, and J. P. Rino, "Interaction potentials for alumina and molecular dynamics simulations of amorphous and liquid alumina," *Journal of Applied Physics*, vol. 103, no. 8, p. 083504, 2008.

[73] W. K. Kim and B. H. Kim, "A molecular dynamics study on atomistic mechanisms of nano-scale cutting process of sapphire," *Journal of Mechanical Science and Technology*, vol. 31, pp. 4353–4362, Sep 2017.

[74] E. Brinksmeier, J. Cammett, W. König, P. Leskovar, J. Peters, and H. Tönshoff, "Residual stresses—measurement and causes in machining processes," *CIRP annals*, vol. 31, no. 2, pp. 491–510, 1982.

[75] D. Johnson-Walls, A. Evans, D. Marshall, and M. James, "Residual stresses in machined ceramic surfaces," *Journal of the American Ceramic Society*, vol. 69, no. 1, pp. 44–47, 1986.

[76] G. Bernal, B. G. Koepke, *et al.*, "Residual stresses in machined magnesium oxide crystals.," tech. rep., Honeywell Inc. corporate research center, 1973.

[77] P. J. Withers and H. Bhadeshia, "Residual stress. Part 1–measurement techniques," *Materials Science and Technology*, vol. 17, no. 4, pp. 355–365, 2001.

[78] G. Jiang, F. Haiyang, P. Bo, and K. Renke, "Recent progress of residual stress measurement methods: A review," *Chinese Journal of Aeronautics*, vol. 34, no. 2, pp. 54–78, 2021.

[79] C. Zhang, P. Feng, and J. Zhang, "Ultrasonic vibration-assisted scratch-induced characteristics of c-plane sapphire with a spherical indenter," *International Journal of Machine Tools and Manufacture*, vol. 64, pp. 38–48, 2013.

[80] V. H. Bulsara and S. Chandrasekar, "Direct observation of contact damage around scratches in brittle solids," in *Window and Dome Technologies and Materials V, AeroSense '97, 1997, Orlando, FL, United States*, vol. 3060, pp. 76–88, International Society for Optics and Photonics, 1997.

[81] Z.-C. Lin, W.-L. Lai, H. Lin, and C. Liu, "The study of ultra-precision machining and residual stress for nip alloy with different cutting speeds and depth of cut," *Journal of materials processing technology*, vol. 97, no. 1-3, pp. 200–210, 2000.

[82] S. M. Langan, D. Ravindra, and A. B. Mann, "Mitigation of damage during surface finishing of sapphire using laser-assisted machining," *Precision Engineering*, vol. 56, pp. 1–7, 2019.

[83] T. Wermelinger, C. Borgia, C. Solenthaler, and R. Spolenak, "3-D raman spectroscopy measurements of the symmetry of residual stress fields in plastically deformed sapphire crystals," *Acta Materialia*, vol. 55, no. 14, pp. 4657–4665, 2007.

[84] S. Liang and J.-C. Su, "Residual stress modeling in orthogonal machining," *CIRP annals*, vol. 56, no. 1, pp. 65–68, 2007.

[85] D. Ulutan, B. E. Alaca, and I. Lazoglu, "Analytical modelling of residual stresses in machining," *Journal of Materials Processing Technology*, vol. 183, no. 1, pp. 77–87, 2007.

[86] M. Gallas, Y. Chu, and G. Piermarini, "Calibration of the raman effect in α-Al_2O_3 ceramic for residual stress measurements," *Journal of materials research*, vol. 10, no. 11, pp. 2817–2822, 1995.

[87] W. Zhu and G. Pezzotti, "Raman analysis of three-dimensionally graded stress tensor components in sapphire," *Journal of Applied Physics*, vol. 109, no. 7, p. 073502, 2011.

[88] S. B. Kwon, *Anisotropic Removal Behavior of Single-Crystal Sapphire in Ultra-Precision Machining*. PhD thesis, The University of Wisconsin-Madison, 2022.

[89] Z.-Y. Yang, X.-M. Zhang, G.-C. Nie, D. Zhang, and H. Ding, "A comprehensive experiment-based approach to generate stress field and slip lines in cutting process," *Journal of Manufacturing Science and Engineering*, vol. 143, no. 7, p. 071014, 2021.

[90] T. Özel and E. Zeren, "Finite element modeling the influence of edge roundness on the stress and temperature fields induced by high-speed machining," *The International Journal of Advanced Manufacturing Technology*, vol. 35, pp. 255–267, 2007.

[91] G. Pezzotti and W. Zhu, "Resolving stress tensor components in space from polarized raman spectra: polycrystalline alumina," *Physical Chemistry Chemical Physics*, vol. 17, no. 4, pp. 2608–2627, 2015.

[92] G. Pezzotti and A. A. Porporati, "Raman spectroscopic analysis of phase-transformation and stress patterns in zirconia hip joints," *Journal of biomedical optics*, vol. 9, no. 2, pp. 372–384, 2004.

[93] W. Mao, Q. Chen, C. Dai, L. Yang, Y. Zhou, and C. Lu, "Effects of piezo-spectroscopic coefficients of 8 wt.% y2o3 stabilized zro2 on residual stress measurement of thermal barrier coatings by raman spectroscopy," *Surface and Coatings Technology*, vol. 204, no. 21-22, pp. 3573–3577, 2010.

[94] L.-N. Zhu, B.-S. Xu, H.-D. Wang, and C.-B. Wang, "Measurement of residual stresses using nanoindentation method," *Critical Reviews in Solid State and Materials Sciences*, vol. 40, no. 2, pp. 77–89, 2015.

[95] S. Suresh and A. Giannakopoulos, "A new method for estimating residual stresses by instrumented sharp indentation," *Acta materialia*, vol. 46, no. 16, pp. 5755–5767, 1998.

[96] Y.-H. Lee and D. Kwon, "Measurement of residual-stress effect by nanoindentation on elastically strained (100) w," *Scripta Materialia*, vol. 49, no. 5, pp. 459–465, 2003.

[97] Y.-H. Lee and D. Kwon, "Estimation of biaxial surface stress by instrumented indentation with sharp indenters," *Acta Materialia*, vol. 52, no. 6, pp. 1555–1563, 2004.

[98] Y. Zhang, M. Allahkarami, and J. Hanan, "Measuring residual stress in ceramic zirconia–porcelain dental crowns by nanoindentation," *Journal of the Mechanical Behavior of Biomedical Materials*, vol. 6, pp. 120–127, 2012.

[99] K. Kese and D. J. Rowcliffe, "Nanoindentation method for measuring residual stress in brittle materials," *Journal of the American Ceramic Society*, vol. 86, no. 5, pp. 811–816, 2003.

[100] F. Dahmani, J. Lambropoulos, A. Schmid, S. Burns, and C. Pratt, "Nanoindentation technique for measuring residual stress field around a laser-induced crack in fused silica," *Journal of materials science*, vol. 33, pp. 4677–4685, 1998.

[101] W. C. Oliver and G. M. Pharr, "An improved technique for determining hardness and elastic modulus using load and displacement sensing indentation experiments," *Journal of materials research*, vol. 7, no. 6, pp. 1564–1583, 1992.

[102] G. Pharr, W. C. Oliver, and F. Brotzen, "On the generality of the relationship among contact stiffness, contact area, and elastic modulus during indentation," *Journal of materials research*, vol. 7, no. 3, pp. 613–617, 1992.

[103] E. Broitman, "Indentation hardness measurements at macro-, micro-, and nanoscale: a critical overview," *Tribology Letters*, vol. 65, no. 1, p. 23, 2017.

[104] M. Fujikane, D. Setoyama, S. Nagao, R. Nowak, and S. Yamanaka, "Nanoindentation examination of yttria-stabilized zirconia (ysz) crystal," *Journal of Alloys and Compounds*, vol. 431, no. 1-2, pp. 250–255, 2007.

[105] A.-R. Alao and L. Yin, "Assessment of elasticity, plasticity and resistance to machining-induced damage of porous pre-sintered zirconia using nanoindentation techniques," *Journal of Materials Science & Technology*, vol. 32, no. 5, pp. 402–410, 2016.

[106] J. Wang, B. Guo, Q. Zhao, C. Zhang, Q. Zhang, and W. Zhai, "Evolution of material removal modes of sapphire under varied scratching depths," *Ceramics International*, vol. 43, no. 13, pp. 10353–10360, 2017.

[107] J. Clayton and J. Knap, "Phase-field analysis of fracture-induced twinning in single crystals," *Acta Materialia*, vol. 61, no. 14, pp. 5341–5353, 2013.

[108] A. Heuer, "Deformation twinning in corundum," *The Philosophical Magazine: A Journal of Theoretical Experimental and Applied Physics*, vol. 13, no. 122, pp. 379–393, 1966.

[109] J.-f. Yin, Q. Bai, and B. Zhang, "Methods for detection of subsurface damage: a review," *Chinese Journal of Mechanical Engineering*, vol. 31, no. 1, pp. 1–14, 2018.

[110] Y. Mizumoto, H. Kangawa, H. Itobe, T. Tanabe, and Y. Kakinuma, "Influence of crystal anisotropy on subsurface damage in ultra-precision cylindrical turning of CaF_2," *Precision Engineering*, vol. 49, pp. 104–114, 2017.

[111] L. Zhou, Y. Tian, H. Huang, H. Sato, and J. Shimizu, "A study on the diamond grinding of ultra-thin silicon wafers," *Proceedings of the Institution of Mechanical Engineers, Part B: Journal of Engineering Manufacture*, vol. 226, no. 1, pp. 66–75, 2012.

[112] P. N. Blake and R. O. Scattergood, "Ductile-regime machining of germanium and silicon," *Journal of the American ceramic society*, vol. 73, no. 4, pp. 949–957, 1990.

[113] J. Yan, T. Asami, H. Harada, and T. Kuriyagawa, "Crystallographic effect on subsurface damage formation in silicon microcutting," *CIRP annals*, vol. 61, no. 1, pp. 131–134, 2012.

[114] J. Lin, F. Jiang, Q. Wen, Y. Wu, J. Lu, Z. Tian, and N. Wang, "Deformation anisotropy of nano-scratching on c-plane of sapphire: A molecular dynamics study and experiment," *Applied Surface Science*, vol. 546, p. 149091, 2021.

[115] J. Yan, T. Asami, and T. Kuriyagawa, "Nondestructive measurement of machining-induced amorphous layers in single-crystal silicon by laser micro-raman spectroscopy," *Precision Engineering*, vol. 32, no. 3, pp. 186–195, 2008.

[116] J. Yan, T. Asami, H. Harada, and T. Kuriyagawa, "Fundamental investigation of subsurface damage in single crystalline silicon caused by diamond machining," *Precision engineering*, vol. 33, no. 4, pp. 378–386, 2009.

[117] T. Onuki, K. Kaneko, H. Ojima, J. Shimizu, and L. Zhou, "Abrasive wear damages observation in engineering ceramics using micro-raman tomography," *Journal of Advanced Mechanical Design, Systems, and Manufacturing*, vol. 17, no. 1, p. JAMDSM0009, 2023.

[118] S. B. Kwon and S. Min, "Studying mechanism of anisotropic crack generation on c-, r-, a-, and m-planes of sapphire during ultra-precision orthogonal cutting using a visualized slip/fracture activation model," *Nanotechnology and Precision Engineering*, vol. 7, no. 4, 2024.

[119] M. L. Falk and J. S. Langer, "Dynamics of viscoplastic deformation in amorphous solids," *Physical Review E*, vol. 57, pp. 7192–7205, Jun 1998.

[120] A. Stukowski, "Visualization and analysis of atomistic simulation data with OVITO-the Open Visualization Tool," *Modelling and simulation in materials science and engineering*, vol. 18, January 2010.

[121] S. B. Kwon, A. Nagaraj, D. Xi, Y. Du, D. N. Kim, W. K. Kim, and S. Min, "Studying crack generation mechanism in single-crystal sapphire during ultra-precision machining by md simulation-based slip/fracture activation model," *International Journal of Precision Engineering and Manufacturing*, pp. 1–13, 2023.

[122] Y. Wang, Z. Liang, W. Zhao, X. Wang, and H. Wang, "Anisotropic cutting mechanisms on the surface quality in ultra-precision machining of r-plane sapphire," *Applied Surface Science*, vol. 622, p. 156868, 2023.

[123] A. Nagaraj and S. Min, "Understanding of residual stress and subsurface damage by 2-step machining of single crystal sapphire," in *19th International Conference on Precision Engineering*, (Nara, Japan), November 2022.

[124] S. Wei, H. Zhao, J. Jing, F. Yun, and X. Li, "Investigation on surface residual stress distribution and evaluation of engineering ceramics in rotary ultrasonic grinding machining," *Proceedings of the Institution of Mechanical Engineers, Part C: Journal of Mechanical Engineering Science*, vol. 231, no. 15, pp. 2773–2782, 2017.

[125] MTI Corp. (2024, Nov. 12), "Al_2O_3 Single Crystal, Sapphire boule and polished wafer." Retrieved from https://www.mtixtl.com/xtlflyers/Al2O3.pdf.

[126] E. Haney and G. Subhash, "Damage mechanisms perspective on superior ballistic performance of spinel over sapphire," *Experimental Mechanics*, vol. 53, pp. 31–46, 2013.

[127] Ronar-Smith (2024, Nov. 12), "Infrared Optical Material – Sapphire." Retrieved from https://wavelength-tech.com/IR-Optics/Material-Sapphire.jsp.

[128] MTI Corp. (2024, Nov. 11), "YSZ polished wafer." Retrieved from https://www.mtixtl.com/YSZ-a-100505S2.aspx.

[129] MSE Supplies (2024, Nov. 15), "8YSZ Single Crystal Substrates." Retrieved from https://www.msesupplies.com/products/mse-pro-yttria-stabilized-zirconia-ysz-single-crystal-substrates.

[130] L. Jin, Q. Yu, A. Rauf, and C. Zhou, "Elastic, electronic and thermal properties of ysz from first principles," *Solid state sciences*, vol. 14, no. 1, pp. 106–110, 2012.

[131] F. Yang, *Electrical and thermal properties of yttria-stabilised zirconia (YSZ)-based ceramic materials*. PhD thesis, The University of Manchester (United Kingdom), 2011.

[132] P. Chen, X. Li, F. Tian, Z. Liu, D. Hu, T. Xie, Q. Liu, and J. Li, "Fabrication, microstructure, and properties of 8 mol% yttria-stabilized zirconia (8ysz) transparent ceramics," *Journal of Advanced Ceramics*, vol. 11, no. 7, pp. 1153–1162, 2022.

[133] S. Heiroth, R. Ghisleni, T. Lippert, J. Michler, and A. Wokaun, "Optical and mechanical properties of amorphous and crystalline yttria-stabilized zirconia thin films prepared by pulsed laser deposition," *Acta Materialia*, vol. 59, no. 6, pp. 2330–2340, 2011.